

# The Burst and Transient Source Experiment Earth Occultation Technique

**Short title: BATSE Earth Occultation**

B. A. Harmon<sup>1</sup>, G. J. Fishman, & C. A. Wilson

NASA Marshall Space Flight Center, SD50, Huntsville, AL 35812 USA

W. S. Paciasas<sup>2</sup> & S. N. Zhang

Department of Physics, University of Alabama in Huntsville, Huntsville, AL USA 35899

M. H. Finger<sup>3</sup>, T. M. Koshut, M. L. McCollough, C. R. Robinson<sup>4</sup> & B. C. Rubin<sup>5</sup>

Universities Space Research Association, SD50, NASA Marshall Space Flight Center, Huntsville, AL 35812 USA

## ABSTRACT

An Earth orbiting detector sensitive to gamma ray photons will see step-like occultation features in its counting rate when a gamma ray point source crosses the Earth's limb. This is due to the change in atmospheric attenuation of the gamma rays along the line of sight. In an uncollimated detector, these occultation features can be used to locate and monitor astrophysical sources provided their signals can be individually separated from the detector background. We show that the *Earth occultation technique* applied to the Burst and Transient Source Experiment (BATSE) on the *Compton Gamma Ray Observatory* (CGRO) is a viable and flexible all-sky monitor in the low energy gamma ray and hard X-ray energy range (20 keV - 1 MeV). The method is an alternative to more sophisticated photon imaging devices for astronomy, and can serve well as a cost-effective science capability for monitoring the high energy sky.

Here we describe the Earth occultation technique for locating new sources and for measuring source intensity and spectra without the use of complex background models. Examples of transform imaging, step searches, spectra, and light curves are presented. Systematic uncertainties due to source confusion, detector response, and contamination from rapid background fluctuations are discussed and analyzed for their effect on

---

<sup>1</sup>alan.harmon@msfc.nasa.gov

<sup>2</sup>bill.paciasas@msfc.nasa.gov

<sup>3</sup>mark.finger@msfc.nasa.gov

<sup>4</sup>current address:National Science Foundation, Arlington, VA 22230; crobinso@nsf.gov

<sup>5</sup>current address:American Physical Society, Ridge, NY, 11961; rubin@aps.org

intensity measurements. A sky location-dependent average systematic error is derived as a function of galactic coordinates. The sensitivity of the technique is derived as a function of incident photon energy and also as a function of angle between the source and the normal to the detector entrance window. Occultations of the Crab Nebula by the Moon are used to calibrate Earth occultation flux measurements independent of possible atmospheric scattering effects.

*Subject headings:* gamma rays: observations — instrumentation: detectors — methods: data analysis — occultations — surveys — X-rays: stars

## 1. INTRODUCTION

The *Compton Gamma Ray Observatory* (CGRO), one of NASA’s four Great Observatories, was launched in 1991 April and operated in low Earth orbit until controlled re-entry in 2000 June. CGRO was responsible for many discoveries in the study of gamma ray bursts, accreting binaries, active galaxies, and pulsars (Gehrels & Shrader 1997; Kniffen & Gehrels 1997; Leonard & Wanjek 2000). The quest for the origin of gamma ray bursts led to the development and flight of The Burst and Transient Source Experiment (BATSE) on the CGRO. BATSE pointed the way to the extragalactic origin of gamma ray bursts through mapping of burst location and number-brightness distributions (Meegan et al. 1992). In addition to BATSE’s primary science goals, its nine years of nearly continuous operation and all-sky capability allowed monitoring of the low energy gamma ray/hard X-ray sky using the Earth occultation technique (EOT). Prior to BATSE, the method had not been used widely by the astrophysics community for gathering spectral and intensity information about celestial sources. We show that the Earth occultation technique, applied to a well-calibrated multiple detector system and without sophisticated imaging hardware, is a viable and inexpensive method for monitoring the high energy sky. It is particularly suitable for uncollimated devices such as background or anti-Compton suppression shields, which are commonly used in X-ray and gamma-ray astronomy missions. We therefore present here a detailed discussion of how the Earth occultation technique was applied to BATSE data. A listing of acronyms and abbreviations used throughout the text can be found in Appendix A.

Historically, monitoring of the high energy sky was accomplished in the energy range of  $\sim 1$ -20 keV using various types of scanning pinhole cameras, modulation collimators, or position-sensitive detectors. X-ray missions such as *Uhuru* (Giacconi et al. 1972), *Vela 5B* (Conner, Evans & Belian 1969), the *Ginga* All-Sky Monitor (Tsunemi et al. 1989), *Ariel 5* (Holt 1976) the GRANAT and EURECA Watch monitors (Lund, 1986; Brandt, 1994; Castro-Tirado, 1994) and most recently, the All-Sky Monitor on the *Rossi X-Ray Timing Explorer* (RXTE) (Bradt, Rothschild & Swank 1993; Levine et al. 1996) have been crucial in discovering and monitoring of X-ray transients, investigating long-term periodic variations in more persistent sources, and detecting other phenomena associated with the X-ray sky. BATSE complements these instruments by monitoring the energy range from 20 keV up to about 1 MeV. This covers the lower energy portion of the nonthermal regime, where the emission is produced by a variety of processes such as Compton up-scattering of soft photons by energetic particles, bremsstrahlung, and synchrotron radiation.

It was realized prior to launch (Fishman et al. 1982; 1984; 1989) that BATSE could serve as a sensitive all-sky monitor of point-like gamma ray sources. Earth occultations of point sources allow sampling of high energy fluxes using the sharp step-like features in the background data for both pulsed and nonpulsed sources (Paciesas et al. 1985). Variations on timescales of hours to years can be investigated. The method allowed BATSE to be very successful at locating new transients, detecting unusual intensity or spectral changes, and stimulating observations in other wavelength bands. Because the EOT was enhanced and used extensively during the operational period of CGRO, we present its use in various forms, and discuss a number of aspects of the

technique such as source identification, sensitivity, and systematic error. Pre-launch discussions of the method can be found in Paciasas et al. (1985) and Fishman et al. (1989). Discussions concerning the post-launch performance and expanded capabilities can be found in Harmon et al. (1992), Wilson et al. (1992), Zhang et al. (1993), and Zhang et al. (1994a). Preliminary surveys of detected sources can be found in Harmon et al. (1993) and Robinson et al. (1997). An imaging capability was added after launch, based on the Radon transform, which greatly improved our ability to locate and identify gamma ray sources (Zhang et al. 1993, 1994a). Another powerful application of BATSE as an all-sky monitor was the ability to detect and monitor pulsars using Fourier analysis or epoch folding techniques. A detailed description of these methods and results from BATSE data can be found in Bildsten et al. (1997).

## 2. INSTRUMENTATION AND OCCULTATION GEOMETRY

### 2.1. BATSE Instrumentation

The Earth occultation analysis technique utilizes the large area detectors (LADs) on BATSE, which are sensitive to photons above 20 keV. The *Compton Gamma Ray Observatory* and placement of the BATSE detector modules on the spacecraft are shown in Fig. 1. The LADs are composed of sodium iodide (NaI(Tl)) crystals, 1.27 cm (0.5 in) thick by 50.8 cm (20 in) across (2025 cm<sup>2</sup> total area of one detector). Eight modules are mounted on the corners of the CGRO with normal vectors perpendicular to the faces of a regular octahedron. Any point on the sky can viewed by four detectors at angles less than 90° to the source direction. This gives BATSE a capability of obtaining crude locations to within a few degrees using the count rates from a combination of detectors and the known response of each detector from photons directly from the source, and source photons scattered off the atmosphere (Pendleton et al. 1995a). This is routinely done to locate gamma ray bursts to within an accuracy of a few degrees (Pendleton et al. 1999). A full description of the BATSE detectors can be found in a number of places; see, for example, Fishman et al. (1984, 1989).

Although Earth occultation features have been used with other gamma ray instruments to restrict the location of point sources (e.g., Wheaton et al. 1982), to our knowledge, only BATSE made use of the method for direct measurement of point source emission. Some Earth occultation measurements have been performed with the BATSE spectroscopy detectors (SDs) (McNamara, Harmon & Harrison 1995; 1996; Paciasas et al. 1998; McNamara et al. 1998). These detectors have a much smaller effective area for source monitoring ( $\sim 600$  cm<sup>2</sup>) than the LADs, but do have an additional low energy bandpass around 10 keV. Here we discuss the method as applied only to the large area detectors.

The Earth occultation technique was also developed and applied to BATSE data in a separate, parallel effort at the Jet Propulsion Laboratory (JPL) (Skelton et al. 1994; Ling et al. 1996). The JPL group has recently published a description of their approach (the Enhanced BATSE

Occultation Package (EBOP)), and a compendium of measurements using the technique covering the 1991 May to 1994 October epoch (Ling et al. 2000). The method used by JPL was developed specifically for extraction of flux histories and spectra of point gamma ray sources. There are primarily two major differences between the JPL method and the method we describe in this paper. First, EBOP uses a semi-physical model for the detector background counting rates. The model is based on expected contributions of low energy gamma ray fluxes local to the low Earth orbit (LEO) environment. These include cosmic ray secondary radiation and activation products from orbital passes through radiation fields in LEO. The JPL global background model consists of a mix of the local radiation components and a combination (determined by the fit) of the SD counting rates as a predictor of the low energy background in the LADs. Secondly, the extraction of source signals is performed usually in one-day segments, with a single fit including terms for *all* sources in the EBOP catalog with *no a priori* assumptions of their intensity. The JPL method has the advantage of potentially greater statistical accuracy at the expense of increased systematic error. The method appears to give reasonable results for bright, hard sources such as the Crab Nebula and Cygnus X-1. In some cases, for relatively weak sources, such as the neutron star binaries Circinus X-1 and Scutum X-1, the JPL method yields significant hard emission greater than  $\sim 200$  keV, which is uncharacteristic for this class of sources (see discussion in Sec. 3.2 and Fig. 8, plates 10 and 75 of Ling et al. 2000). We have not been able to confirm these unusually hard spectra with the Marshall Space Flight Center (MSFC) method, nor are they reported by other high energy observatories.

Instead of the physical inputs used in the JPL fitting procedure, the MSFC method uses simple polynomials as the set of basis functions for fitting the background and extracting the source signal (see Section 3 for details). This is equivalent to assuming that the background is smooth on a timescale of a few minutes, as discussed in Section 3, with respect to count rate variations caused by cosmic ray secondaries, activation, and other local background components. This assumption breaks down only during times of high solar flare activity, gamma ray bursts and a few flaring gamma ray sources, which are either excluded from the analysis, or flagged later at the discretion of the observer (see Sec. 2.2 for a discussion of data selection procedures). The only source terms included in the fit are those which are thought to be active during the short four-minute time windows. We chose to adopt the method described here over that of EBOP to minimize the effect of unpredictable systematic error, and because of the real-time needs of the MSFC all-sky monitoring effort. The MSFC method also lends itself well to an iterative approach in selecting sources that may potentially interfere with the source of interest (SOI), so that a best solution comes from building up a knowledge of the sky region within a few degrees surrounding the source.

More recently, Southampton University has undertaken a more rigorous approach in modeling the BATSE backgrounds in order to generate all-sky images and extract of source fluxes using Earth occultation (Shaw et al. 2000). This method incorporates the physical background components discussed above and a mass model of the *Compton Observatory* in a Monte Carlo

simulation using the radiation transport code GEANT as was done with the European Space Agency International Gamma Ray Astrophysics Laboratory (INTEGRAL) (Lei et al. 1999). The result of the simulation is the *a priori* determination of the total diffuse background in the LADs at any orientation and geomagnetic coordinates of the Earth. This method offers the possibility of removing the source signal without the need for a simultaneous fit to the background.

## 2.2. Data Selection

The LADs are well-suited to Earth occultation measurements because of their sensitivity, uniformity in energy range, and stabilized gain. Data from two or more LADs can be easily combined or fitted jointly, depending on the application. There are two different data types which are most convenient for occultation measurements: DISCLA (LAD discriminator data) and CONT (or LAD continuous data) which cover the same energy range (20 keV - 1 MeV). The DISCLA data type provides four energy channels binned every 1.024 seconds, and the CONT datatype provides 16 channels every 2.048 seconds.

Prior to application of the Earth occultation method, proper data selection is required to remove large fluctuations that may affect the fitting of occultation steps. When data are flagged in one stage of the selection process, they are then excluded from the occultation analysis.

The first stage of the data selection is performed onboard. Several different datatypes are scanned, including the DISCLA type, by comparing the local background count rate to new data as they are acquired. An event may “trigger” the gamma ray burst (GRB) acquisition mode when a high data rate is encountered relative to the background in two or more LADs (Meegan et al. 1992). High rate events may be caused by bursts, solar flares, bremsstrahlung from electron precipitation (Aschwanden, Schwartz & Dennis 1998), terrestrial gamma ray flashes (Fishman et al. 1994a), or even flaring galactic sources (Mallozzi et al. 1993). Any triggered events are flagged automatically in the datastream and identified later.

The second stage of the selection process consists of manual inspection for other events that may escape the burst trigger, yet generate large transient flares. These are of a somewhat longer timescale than GRBs, usually a few tens of seconds to minutes. The fluxes from these events are generally easy to identify based on their observed timing and spectral properties. Time periods containing transient background features large enough to be detected visually (about 10% of the total background counting rate) are flagged and excluded from occultation analysis along with the triggered events. The vast majority of these events are gamma ray fluxes solar flares or bremsstrahlung from precipitating electrons.

The last stage of the data selection consists of additional flagging of very short ( $< 1$  sec) cosmic ray events. These occur in only one LAD at a time when a heavy cosmic ray, such as an iron nucleus, deposits a large amount of energy into the scintillation medium. This is observed as a sharp, positive-going spike in the background data for one time bin. It is caused by long-lived

phosphorescence characteristic of impurities in the NaI(Tl) crystal (Fishman & Austin 1976). The affected data bins are flagged using a spike filter prior to occultation as well as pulsar measurements.

An interesting aside to the standard data treatment discussed above is that bright and extremely variable galactic sources are occasionally detected via the burst trigger. Such occurrences do not affect earth occultation analyses to a large degree because the amount of data excluded in the data selection process due to intrinsic source variability is statistically insignificant. However, the extremes of variability are reduced if the burst trigger is enabled by the SOI, since the CONT or DISCLA data at the time of the trigger are rejected in our data analysis procedure. The sources for which this was known to have occurred during the mission are A 0535+262 (Finger, Wilson & Harmon 1996) (see Fig. 2), Cygnus X-1 (Fishman et al. 1994b), GRO J0422+32 (Mallozzi et al. 1993), GRO J1744-28 (Kouveliotou et al. 1996), and 4U 1700-377 (Rubin et al. 1996a), and soft gamma ray repeaters (Woods et al. 1999). For some flaring episodes of these sources, the BATSE burst trigger threshold was raised temporarily in order to minimize the number of non-GRB triggers. Normally, the likelihood of a source being rejected in this manner for Earth occultation measurement is rather small due to the great difference in peak brightness of these sources and that of GRBs. It should be noted that when data are flagged and removed from the analysis, in actuality, the data are recoverable by re-analyzing the CONT or DISCLA data with less restrictive filtering criteria.

### 2.3. Source Occultations

In one orbit around the Earth, two occultation step features, a rise and set pair, will be superimposed on the background counting rate as each point source is occulted. A measurement can be made of the intensity of a source in each energy channel at rise or set. In practice, two measurements per *every* orbit are not achieved. The most common reasons are passages through the lower Van Allen radiation belt at the South Atlantic Anomaly when the detector voltage is turned off, or that CGRO is out of line-of-sight contact with the NASA Tracking & Data Relay Satellites (TDRSS), and data which have been flagged and are not available for analysis. High declination sources ( $\sim |\delta| \geq 41^\circ$ ) also experience an interruption of occultations near the orbital poles (see Appendix B). Source confusion, where occultations of one source are indistinguishable from another, also limits the number of usable occultation steps. The impact of these effects combined causes Earth occultation coverage averaged over one precession cycle ( $\sim 52$ d) to range between 80%-90%, at best, and at worst, about 50%.

The attenuation of gamma rays by the Earth's atmosphere and the variation in thickness of the air mass along the line of sight to the X-ray source produce the step-like features in the detector count rate as a function of time. The attenuation is 50% for 100 keV photons that pass through the atmosphere along a line of sight with minimum altitude of 70 km. For a typical orbital speed of 8 km/s, the duration of the occultation step for a source rising or setting in the plane

of the spacecraft orbit is about 10 seconds. Therefore occultations are relatively sharp features superimposed on the generally slower background variations caused by orbital motion around the Earth.

Several examples of occultation features, or “steps”, in the DISCLA and CONT data are shown in Fig. 2. Except where otherwise noted, the date and time convention used in this paper is *Truncated Julian Date* (TJD) = Julian Date (JD) - 2,440,000.5 and *seconds of day* measured from the TJD start. Fig. 3 shows a close-up view of individual occultation steps with fitting functions based on a model for the atmospheric attenuation for gamma rays (See Section 3.1).

The accuracy to which the timing and magnitude of these steps can be fit determines the performance of the Earth occultation technique. We discuss three forms of the technique from which information can be obtained using BATSE data: (1) the flux and spectra extraction method, where we assume *a priori* knowledge of source locations, and (2) the step search and (3) the occultation imaging methods, where the source location is not required. Methods (2) and (3) are best-suited for new source searches. An overall comparison of these approaches is given in Table 1.

In Appendices B and C, we supplement the discussion of the EOT by developing the mathematical framework for Earth occultation from an orbiting spacecraft. This includes expressions for timing of Earth occultation features and their use for locating point sources.

### 3. FLUX AND SPECTRA EXTRACTION FOR KNOWN SOURCES

#### 3.1. Estimation of Occultation Steps in Counting Rates

The count rate for a source in the LAD is extracted by simultaneously fitting occultation step features with terms for each source in the fit and a quadratic polynomial to represent the detector background. The fit is performed independently for each energy channel. Each occultation step, rise or set, is fit over a time  $t_{occ} - \tau$  to  $t_{occ} + \tau$ , which we refer to as the *fitting window*.  $t_{occ}$  represents the occultation time of the SOI and also the center of the time window. Use of a quadratic form for the background restricts the half-width of the fitting window,  $\tau$ , to no more than about 120 seconds of data. The modeled detector count rate  $R$  in each energy channel can be represented as

$$R(t) = \sum_{i=0}^2 b_i(t - t_{occ})^i + \sum_{j=1}^n r_j T_j(t) \quad (1)$$

where  $b_i$  are the coefficients of the background model (to second order) and  $r_j$  are the source count rates including the SOI and other bright sources with occultation steps occurring within the fitting window, and  $T_j(t)$  are the atmospheric transmission functions. The number of source terms  $n$  is kept to a minimum for greatest sensitivity, at the expense of incurring some systematic error. This method is similar to that adopted in Wheaton et al. (1995) for multi-parameter least squares fitting of data when the detector background is time variable and individual measurements are of



low statistical quality. We assume that the background is smooth and adequately fit by the second order polynomial on the order of the size of the fitting window,  $2\tau$ . In particular, the failure of this assumption is usually caused by the presence in the data of bright pulsars, weak bursts, solar flares, and other disturbances on the timescale of the fitting window. Problematic stretches of data are mostly removed in the data selection process discussed in Sec. 2.2. Experience shows that there are non-Poissonian components that remain in the data, and must be accounted for in the analysis of results. However, most of these effects add incoherently on timescales of a day or longer.

The occultation features are represented via a model function for the transmission  $T(t)$  as

$$T(t) = e^{\mu(E)A(h(t))} \quad (2)$$

where  $\mu(E)$  is the energy-dependent mass attenuation coefficient of gamma rays in air (Storm & Israel 1970; Chupp 1975) and  $A(h)$  is the air mass computed along the line of sight at a given altitude  $h(t)$ .  $A(h)$  is interpolated from a table of air masses (W. Wheaton, private communication) for values of  $h$  between 50 and 110 km, and is based on the U.S. International Commercial Aviation Organization (ICAO) Standard Atmosphere (1962). Use of Eqs. (1) and (2) requires precise knowledge of the spacecraft ephemeris (time and position), the direction to the SOI, and a model of the Earth that accounts for its non-sphericity (see Appendix C). To use the CONT data at its full time resolution of 2.048s, the position of the spacecraft at the center of the time bin must be known accurately. The spacecraft position is nominally interpolated for the center of the 2.048s time bin from the incoming ephemeris data. For most of CGRO mission, the component of the position vector in the direction of spacecraft motion was known to less than 10 km. Due to the sharpness of occultation profiles ( $\sim 10$ s), ephemeris errors even on the order of 25 km downrange (about 1 part in 2000) can shift the step model enough to seriously affect the flux measurement. A few ephemeris problems occurred during the mission, but were corrected in the data archive. The ability to measure the time of an occultation and the sharpness of Earth occultation features can be exploited to determine the location of a source as outlined in Appendices B and C.

A database of source locations, outburst times, and intensities provides information to determine whether terms for sources should be included in the fitting window. This database was built up as new sources were found either through occultation analysis (light curves and images) or from other instrument measurements. Information about source outburst intensity levels as a function of time are read from the database by the analysis software before the flux measurement is performed.

Each energy channel in the source-pointed LADs (defined to be less than  $60^\circ$  between the source direction and detector normal) is fit independently to derive a count rate in each CONT channel for all sources  $r_j$  as a function of time. The statistical error ( $\delta r_j$ ) of the  $r_j$ th term at time  $t_{occ}$  is computed from the least squares fit of Eq. (1). Some physical insight into the obtainable error from the Earth occultation fits can be achieved by assuming a simple linear step function in place of the transmission function  $T_j(t)$  in Eq. (1) and setting  $j=1$  (only the SOI is considered).

The uncertainty in the fit can then be extracted from the Hessian, or information, matrix (Press et al. 1992), which is to first order

$$\delta r_j = \eta \sqrt{\frac{2R_o}{\tau}} \quad (3)$$

where  $\eta$  is a parameter that depends on the half-width,  $\tau$ , the occultation step width, and the slope of the background across the fitting window.  $R_o$  is the detector count rate at the center of the fitting window. For an occultation step of width 10s and  $2\tau=240$ s,  $\eta \approx 3$ .

To derive a flux history, the fitting coefficient corresponding to the SOI (the  $r_j$ th term at time  $t_{occ}$  in Eq. (1)) is accumulated as a function of time for later deconvolution from the instrument response. However, all the coefficients, including those for other sources in the fit, and the background terms, can be written to a file for later use.

### 3.2. Spectral Analysis

Here we present examples illustrating the usefulness of the BATSE EOT to measure source variability and differences in spectral behavior. The technique has been used to monitor spectral state transitions in the black hole candidates GX 339-4 (Harmon et al. 1994; Rubin et al. 1998) and Cyg X-1 (Zhang et al. 1997). During the operational lifetime of CGRO, outbursts of monitored sources, particularly unusual ones, were made known to the scientific community through various electronic media.

The history of the source intensity and spectral behavior can be generated from the  $r_j$  in Eq. (1). The  $r_j$  in counts  $s^{-1}$  per energy channel per LAD, without correction for the detector response, are stored in a time-ordered file with a beginning and ending time specified by the user. Energy spectra (flux per energy channel) and light curves showing the history of the source's intensity as a function of time can be generated from the raw history file.

The octahedral geometry of BATSE insures that at least four detectors simultaneously view a point source anywhere on the sky. The angular sensitivity of the LADs is maintained by combining statistics from two, three and ultimately four detectors at successively larger angles from any one of the detector normals as discussed later in Sec. 3.3. Since there is no improvement in the signal-to-noise ratio by combining data from detectors beyond about  $60^\circ$ , this is a convenient cutoff angle for choosing which detectors are used. Furthermore, the natural timescale for which spectral measurements are most easily obtained without changing detector combinations is the observation, or pointing period, of CGRO. Observations, where the orientation of the LADs were kept fixed with respect to celestial coordinates, lasts about two to three weeks. The specific orientation of the X and Z axes, which were set by the CGRO observing schedule, determined the LAD combination for viewing a point on the sky.

In Fig. 4, LAD count spectra and model residuals are shown for four sources extracted using the method of the previous section. Each frame consists of source count rates as measured via

Earth occultation for a set of LADs whose normal vectors are less than  $60^\circ$  to the respective direction of the source. All occultations of same source have been fitted to determine the  $r_j$ , which are then averaged over the observation period to yield the rates (error-weighted) and uncertainty for each channel in each detector as shown in Fig. 4. The number of detectors per combination ranges from two (Vela X-1) to four (Cygnus X-1).

The dotted curves represent the best fitting model spectra for each LAD. The fitting procedure, used commonly in high energy astronomy, is called “forward-folding” (Briggs 1995). This method avoids a potentially unstable inversion of the BATSE response matrices, which have large off-diagonal elements due to the LAD’s relatively shallow detection depth. (We will delay discussion of the LAD response formalism until Sec. 3.5.) Minimization of the chi-square statistic is performed using the Levenberg-Marquardt formulation of linear least squares (Press et al. 1992). The selected spectral model is folded through the instrument response (Pendleton et al. 1995a) for all detectors in the combination to determine model count spectra. The choice of an appropriate spectral model is based on trial and error, and depends on the type of source. The parameters of the model are then adjusted to minimize chi-square between the model count rates and the observed count rates for all detectors in the combination. If all fourteen energy channels are used, the number of degrees of freedom is  $(\# \text{ of LADS}) \times 14 - p$ , where  $p$  is the number of parameters in the model. Residuals from the model fit in number of sigmas are shown below the count rate spectra for all detectors in the fit.

In Fig. 5 we show the corresponding multiple detector photon spectra after deconvolution of the response for the same four sources and observation periods as in Fig. 4. The solid curves represent the best fitting spectral model with parameters given in Fig. 5. Uncertainties in the fit parameters are obtained according to the prescription of Lampton, Margon & Bowyer (1976). Data points in photon space and associated uncertainties (here in photons  $\text{cm}^{-2}\text{s}^{-1}\text{keV}^{-1}$ ) are derived by multiplying the spectral model by the ratio of the model counts to the observed counts. The channel boundaries and photon data points are averaged for the LADs after deconvolution of the response function.

Representative light curves as a function of time are shown in Fig. 6. For generation of light curves, the same type of spectral fit is performed on the count spectra, usually with one or more days of occultation data, then fluxes for each point in the light curves are obtained by integrating over a specified energy range of the best fitting spectral model. In cases where the flux is not a parameter, the uncertainty in the flux is obtained either by analytically or numerically differentiating the fitting model with respect to the parameters. For generating light curves, the simpler spectral models, with one or two parameters, such as single power law or bremsstrahlung are best for the shorter energy range, whereas for longer integrations as shown in Fig. 5, more sophisticated models can be used.

It should be kept in mind that the treatment of statistical errors in the data shown in Figs. 4-6 are based on propagating the error from the source count rates extracted from occultation

step fits to the raw data. The errors shown in the count spectra in Fig. 4 come from direct error-weighted averaging of occultation step rates occurring over an observation period. In Figs. 5 and 6, even though the proper prescription of errors in the spectral fitting parameters are given, it is important to note that the “data” in photon space are model dependent. For example, when a source is near the minimum detectable limit (see Sec. 3.3), and the statistical significance is low, the absolute value of the data in photon space depends heavily on the choice of spectral model. A much more desirable method of obtaining accurate fluxes and/or upper limits in a given energy band is to compare the source count rate to that of the Crab Nebula.

Error-weighted averaging across CGRO pointing boundaries *after* deconvolution of the response is a straightforward method to increase the significance of a source signal. This is desirable for cases in searching for weaker emission or longer-term variations in sources. For the light curves in Fig. 6, it is simply a matter of binning the flux data into longer time bins. Alternatively, it is possible to combine channel by channel data *before* deconvolution of the response. The fitting can then be done by retaining the total exposure to the source in each observation interval and weighting the detector response accordingly. This approach is desirable when energy spectra for weak sources ( $\sim$ few mCrab) are required; however, systematic errors limit the ultimate flux sensitivity that can be achieved by averaging over many weeks or even years. The issue of systematic error is dealt with in later sections.

### 3.3. Sensitivity

We first consider the sensitivity of Earth occultation without complicating factors such as nearby point sources and imperfections in the detector response function. The sensitivity of the EOT with the BATSE LADs depends on several factors. The uncollimated detector geometry of the LADs and the fixed orientation of CGRO with respect to the sky (for a single pointing period) generates continuously varying backgrounds which range over a factor of two or more. The lower energy background (up to  $\sim$ 100 keV) is dominated by the modulation of the diffuse sky flux by the Earth and at higher energies by the cosmic ray secondary radiation as shown in Fig. 2. Thus the low energy background exhibits a slow sinusoidal variation with the orbital period of the spacecraft. At high energy, the background is modulated more rapidly due to the changes in magnetic field strength and direction. Furthermore, a given source exposes a combination of several detectors at different angles. The effective area of the LAD (the product of the geometric area and the efficiency) is also a strong function of energy just above the lower energy threshold due to the entrance window attenuation. It decreases more slowly at higher energies from Compton leakage. All these factors combine to produce complex energy and time-dependent variations in the background. Nevertheless, we can use the known Crab Nebula flux as a standard candle to perform an empirical calculation of the sensitivity.

A basic representation of the instrument sensitivity to a point source of continuum emission

over a specified energy range is

$$F_{min} = \frac{N_\sigma}{A\epsilon} \sqrt{\frac{R_B}{T_{live}}} \quad (4)$$

where  $F_{min}$  is the minimum detectable flux for  $N_\sigma$  standard deviations,  $R_B$  is the background count rate,  $\epsilon$  is the detector efficiency,  $A$  is the geometric area of the detector, and  $T_{live}$  is the livetime of the observation. This expression does not lend itself readily to an EOT sensitivity calculation, since the background changes within the fitting window and  $T_{live}$  is not a well-defined quantity. In addition, correction for a small rate-dependent electronic deadtime is made at that time for the CONT data in counts are converted to count rates. Therefore we replace  $\sqrt{R_B/T_{live}}$  with the uncertainty  $\delta r_s$  from the least squares fitting problem (see Eq. (3)), so that

$$F_{min} = \frac{N_\sigma}{A\epsilon} \delta r_s. \quad (5)$$

Note that Eq. (5) combined with the semi-analytical expression Eq. (3) can be used to estimate Earth occultation sensitivity for a given background rate; however, we can use the Crab Nebula with known flux and measurement errors to obtain a more accurate calculation.

The Crab Nebula flux ( $F_{Crab}$ ) can be related to the measured Crab count rate  $r_{Crab}$  using

$$r_{Crab} = A\epsilon F_{Crab} \quad (6)$$

Combining Eqs. (5) and (6) by eliminating the area and efficiency factors yields

$$F_{min} = \delta r_{Crab} \frac{N_\sigma F_{Crab}}{r_{Crab}} \quad (7)$$

We adopt a best fit broken power law for the Crab Nebula spectrum in photons  $\text{cm}^{-2} \text{s}^{-1} \text{keV}^{-1}$  obtained from HEAO-A4 measurements (Jung 1989)

$$\begin{aligned} \mathcal{S}_{Crab}(E) &= 3.25 \times 10^{-3} / (E/45)^{2.075} \quad \text{for } E < E_B \\ \text{and } \mathcal{S}_{Crab}(E) &= 3.732 \times 10^{-4} / (E/E_B)^{2.48} \quad \text{for } E \geq E_B \end{aligned} \quad (8)$$

where  $E_B = 127.7$  keV. Equation (8) has been used previously in evaluating the performance of BATSE prototype LADs in balloon observations of supernova SN 1987A (Pendleton et al. 1995b). The HEAO A-4 spectrum compares well with the observed Crab Nebula spectrum during the balloon flight. We can now compute the sensitivity as a function of energy, angle and detector combination, provided the source signal is adequately determined.

A large body of Crab Nebula occultation data was obtained in all eight detectors in the 16 CONT data channels at many orientations of the CGRO, covering a period of about five years. These data, as we discuss later in the context of systematic error, were parameterized so that the Crab Nebula source rate at any angle or energy in the LADs could be determined. The parametrization therefore automatically contains the averaged exposure and background effects typical of BATSE data, and can be used to determine  $r_{Crab}$  and  $\delta r_{Crab}$  in eq. (7).

Using eq. (7) and integrating eq. (8) over the appropriate energy range to obtain  $F_{\text{Crab}}$ , we derive the point source sensitivity of a typical two week observation (approximately the length of one CGRO pointing period). This is shown as a function of energy and angle in Figs. 7 and 8, respectively. As the angle to the source from the detector normal increases (Fig. 8), two, three and four detector combinations in the octahedral geometry become more sensitive than a single detector as shown. Table 1 compares the sensitivity of the flux extraction method and the two point source search methods discussed later.

It should be kept in mind that the sensitivity in crowded sky regions such as the galactic center region is degraded from that shown in Figs. 7 and 8 due to additional terms in Eq. (1) for known interfering sources and systematic error in the flux measurements. We discuss causes of systematic error in the next section.

### 3.4. Systematic Errors Related to Sky Location and Limb Geometry

Several sources of systematic error were identified in the use of the EOT to measure source fluxes. We have identified those based on location in the sky combined with orbital precession effects, unusual variations in the background, and also absolute flux using the instrument response. The treatment of systematic error varies depending on use of the data.

The current method of extracting flux and spectral occultation data assumes some *a priori* knowledge of source intensity for sources other than the SOI, i.e., a decision is made as to what sources must be included in eq. (1). The selection of which sources are included in the fitting window is therefore an important determiner of the systematic error in two cases: (1) where residual sharing of flux occurs between source terms in the fitting process, and (2) where sources are neglected intentionally, because of an incorrect assumption about the sources' relative intensities to the SOI, or unintentionally, simply because an unknown source was present in the fitting window at the time. It is important therefore to keep a controlled database of bright source information as discussed in Section 3.1. Generally, sources that exceed  $\sim 0.02$  photons  $\text{cm}^{-2}\text{s}^{-1}$  in the 20-100 keV band (about 75 mCrab for a source with a Crab-like spectrum) are considered as sufficiently bright to be included in the fitting window. This corresponds to about  $2\sigma$  detection in one day sampling by Earth occultation (see Table 1). We have chosen a modest flux level that is comparable to our one-day sensitivity. Setting thresholds in count space would be preferable, but this adds significantly to the computational burden. A single threshold in photon space should be regarded as a first pass method in an iterative process designed to achieve best results. No account is made for the spectral differences between the SOI and potentially interfering bright sources. It is possible, for example, in a reanalysis to set finer intensity thresholds or make energy-dependent cuts.

The Crab Nebula and the black hole system Cyg X-1 generally are the most persistently bright hard X-ray to low energy gamma ray sources in the sky. Only occasionally do other sources,

usually transients, exceed the intensity of these objects. The Crab and Cyg X-1 are therefore dominant contributors to systematic error in their respective sky regions when their occultation steps fall into the fitting window of the SOI.

An analysis of these errors can be made by examining the limb geometry as a function of time. In Fig. 9 we show the sky region near the Crab Nebula and Cygnus X-1 and surrounding sources monitored by BATSE. In each plot, two shaded regions are shown. Those bounded by dashed curves represent the set of projections of the setting limb of the Earth as the spacecraft moves through one precession cycle of its orbit. The shaded regions bounded by solid curves are the equivalent regions for the rising limb. The limb appears noncircular because of the flat sky projection.

Note that some regions of the sky are not swept by the Earth’s limb at times of occultation of the Crab and Cyg X-1. For example, the gamma ray sources GRO J0422+32 and Geminga are located in sky regions that are not crossed by the projected limb of the Earth at times of occultation of the Crab. Light curves generated for either these two sources show minimal deviation with precession phase due to the presence of Crab occultation steps near in time to those of the two sources of interest. In contrast, 4U 0614+091 or SAX J0501+11, are located such that the projected setting and rising limbs of the Crab, respectively, cross them at certain times during the precession cycle. This is equivalent to the Crab and the two sources having occultations at essentially the same time for a period of 1-2 days. Light curves for these two sources will exhibit significant systematic deviations in their light curves near and at these times.

This is illustrated in Fig. 10, where we show the time dependence of the angle between the locations of the sources (a) GRO J0422+32 and (b) 4U 0614+091, and the closest approach points of the Earth’s limb projection that intersect the Crab Nebula over a period of 200 days, or about four precession cycles. The corresponding light curves over the same time intervals are shown. GRO J0422+32 is not detected during this time, but 4U 0614+091 is detected consistently, but variable ( $\sim 0.01$  photons  $\text{cm}^{-2} \text{s}^{-1}$ ). The minimum angle for the setting limb of Crab approaching GRO J0422+32 is about  $3^\circ$ , and therefore the occultation steps are well separated. However, for the setting limb of the Crab crosses the location of 4U 0614+091, and the occultations become superposed for a few days every precession cycle (for example, around TJD 9900). The corresponding light curve for 4U 0614+091 shows systematic deviations at these times due to residual sharing of source signal as we approach the conjunction of the setting occultation steps. Our general treatment of these light curves is to reject the measurement of occultation steps of 4U 0614+091 that fall within 10 secs of the Crab steps ( $\sim 0.7^\circ$ ). The amount of signal sharing depends on factors such as the broadness of the occultation features (governed by the elevation angle,  $\beta$ , of the source above the CGRO orbital plane, see Appendix B) and the steepness of the background. Sometimes a cut is made on the step measurements when the angle between the limb and the source location is less than  $2^\circ$ , which unfortunately creates or increases gaps in coverage when both the rising and setting limbs have poor geometries for separating the flux from the SOI from interfering sources. Here we derive an average systematic error as discussed below to account

for this effect.

Our investigation of several sources of systematic error illustrates that it is difficult to quantify the total systematic error precisely. Unknown systematic errors due to source confusion are time and sky location dependent. An additional source of systematic error, discussed in the context of source step searches, is the presence of non-statistical background fluctuations (red noise and coherent pulses) from bright X-ray sources. We generally characterize these as background components that are, in practice, unpredictable.

Another source of error that we have not treated rigorously is the diffuse galactic emission along the galactic plane (Valinia & Marshall 1999). Under appropriate limb conditions, the diffuse component may have a sufficiently sharp profile in galactic latitude at energies in the sensitive range of BATSE to create occultation step-like features in the background and/or to increase the amount of cross-coupling between background and source terms in the fit. At this time, we have not tried to separate the diffuse component from possible weak point source contamination in the galactic bulge region. Although the presence and structure of the ridge is scientifically interesting, modeling of this component is best done in context of a global background model, and so beyond the scope of this paper.

We wish, nevertheless, to estimate a total *average* systematic error (source confusion + unpredictable background variations). To do this, we created a grid covering the galactic plane in areas where sky-dependent systematic error is a significant problem as shown in Fig. 11. The grid has points every  $3^\circ$  along the galactic plane with two sets of grid points at  $+6^\circ$  and  $-6^\circ$  galactic latitude. Grid points within  $2^\circ$  of known bright occultation sources were excluded, yielding a total sample of 156 points.

In Fig. 12, we show the average flux from each grid point averaged over a 7.2 year period and the standard deviation of one-day flux averages from the beginning of the CGRO mission, in 1991 April, to 1998 July, as a function of galactic longitude,  $l_{II}$ . The standard deviations are clearly broader than predicted for a Gaussian distribution about zero flux due to systematic errors from various effects ( $1 \sigma = \sim 0.01 \text{ photons cm}^{-2}\text{s}^{-1}$ ). We find broadening factors of about 30% to 60% in excess of normal statistics, strongest near the galactic center, and near bright, variable sources such as Vela X-1 ( $l_{II} = -96.9^\circ$ ) and Cygnus X-1 ( $l_{II} = 71.3^\circ$ ). There are also small positive and negative trends in the average fluxes for the 156 test points. Absolute values are less than  $\sim 0.01 \text{ photons cm}^{-2}\text{s}^{-1}$ , with the exception of the galactic center itself. Even though small, the galactic bulge region between  $+60^\circ$  and  $-60^\circ$  shows a clear effect, presumably due to weak X-ray and gamma ray sources in greater numbers, and/or a galactic ridge component. The trends for galactic latitude are similar, but narrower in spatial extent. These results are used to estimate systematic error in the BATSE Earth occultation catalog of low energy gamma ray sources (Harmon et al. in preparation).



### 3.5. Systematic Errors Due to Detector Response Model

The response matrices for the BATSE large area detectors have been described elsewhere (Pendleton et al. 1995a), as well as their use for locating gamma ray bursts (Pendleton et al. 1999). The matrices are an ordered, discrete representation of the BATSE gamma-ray detectors’ response characteristics, and thus are used for all types of studies such as bursts, distant point sources, solar flares and atmospheric gamma ray phenomena. They are designed to convert background-subtracted source counts to incident photon spectra. The main parameters used to characterize the response is the incident photon energy, the measured detector output energy, and the angle between the detector normal and the source direction. LAD prototypes were used in balloon flight observations of SN 1987A and the Crab (Pendleton et al. 1995b), for which an early version of the matrices eventually used for BATSE was developed. A Monte Carlo simulation was used to generate the BATSE LAD responses based on a well-known electromagnetic cascade/transport code called EGS (Ford et al. 1978; 1985) and a mass model for the LAD, its mount, and more crudely, for the remainder of the CGRO spacecraft. Prior to launch, the LAD modules were calibrated using angular response and absolute efficiency test data taken with radioactive sources (Lestrade 1989, 1991; Horack 1991). The Monte Carlo simulations were then optimized using the test data.

Scattering of source radiation off the upper atmosphere can produce substantial fluxes in near Earth-pointed detectors, when a point source is well above the horizon. For example, scattered radiation from an overhead gamma ray burst can contribute to the measured flux by as much as 50% (Pendleton et al. 1999). However, for Earth occultation, which is near line-of-sight to the horizon for the source direction, our simulations indicate that the atmospheric scattering is negligible. Therefore only the direct response matrices need be used for deconvolving fluxes as described here.

In the course of our science analysis of Earth occultation data, two significant systematic effects were found that could be traced to the response model: (1) the CONT channel boundaries were difficult to calibrate using a simple function of energy, especially below 100 keV, due to nonlinearities in the onboard analog electronics. This created unacceptably large residuals in spectral model fits and model-dependent flux measurements, and (2) the instrument response for near face-on flux measurements was under-predicted in the model. This caused fluxes for sources near the normal direction to a LAD, less than about  $20^\circ$ , to be artificially high by as much as 30%. Unfortunately, these two sources of systematic error were not understood prior to the launch of CGRO, and corrections to the response using in-flight data were complicated due to the coupling of the two effects.

Preece et al. (1994) and Pendleton et al. (1994) have used various data types to better determine the effective energies of the CONT channel boundaries. Each approach is different, and, although neither appears to be superior to the other, both schemes are an improvement over the pre-flight calibration (Lestrade 1991), which makes no adjustments for the electronic

nonlinearity. Both the Pendleton and Preece algorithms are incorporated into the analysis of BATSE occultation data. For this work, all spectra and light curves were determined using the Pendleton algorithm which optimizes the channel boundaries using Earth occultation and pulsar data in a joint analysis (Pendleton et al. 1994).

To more fully investigate the LAD response as a function of photon energy and source aspect angle, i.e., the angle between the detector normal and the source direction, the Crab Nebula occultation dataset for all eight detectors in the 16 CONT data channels at many orientations of the CGRO was used. An example of these data is shown in Fig. 13 for CONT channel 3 (40-50 keV) as a function of angle in LADs 0, 1, 2, and 3. We find that the Crab count rate is a smooth function of angle and highly reproducible. This is consistent with the Crab Nebula flux being constant to within about 5% fractional rms for the 20-100 keV band over the 5-year sampling period (see Fig. 14). The dotted curve represents the modeled response of the known Crab Nebula flux (eq. (8)), before (four top frames) and after (four bottom frames), response corrections (described below) have been applied, and the solid curve (same in top and bottom frames) represents an empirical fit used to characterize the Crab rates as a function of energy and angle (Laird et al. 1996). For all energy bands, and at intermediate aspect angles ( $\sim 20^\circ$ - $70^\circ$ ), the agreement between data and the response model is excellent. However, in the lowest CONT channels (1-3), as in part (a) of Fig. 13, the model underpredicts the actual measured Crab rate as we approach the normal direction to the detector face, yielding a flat response at angles of  $20^\circ$  or less, whereas the true response is more forward pointed as indicated by the data. This effect was partially attributed to the simplifying assumptions made in the LAD response model for the detector entrance window.

The entrance window consists of two 0.635 cm layers of a light weight aluminum-epoxy composite, called HEXEL, interleaved with other low Z (charge) materials to minimize attenuation of the low energy photons. The HEXEL provides support and optical insulation for a plastic scintillator in front of the NaI crystal for charged particle rejection. Viewed from the direction of incoming photons, the HEXEL appears as a close-packed hexagonal array, or “honeycomb” of cells. The cells are about 0.3-0.5 cm in diameter, and irregularly shaped with no alignment of cell walls between the two layers, creating a difficulty for Monte Carlo modeling. In the original response matrix generation (Pendleton et al. 1995a), the HEXEL is treated as uniform layers of aluminum of reduced effective thickness.

During the mission, we surmised that the entrance window allowed more flux into the detector than was predicted in the Monte Carlo model of the LADs. The aluminum-epoxy is very thin in the direction of the normal to the detector face, but thickens faster than  $1/\cos\theta$  as the angle increases, acting as a low energy collimator. We therefore performed calibration tests of an entrance window for the LADs at Eastern Kentucky University (EKU) (Laird et al. 1996) to quantify this effect. The results revealed an energy and angular dependence due to the double HEXEL layer consistent with the known composition of the material.

The HEXEL was found to account, however, for only a portion of the observed forward-angle response deficiency and only in the lowest three energy bands (20-60 keV). An additional detector and angular dependent effect was observed between the Crab data and model predictions over the angular range (0°-20°) and the entire energy range (20-2000 keV) of the LADs. We attribute the additional deficiency to the adoption of a power series in cosine of the aspect angle (Pendleton et al. 1995) that was used to interpolate response matrices between the Monte Carlo results at a predetermined set of angles. This function (dotted curves in part (a)) is flatter in the forward direction than the Crab data predict as shown in Fig. 13. A more physical function, including the triangular response of the HEXEL at low energies and the cosine of the geometric area (Laird et al. 1996), was used to fit the data (solid curves in part (a) and (b)) instead.

Ideally, it would be best to regenerate the response matrix model with the forward angle response properly treated, but operationally it is more convenient to consider the effects discussed above as additive, and determine an effective correction to account for the discrepancy of model and data.

Using the empirical fits as shown in Fig. 13 as a benchmark, we derived total corrections to the response model, including both the entrance window and empirical angle corrections. The response matrix is multiplied by a factor of the form

$$A \exp(-B\theta - 2\mu\tau_{eff} + 2\mu\frac{t}{\cos\theta}) \quad (9)$$

prior to spectral fitting. Here  $\tau_{eff}$  represents the effective thickness of the HEXEL derived from the EKV measurements, and  $\mu$  is the energy-dependent attenuation coefficient for aluminum. The constant A is determined by matching the model and data for each detector at 0°. The constant B, which determines the sharpness of the angular correction, was adjusted to reduce the residual difference between the dotted and solid curves in part (a) of Fig. 13. Neither A or B are energy dependent, and B has the same value for all detectors. The corrections given in eq. (9) have been incorporated into all spectra and intensity histories presented in this paper and in the catalog of low energy gamma ray sources (Harmon et al. in preparation).

A histogram of the average daily Crab Nebula fluxes as a function of time before and after the correction is shown in Fig. 14. The histogram of flux measurements after correction is more symmetric and less-skewed toward higher fluxes. The fractional rms of the measured Crab flux has dropped from about 5.2% to 4.3% in the 20-100 keV band.

### 3.6. Absolute Flux Calibration

We attempt here to perform an absolute calibration of the Earth occultation flux measurements using the Crab Nebula emission as a standard candle. We break the absolute flux determination into two parts. First, we compare Earth occultation measurements of the Crab Nebula with lunar occultations of the same source to avoid any systematic effects due to using the Earth

and surrounding atmosphere as an occulting disk, and also independent of the BATSE response model. Second, we compare observations of the Crab Nebula with other high energy instruments, assuming that the Crab is a steady source of high energy emission.

From 1993 April to 1994 January, the Crab Nebula was occulted several times by the Moon. Since the Moon has no atmosphere, lunar occultations can in principle be used to measure the absolute Crab intensity without the systematic uncertainty due to atmospheric scattering. To find when the Crab was being occulted by the Moon, we first searched for minima in the angle between the Earth-Moon vector and the unit vector to the Crab. Next we did more detailed calculations to see if the Crab was being occulted by the Moon on these days. If it was not Earth occulted, we computed the inner product  $\lambda(t)$

$$\lambda(t) = \Delta\mathbf{x} \cdot \boldsymbol{\Omega} = |\Delta\mathbf{x}| \cos \alpha \quad (10)$$

where  $\Delta\mathbf{x}$  is the vector from the *CGRO* spacecraft to the Moon, calculated every 2.048 seconds using the spacecraft position in the BATSE housekeeping data and the Moon position from the complete JPL DE-200 ephemeris (Standish et al. 1992).  $\boldsymbol{\Omega}$  is a unit vector pointed from the Moon in the direction of the Crab Nebula, and  $\alpha$  is the angle between these two vectors, as shown in Fig. 15. If  $\lambda(t) \leq 0$  then a lunar occultation is possible. The Crab is occulted by the Moon if

$$\rho^2 = |\Delta\mathbf{x}|^2 - \lambda^2 < R_{\text{Moon}}^2 \quad (11)$$

where  $R_{\text{Moon}} = 1737.4$  km is the radius of the Moon. The time of occultation is computed by linear interpolation between BATSE housekeeping records. The times of lunar occultations of the Crab and the BATSE LADs (0-7) that observed them are listed in Table 2.

To find the intensity of the Crab Nebula, lunar occultations were fitted in each energy channel and each detector with a model of same form as Eq. (1), except that we replaced the atmospheric transmission with a step model for the Crab-Moon occultation as follows. We assumed the Crab Nebula to be an extended source with uniform emission, i.e.,

$$T_n(t) = \begin{cases} 1 & \text{if } t < t_{\text{occ}} - \tau/2 \\ \pm \frac{1}{\tau}(t - t_{\text{occ}}) + \frac{1}{2} & \text{if } t_{\text{occ}} - \tau/2 \leq t \leq t_{\text{occ}} + \tau/2 \\ 0 & \text{if } t > t_{\text{occ}} + \tau/2 \end{cases} \quad (12)$$

Positive and negative signs indicate setting and rising occultations, respectively.  $t_{\text{occ}}$  is the occultation time, and the width of the occultation step in time  $\tau$  is estimated as

$$\tau = \frac{D_{\text{Crab}}}{D_{\text{Moon}}} \Delta t \quad (13)$$

where  $D_{\text{Crab}}$  is the angular extent of the Crab Nebula,  $D_{\text{Moon}}$  is the maximum angular extent of the Moon (1900"), and  $\Delta t$  is the total time the Crab is occulted by the Moon. For each pair of steps (a set and a rise), both steps were fitted simultaneously. Background data were used from

110 seconds before the first step fitted until 110 seconds after the last step fitted. An example of a fit with this model is shown in Fig. 16.

Using a grid search to find the best value of  $D_{\text{Crab}}$ , we minimized

$$\chi^2 = \sum_{p=1}^M \sum_{k=1}^{N^p} \sum_{j=1}^{N_{\text{det}}^p} \sum_{i=1}^{N_{\text{chan}}} \frac{(r_{ijkp} - y_{ijkp}(t_{kp}))^2}{\sigma_{r_{ijkp}}^2} \quad (14)$$

where  $M$  is the number of pairs of rises and sets;  $N^p$  is the number of data points for pair  $p$ ;  $N_{\text{det}}^p$  is the number of detectors viewing pair  $p$ ;  $N_{\text{chan}} = 10$  is the number of energy channels used;  $r_{ijk}$  is the BATSE count rate in energy channel  $i$  and detector  $j$  at time  $t_k$ ; and  $y_{ijkp}(t_{kp})$  is the count rate model evaluated at time  $t_{kp}$  for energy channel  $i$ , detector  $j$ , and pair  $p$ . The energy channels used correspond to 20-300 keV. Our best fit to the angular extent of the emission region of the Crab Nebula, assuming uniform emission, was  $D_{\text{Crab}} = 131'' \pm 5''$ . This agrees well with previous results from lunar occultations of the Crab (Staubert et al. 1975).

To compare BATSE Earth and Moon occultation measurements of the Crab, we used the characterization of the BATSE Earth occultation count rates for the Crab as a function of energy, aspect angle, and detector from empirical fits as shown in Fig. 13 with our fits to lunar occultations. Figure 17 shows the comparison between lunar occultations with our extended source model (Eq. 12) and Earth occultation measurements. We find that the Crab flux values from Moon occultation are on average about  $95.5(\pm 1.9)\%$  of those measured with Earth occultation. Although the results we have obtained depends on the assumed model of the Crab Nebula emission, we believe that the error due to this effect is small. The Earth occultation fluxes are systematically higher by a few percent. This could be due to the simple atmospheric model we use, which neglects scattering of source flux off the atmosphere away from the line-of-sight. Atmospheric scattering is substantial at more oblique angles to the atmosphere, and is a significant effect in determining GRB locations (Pendleton et al. 1999). For near line-of-sight scattering into the FOV of the detector at rise or set, however, we do not calculate significant contributions to account for the observed effect.

Observations of the Crab Nebula spectrum using a simple broken power law model for fitting data between 20 keV and 1 MeV have been performed with a Naval Research Laboratory balloon experiment (Strickman, Johnson, & Kurfess 1979), HEAO-1 (Jung 1989), the Oriented Scintillation Spectrometer Experiment (OSSE) on board the CGRO (Much et al. 1996; Strickman, private communication) and the Gamma-Ray Imaging Spectrometer (GRIS) (Bartlett 1994). In Fig. 18, we show the measured BATSE spectrum of the Crab Nebula compared to these measurements based on the broken power law fit, and a confidence region obtained by varying the high and low energy spectral indices, and the break energy separately by three  $\sigma$  (see Eq. (8)). The spectrum is a composite result of fitting each of the eight LADs simultaneously at times when the Crab aspect angles are  $30^\circ$  or less. The BATSE response has been corrected according to the prescription given in Eq. (9) and reduced by 4.5%, consistent with the absolute calibration by Moon occultation. We also show RXTE Proportional Counter Array (PCA) data in the 10-30 keV band, RXTE High

Energy X-Ray Telescope (HEXTE) data in the 20-200 keV band (Heindl, private communication) and BeppoSax Wide Field Camera (WFC) data (In’t Zand, private communication) in the 10-25 keV band. The BATSE data agree reasonably well with most of the other measurements of the Crab Nebula spectrum below  $\sim 200$  keV, except OSSE and GRIS.

The discrepancy between BATSE and OSSE is quite significant below  $\sim 150$  keV (15%-20%) and has been documented previously by Much et al. (1996). No adequate explanation for this has resulted from our analysis. We have eliminated the possibility of atmospheric scattering, and corrected systematic errors due to the response model. In fact, a normalization of our data to the OSSE results at 100 keV (difference is about  $\sim 16\%$ ) forces the effective area of the LAD ( $\sim 1700$  cm<sup>2</sup>) to be roughly the same as its geometric area (2025 cm<sup>2</sup>)! A comparison to other published instrumental results, with the exception of GRIS (Fig. 18), suggests that the OSSE response at lower energies (less than about 150 keV) is overestimated. The OSSE Crab Nebula spectrum tends to increase the change in photon spectral index from above and below the break energy (120-200 keV). The GRIS balloon-borne germanium detector also shows a breaking spectrum in this energy range, but the discrepancy of these data with BATSE is the largest of all instruments. Again, the reason is unknown, but underscores the difficulty in precision normalization of gamma ray astronomy telescopes which typically involve complex background and detector response effects. In our BATSE calibration exercise, we have looked for overall consistency between the eight LADs and compared the basic mechanism of occultations by the atmosphere to those by the Moon.

## 4. SEARCH TECHNIQUES FOR UNKNOWN SOURCES

### 4.1. Single Step Searches

After the data selection process as described in Sec. 2.2, a daily search of BATSE CONT data was routinely performed to find occultation features of the brightest hard X-ray/gamma ray sources below the gamma ray burst trigger level. The sensitivity of the search method depends on a variety of factors such as the shape of the source spectrum, energy bandpass, the number and orientation of detectors with respect to the source used, and the behavior of the background. Sources that reached levels of about  $4.6 \times 10^{-9}$  erg cm<sup>-2</sup> s<sup>-1</sup> (about 200 mCrab for sources with Crab-like spectra) are detectable with the step search method (see also Table 1).

Data in each LAD are first summed over the CONT data channels where the best signal-to-noise (S/N) ratio for sources with Crab-like spectra is obtained (30-200 keV). A series of fitting tests are then performed on a contiguous data segment within a fitting window of four minutes centered on a test time  $t_{occ}$ . We then determine if an occultation step is present in the background somewhere within the window. Once a segment has been tested, positive or negative results are logged for post analysis, and the window moves or “slides” to the next data segment. To

maximize the sensitivity of the sliding search, a grid of points along the Earth’s limb is calculated at  $t_{occ}$ . Using a cosine function to represent the response of the detector, the combinations of the eight LADS (out of a possible 28) with the best S/N ratio for each point are determined. These combinations are then tested at the corresponding limb points.

The first test is a linear fit over the fitting window for each LAD combination to locate deviations from a background of approximately constant slope. If the goodness of fit ( $\chi^2$ ) per degree of freedom is above a threshold (usually set to  $\geq 1.0$ ), a second fit is performed over the same fitting window using a template step function to determine if the deviation is caused by an source occultation ( $\chi^2$  required for an occultation step is typically  $\leq 1.3$ ). A third fit is then made to estimate the best time  $t_{occ}$  of the occultation and the maximum significance of a step. The significance cutoff is set to a minimum of  $2\sigma$  to avoid large numbers of spurious step detections.

The results of an occultation search for a single day are shown in Fig. 19. The significance of detected occultation steps is plotted as a LAD number (0-7) as a function of time elapsed from the beginning of the spacecraft orbit for each orbit searched. The plotted symbol corresponds to the LAD number (0-7) with the most significant step in the combination of detectors. The time zero is the time of the first data packet for the day. Plotted in this way, detected steps from the same source cluster at a specific time, although a shift of a few seconds occurs in the occultation time folded on the orbital period due to the orbital precession, which is about  $0.5^\circ$  per orbit. The times of bright source occultations, such as those for the Crab and Cygnus X-1, are shown on the plot. Significances above zero and below zero indicate rising steps and setting steps, respectively.

This method allows a quick determination of occultation times of bright transient or flaring sources from which the location of a source can be deduced from the orientation of the Earth’s limb at rise and set. In Appendices B and C we describe a graphical method for localizing a point source based on the time of occultation steps.

The single step search/graphical method for determining source locations was used primarily in the early part of CGRO mission, prior to 1993, after which we developed Earth occultation imaging to improve our ability for source localization. Two effects severely limited the sensitivity of the single step search. In the first place, orbit to orbit variations in the background make it impractical to combine raw data for different orbits. A change in the background of a few percent from one orbit to the next can induce features in the background that mimic occultation steps. Without a reliable predictor of the background or a de-trending algorithm, orbit by orbit data cannot be folded to increase the sensitivity (this is overcome in the imaging technique discussed in the next section). The second problem is the presence of sub-threshold transient features that escape the manual flagging procedure or are impractical to flag. An example is the presence of bright long-period ( $P \sim$ minutes) pulsar signals in the background data. Pulses from sources such as Vela X-1, GX 301-2 or other bright high mass binary transient systems are a source of nonstatistical noise. This problem was partially overcome by increasing the length of the fitting window and the bandpass for the search, at the expense of sensitivity to softer spectrum sources.

In general, the accuracy of the EOT for determining a source’s sky position depends very strongly on the orientation of the Earth’s limb at the time of detection. If the rising and setting limbs are nearly parallel, which is true when the source direction is very close to the orbital plane of the spacecraft, it is obvious the positional accuracy along the limb direction can be very poor. On the other hand, allowing orbital precession to move the limb geometry into a more favorable configuration, can greatly improve positional accuracy. In a situation of optimal limb geometry, the width of the occultation feature itself and the S/N ratio limits the ultimate positional accuracy. The spatial resolution perpendicular to the limb is determined by the width of the occultation step in time, which takes about  $8/\cos \beta$  seconds, where  $\beta$  is the angle of the source with respect to the orbital plane (see Appendix B). For a 90 minute orbit, the angular resolution on the sky is  $(8\text{s}/5400\text{s}) * 360^\circ$ , or  $\sim 0.5^\circ$ . Table I gives a lower limit on the positional error, considering these factors. For the step search method, the best obtainable accuracy was  $\sim 1^\circ$  with a simple step function consisting of a fitted line for the background and a steeper line with a step width of 10 seconds. We were able to improve our locational accuracy to  $\sim 0.2^\circ$  by comparing the step search results to the predicted shape of the Earth occultation features from the atmospheric attenuation model (Sec. 3.1). Usually a few iterations on the source location were required to achieve the best agreement with the data that were available at that time. Examples of the use of this method are given in Harmon et al. (1992), Pacieras et al. (1992) and Harmon et al. (1993), for the sources 4U 1543-47 ( $0.25^\circ$ ), GRO J0422+32 ( $0.68^\circ$ ), and GRO J1719-24 (=GRS 1716-249) ( $0.14^\circ$ ), respectively, where the number in parenthesis is the difference in degrees between the reported BATSE location and that of the optical counterpart from the electronic database SIMBAD.

## 4.2. Occultation Imaging

Occultation features in the time domain can be transformed into spatial information for construction of images. This enhanced the ability of BATSE to locate and identify much weaker sources than the step search algorithm permitted, and considerably increased the effectiveness of the instrument as an all-sky monitor (Zhang et al. 1993, 1994a). It also allowed us to obtain positional information more efficiently and easily for new transient sources and to discriminate between sources in crowded regions such as the galactic center.

Occultation transform imaging is conceptually similar to techniques used for many years in radio astronomy (Bracewell 1956) and medical X-ray tomography (Gullberg & Tsui 1989) to convert essentially one-dimensional scanning measurements into two-dimensional images. Using the Earth as a stable occulting disk, the limb is projected onto the sky. As the limb of the Earth (an arc, not a straight line) sweeps through a chosen region of the sky, the LADs record the counting rate as a function of time. The location of the spacecraft is well-known and thus the location and orientation of the limb projected on the sky can be determined accurately. For point sources along the limb, a change occurs in the detector counting rate as shown in Figs. 2 and 3. For a single location on the sky, the intersecting Earth’s limb will change its angle due to



precession of the spacecraft orbit. If enough one-dimensional strips are sampled, an image can be generated.

Image reconstruction is achieved via the Radon transformation (Deans 1983) and the Maximum Entropy Method (Huesman et al. 1977). Use of the Radon transformation to represent the limb projection limits sky images to a field-of-view (FOV) of about  $20^\circ$  by  $20^\circ$ . Larger images produce distortion of point source locations near the edges of the FOV.

We begin with a forward transform from the image space (sky pixels) to the data space (count rate vs. time), which is accomplished in two steps. First, a curved Radon transform is applied (Deans 1983) for the defined FOV. This is performed numerically since no analytic form is available to describe the limb arc on the sky. In the second step, a high pass Butterworth filter from the Radon space to the data space is executed using a Fast Fourier Transform (FFT). The Butterworth filter was chosen over a differential filter (Zhang et al. 1995) used in a first generation of the imaging system (Zhang et al. 1993) since it gives a better S/N ratio, 80% vs. 50%, and was also less sensitive to spikes in the background data. The data are then filtered with the same algorithm, however, the data (DISCLA) usually contain gaps due to flagging of fast timescale variations in the background, SAA passages or loss of telemetry. The best method we have found to fill data gaps is to make a simple linear interpolation. The result is a flattened data residual with bi-polar shaped features of finite width for point source occultations with the slowly-varying background components removed (Paciesas et al. 1995).

Finally, the data space to image space reconstruction is performed using the Maximum Entropy Method (MEM) (Gull & Skilling 1984). The backward transform is physically a smearing of the original image with the forward transform function, and thus defines the direction in which the iterative process converges. The Maximum Entropy Principle is used as a stopping criteria since an exact reconstruction is not achievable due to the presence of noise and imperfect sampling forced by the available limb projections.

Monte Carlo simulations have been performed to confirm the reliability and sensitivity of the images (Zhang et al. 1995). A simulated image and occultation data (after filtering) for two closely-spaced point sources using data which contain rises and sets separated by two days is shown in Fig. 20.

Examples of images are shown in Fig. 21 for sources along the galactic plane. The location accuracy near the center of a  $10^\circ \times 10^\circ$  image is  $\geq 0.3^\circ$  for a best case geometry (nearly perpendicular limb samplings), with a sensitivity in the 20-100 keV range of about  $\sim 1.1 \times 10^{-9}$  erg  $\text{cm}^{-2} \text{s}^{-1}$  (75 mCrab for a source with a Crab-like spectrum) for a one day integration. Computer memory requirements limit the number of days that can be combined into one image, although we have achieved integrations of 15-20 days, with a sensitivity between 10 and 20 mCrab. For locating a new source, generating an image such that a source is near the center of the FOV, produces a sensitivity and positional accuracy that is close to the standard flux extraction method (see Table 1). The chief advantage of imaging method is that it requires less *a priori* knowledge of a new

source location and the details of orbital precession and the presence of interfering sources are naturally taken into account. Thus the method allowed deep imaging of short-lived transients (a few days), and identification of weak high energy emission from low mass X-ray binaries (Barret et al. 1996), active galaxies (Malizia et al. 2000) and supernova remnants (McCollough et al. 1997). Examples of new transients located with this method are GRS 1009-45 (Zhang et al. 1993) ( $0.39^\circ$ ) and GRO J1655-40 (Zhang et al. 1994b) ( $0.31^\circ$ ), where the number in the parenthesis is difference in degrees from the BATSE-reported location of the source and that of the optical counterpart from SIMBAD.

## 5. CONCLUSION

We have shown various aspects of the Earth occultation technique for point source studies with the BATSE large area detectors. The technique is applicable to all-sky monitoring or obtaining time- and energy-dependent information about hard X-ray and low energy gamma ray sources, and yields positional information for point sources with moderate accuracy. It has been used successfully for several years for independent science investigations and triggering observations with other satellites and ground-based instruments. The method can be used with an uncollimated detector and without sophisticated background models. Improved background modeling, however, would allow one to increase the amount of data within the fitting window and abandon the simple polynomial fits, thus potentially increasing the sensitivity of the method. Several efforts have resulted in models that can predict backgrounds to the few percent level (Ling et al. 1996; Rubin et al. 1996b), but in practice, extracting point source fluxes in the few mCrab range using BATSE requires sub-percent level accuracy.

## 6. ACKNOWLEDGEMENTS

The authors would like to thank the BATSE Mission Operations Team for their help in preparing software and other data products, and especially Maitrayee Sahi, Burl Peterson and William Henze. B.A.H. is also especially grateful to William A. Wheaton, James C. Ling, and Duane Gruber for sharing their vast knowledge of HEAO data analysis and studies of the high energy background in gamma ray detectors. We thank Chris Laird and students at Eastern Kentucky University for measurement and characterization of the LAD entrance window. We also thank the following individuals for instrument data on the Crab Nebula: Mark Strickman, for OSSE, Keith Jahoda, for RXTE/PCA, Jean in't Zand, for BeppoSax/WFC, and William Heindl, for RXTE/HEXTE. This made research has made use of the SIMBAD database, operated at CDS, Strasbourg, France. This work was supported by the Goddard Space Flight Center Compton Gamma Ray Observatory Science Support Center, which is funded by the NASA Office of Space Science.

## A. LIST OF ACRONYMS AND ABBREVIATIONS

BATSE	Burst and Transient Source Experiment
CGRO	<i>Compton Gamma Ray Observatory</i>
CONT	large area detector continuous data
DISCLA	large area detector discriminator data
EBOP	Enhanced BATSE Occultation Package
EGS	Stanford electromagnetic cascade and transport code
EKU	Eastern Kentucky University
EOT	Earth Occultation Technique
FOV	field of view
GEANT	Southampton electromagnetic cascade and transport code
GRB	gamma ray burst
GRIS	Gamma-Ray Imaging Spectrometer
HEAO	<i>High Energy Astronomy Observatory</i>
HEXEL	honeycomb-like aluminum-epoxy composite
HEXTE	High Energy X-Ray Timing Experiment
ICAO	International Civil Aviation Organization
INTEGRAL	<i>International Gamma-Ray Astrophysics Laboratory</i>
JPL	Jet Propulsion Laboratory
LAD	large area detector
LEO	low Earth orbit
MEM	maximum entropy method
MJD	Modified Julian Date (Julian Date - 2,400,000.5)
MSFC	Marshall Space Flight Center
OSSE	Oriented Scintillation Spectrometer Experiment
PCA	Proportional Chamber Array
RXTE	<i>Rossi X-Ray Timing Explorer</i>
SAA	South Atlantic Anomaly
SD	spectroscopy detector
S/N	signal-to-noise
SOI	source of interest
TDRSS	Tracking & Data Relay Satellite System
TJD	Truncated Julian Date (Julian Date - 2,440,000.5)
WFC	Wide Field Camera

## B. BASIC FEATURES OF OCCULTATION TIMING

The geometry and timing of Earth occultations of a celestial source are most simply understood for an idealized model where the orbit of the spacecraft is assumed to be circular, the precession of the orbital plane is ignored, and the oblateness of the Earth is ignored.

The basic geometry is shown in Fig. B1. We adopt a coordinate system in which the spacecraft orbit is in the x-y plane. The source is located at an azimuthal angle  $\phi$  from the x-axis, and an angle  $\beta$  above the orbital plane. The spacecraft is located at radius  $r_{sc}$  and azimuthal angle  $\phi_{sc}$  which increases in time at a rate of  $2\pi/P_{orbit}$ . The angle  $\theta$  between the direction to the source and the direction to the Earth from the spacecraft is given by

$$\cos \theta = -\cos(\phi - \phi_{sc})\cos\beta . \quad (\text{B1})$$

As shown in Fig. B2, this angle is related to  $h$ , the minimum height of the line of sight above the surface of the Earth, by

$$r_e + h = r_{sc} \sin \theta \quad (\text{B2})$$

where  $r_e$  is the Earth radius. In the middle of an occultation step we define

$$\theta = \theta_{occ} = \sin^{-1}([r_e + h_{occ}]/r_{sc}) \quad (\text{B3})$$

where  $h_{occ}$  is the altitude for 50% transmission. For a spacecraft altitude of 500 km and an occultation altitude of 70 km,  $\theta_{occ} = 69.6^\circ$ . If the source is too far above or below the orbital plane,  $|\beta| > \theta_{occ}$ , the source is always visible and no occultations are seen. Earth spans an opening angle of  $\sim 140^\circ$ , or about 30% of the sky for a spacecraft altitude of 500 km. The oblateness of the Earth causes the CGRO orbit to precess with a cycle of about 53 days. Hence, during the precession cycle, if the angle in which a vector in the direction a source makes with the orbital plane ( $\beta$ ) exceeds  $69.6^\circ$  occultations will cease. The duration of this gap in occultation coverage is

$$\tau_{gap} = 2 \frac{P_{precession}}{2\pi} \cos^{-1} \left( \frac{\sin \theta_{occ} - \cos i \sin |\delta|}{\sin i \cos \delta} \right), \quad (\text{B4})$$

where  $\delta$  is the declination of the source,  $P_{precession}$  is the precession period,  $\theta_{occ}$  is the angle between the geocenter and the Earth's limb at 50% transmission as seen from the spacecraft, and  $i$  is the inclination of the spacecraft orbit. For a 500 km altitude orbit with  $i = 28.4^\circ$   $P_{precession} = 53.4$  days. We have then

$$\tau_{gap} = \Delta\Omega (6.74^\circ \text{ day}^{-1})^{-1} \quad (\text{B5})$$

where

$$\Delta\Omega = 2 \cos^{-1} 1.97 \sec \delta - 1.85 \tan \delta \quad (\text{B6})$$

These time gaps occur for sources with declinations in the range

$$\theta_{occ} - i < |\delta| < \pi - i - \theta_{occ} \quad (\text{B7})$$

or  $\pm(41.2^\circ$  to  $82^\circ)$ .

Otherwise, a rise and set are seen each orbit at the spacecraft azimuth angles

$$\begin{aligned}\phi_{sc}^r &= \phi - \cos^{-1}(-\cos \theta_{occ} / \cos \beta) \\ \phi_{sc}^s &= \phi + \cos^{-1}(-\cos \theta_{occ} / \cos \beta)\end{aligned}\tag{B8}$$

where the label  $r$  is for source rise,  $s$  for source set. The duration of either occultation step is given by

$$\Delta t_{occ} \approx \left(\frac{P_{orbit}}{2\pi}\right) \left(\frac{\Delta h}{r_{sc} \cos \theta_{occ}}\right) \frac{\sin \theta_{occ}}{\sqrt{\cos^2 \beta - \cos^2 \theta_{occ}}},\tag{B9}$$

where  $\Delta h$  is the difference between the 90% and 10% transmission altitudes.

If we measure the times of a pair of rising and setting occultations, we can determine the location of the source. Fig. B3 shows the projection on the sky of the limb of the Earth at the time of rise and set for a source with  $\phi = 0^\circ$  and  $\beta = 50^\circ$ . These rising and setting limbs are the locus of directions  $(\phi, \beta)$  that satisfy Eq. (B8) with  $\phi_{sc}$  fixed at its value at the source rise or set. For a given pair of rising and setting occultations there are two possible source locations, one above and one below the orbital plane. This ambiguity must be resolved by using the direction sensitivity of the detectors or other means. If the two occultation times are measured with an accuracy of  $\sigma_t$ , then the errors on the estimate for the source location can be shown to be

$$\sigma_\phi = \frac{\sigma_t}{\sqrt{2}\Delta t_{occ}} \left(\frac{\Delta h}{r_{sc} \cos \theta_{occ}}\right) \frac{\sin \theta_{occ}}{\sqrt{\cos^2 \beta - \cos^2 \theta_{occ}}},\tag{B10}$$

$$\sigma_\beta = \frac{\sigma_t}{\sqrt{2}\Delta t_{occ}} \left(\frac{\Delta h}{r_{sc} \cos \theta_{occ}}\right) \frac{\tan \theta_{occ}}{\tan \beta}.\tag{B11}$$

### C. ACCURATE OCCULTATION CALCULATIONS

Precise predictions of occultation times or calculations of the Earth limbs at given times require the use of an accurate spacecraft ephemeris, and an accurate model of the shape of the Earth. The Earth's surface is approximately an oblate ellipsoid given by

$$x^2 + y^2 + (1 - f)^{-2} z^2 = a^2\tag{C1}$$

where  $x$ ,  $y$ , and  $z$  are geocentric Cartesian coordinates with the  $z$ -axis aligned with the north pole,  $f = 1/298.257$  is the flattening factor of the Earth, and  $a = 6378.136$  km is the Earth's equatorial radius. Near the Earth's surface, constant atmospheric density surfaces can be approximated by ellipsoids of the same oblateness. If the spacecraft is at position  $R = (x_{sc}, y_{sc}, z_{sc})$ , the source is in direction  $\Omega = (\Omega_x, \Omega_y, \Omega_z)$ , and the height  $h(s)$  above the surface of a point on the line of sight at a distance  $s$  from the spacecraft, then we have

$$(a + h(s))^2 = (x_{sc} + s\Omega_x)^2 + (y_{sc} + s\Omega_y)^2 + (1 - f)^{-2}(z_{sc} + s\Omega_z)^2.\tag{C2}$$

The minimum height, and its distance along the line of sight is given by

$$h_{min} = \left[ x_{sc}^2 + y_{sc}^2 + (1-f)^{-2} z_{sc}^2 - \frac{(x_{sc}\Omega_x + y_{sc}\Omega_y + (1-f)^{-2} z_{sc}\Omega_z)^2}{\Omega_x^2 + \Omega_y^2 + (1-f)^{-2}\Omega_z^2} \right]^{1/2} - a, \quad (\text{C3})$$

$$s_{min} = -\frac{x_{sc}\Omega_x + y_{sc}\Omega_y + (1-f)^{-2} z_{sc}\Omega_z}{\Omega_x^2 + \Omega_y^2 + (1-f)^{-2}\Omega_z^2}. \quad (\text{C4})$$

If  $s_{min}$  is negative, then the minimum occurs in the direction from the spacecraft away from the source, and the source is visible, since that spacecraft is above any significant atmosphere.

To accurately calculate the projection of the Earth’s limb on the sky at a given time, we take advantage of a linear transformation that maps the oblate Earth into a sphere. For a vector  $\mathbf{X}$  we set

$$x = X_x, \quad y = X_y, \quad \text{and} \quad z = (1-f) X_z. \quad (\text{C5})$$

Then Eq. (C1) reduces to  $|\mathbf{X}|^2 = a^2$ . The transformed geometry of the occultation is like that discussed in Appendix A. Given the spacecraft position  $R$  and velocity  $V$ , we compute a set of orthonormal (in the transformed space) basis vectors:

$$\mathbf{e}_1 = \mathbf{R}/|\mathbf{R}| \quad (\text{C6})$$

$$\mathbf{e}_3 = \mathbf{R} \times \mathbf{V}/|\mathbf{R} \times \mathbf{V}| \quad (\text{C7})$$

$$\mathbf{e}_2 = \mathbf{e}_3 \times \mathbf{e}_1 \quad (\text{C8})$$

Then with  $\theta_{occ} = \sin^{-1}([a + h_{occ}]/|\mathbf{R}|)$  we compute the direction vectors

$$\mathbf{\Omega}(\psi) = -\mathbf{e}_1 \cos \theta_{occ} + \mathbf{e}_2 \sin \theta_{occ} \cos \psi + \mathbf{e}_3 \sin \theta_{occ} \sin \psi \quad (\text{C9})$$

where the parameter  $\psi$  ranges from  $-\pi/2 < \psi < \pi/2$  for the rising limb, and  $\pi/2 < \psi < 3\pi/2$  for the setting limb. After transforming the direction vectors back to our original coordinate system we then compute right ascensions  $\alpha(\psi)$  and declinations  $\delta(\psi)$  along the limb of the earth:

$$\alpha(\psi) = \tan^{-1}(\mathbf{\Omega}_2(\psi)/\mathbf{\Omega}_1(\psi)) \quad (\text{C10})$$

$$\delta(\psi) = \tan^{-1}((1-f)\mathbf{\Omega}_3(\psi)[\mathbf{\Omega}_1^2(\psi) + \mathbf{\Omega}_2^2(\psi)]^{-1/2}). \quad (\text{C11})$$

The precession of the plane of the spacecraft orbit causes the orientation of the rising or setting limb passing through a source to change cyclically with the precession period ( $\sim 50$  days for a near Earth orbit with  $23^\circ$  inclination). If limbs are plotted for a new source for a number of days, the precession allows the location ambiguity discussed in appendix B to be resolved.

## REFERENCES

Aschwanden, M. J., Schwartz, R. J., & Dennis, B. R. 1998, ApJ, 502, 468

- Barret, D. et al. 1996, A&AS, 120C, 121
- Bartlett, L. M. et al. 1994, "High Resolution Gamma-Ray Spectroscopy of the Crab", Ph. D. Dissertation, University of Maryland
- Bildsten, L. et al. 1997, ApJS 113, 367
- Bracewell, R. N. 1956, Aus. J. Phys., 9, 198
- Bradt, H. V., Rothschild, R. E., & Swank, J. H. 1993, A&AS, 97, 355
- Brandt, S. 1994, Ph.D. Thesis, Copenhagen University Observatory
- Briggs, M. S. 1995, in Proc. of the Third Huntsville Symp on Gamma Ray Bursts, AIP Conf. Proc. 384, ed. Kouveliotou, C., Briggs, M. S., & Fishman, G. J. (AIP: New York), 133
- Castro-Tirado, A. J. 1994, Ph.D. Thesis, University of Copenhagen
- Chupp, E. L. 1975, *Gamma Ray Astronomy*, (D. Reidel, New York), p. 278
- Conner, J. P., Evans, W. D., & Belian, R. D. 1969, ApJ, 157, L157
- Deans, S. R. 1983, *The Radon Transform and Some of Its Applications* (Wiley Press).
- Finger, M. H., Wilson, R. B., & Harmon, B. A. 1996, ApJ, 459, 288
- Fishman, G. J. & Austin, R. W. 1976, NIM, 140, 193
- Fishman, G. J., Meegan, C. A., Parnell, T. A., & Wilson, R. B. 1982, in *Gamma-Ray Transients and Related Astrophysical Phenomena*, eds. R. E. Lingens, H. S. Hudson, & D. M. Worrall, AIP Conf. Proc. 77, (AIP: New York), 443
- Fishman, G. J., Meegan, C. A., Parnell, T. A., Wilson, R. B., & Paciesas, W. S. 1984, in *High Energy Transients in Astrophysics*, ed. S. E. Woosley (AIP: New York), 651
- Fishman, G. J. et al. 1989, in the *Gamma Ray Observatory Science Workshop*, Goddard, Greenbelt ed. N. Johnson, (unpublished), Sec. 3, p. 47
- Fishman, G. J. et al. 1994a, NASA Report N96-11316
- Fishman, G. J. et al. 1994b, ApJS, 92, 229
- Ford, R. et al. 1978, Stanford Univ., SLAC-210
- Ford, R. et al. 1985, stanford Univ., SLAC-265
- Gehrels, N. & Shrader, C. R., 1997, in *X-ray Imaging and Spectroscopy of Cosmic Hot Plasmas*, Proc. of an International Symp. on X-Ray Astronomy, Tokyo, ed. F. Makino & K. Mitsuda, 593
- Giacconi, R., Murray, S., Gursky, H., Kellogg, E., Schreier, E., Tananbaum, H. 1972, ApJ, 178, 281
- Gull, S. F. & Skilling, J. 1984, IEEE Proc., 131, 646
- Gullberg, G. T. & Tsui, B. M. 1989, *Information Processing in Medical Imaging* Ed. by C. N. deGraaf & M. A. Viergeren, 181 (Plenum Press, New York) 181-189.

- Harmon, B. A., Finger, M. H., Rubin, B., Mallozzi, R., Paciesas, W. S., Wilson, R. B., Fishman, G. J., Brock, M., & Meegan, C. A. 1992, NASA CP-3137, in *The Compton Observatory Science Workshop*, ed. C. R. Shrader, N. Gehrels, & B. Dennis, 69
- Harmon, B. A. et al. 1993, AIP Conf. Proc. 280, *Compton Gamma Ray Observatory*, ed. M. Friedlander, N. Gehrels & D. J. Macomb (AIP: New York), 314
- Harmon, B. A. et al. 1992 IAUC 5504
- Harmon, B. A. et al. 1993 IAUC 5874
- Harmon, B. A. et al. 1994, ApJ, 425, L17
- Holt, S. 1976, Ap. Sp. Sci. 42, 123
- Horack, J. M. 1991, NASA Ref. Pub. 1268
- Huesman, R. H. et al. 1977, *Donner Algorithms for Reconstruction Tomography*, LBL Publ. 214, 42-44
- Jung, G. V. 1989, ApJ, 338, 972
- Kniffen, D. A. & Gehrels, N., 1997, in *Proc. of the Fourth Compton Symp.*, AIP Conf. Proc. 410, ed. Dermer, C. D., Strickman, M. S., & Kurfess, J. D. (AIP: New York), 524
- Kouveliotou, C. et al. 1996, *Nature* 379, 799
- Laird, C. E. 1996, NASA ADS Conference Report, 1996N98-96174
- Lampton, M., Margon, B., & Bowyer, S., 1976, ApJ, 208, 177
- Lei, F. et al. , 1999, *Astroph. Letts & Comm.*, 39, 373
- Leonard, P. J. T. & Wanjek, C., 2000 July, S&T 100, 48
- Lestrade, J. P. 1989, “Calibration of the Burst and Transient Source Experiment”, unpublished
- Lestrade, J. P. 1991, “Energy-Channel Calibration of the Burst and Transient Source Experiment: The Data”, unpublished
- Levine, A. M. et al. 1996, ApJ, 469, L33
- Ling, J. C. et al. 1996, A&AS 120C, 677
- Ling, J. C. et al. 2000, ApJS 127, 79
- Lund, N. 1986, SPIE, 597, 95
- Malizia, A. et al. 2000, ApJ, 531, 642
- Mallozzi, R. S. et al. 1993, AIP Conf. Proc. 280, 1122
- McCullough, M. et al. 1997, in “Transparent Universe”, eds. C. Winkler, T.J.-L. Courvoisier, & Ph. Durouchoux, (ESA: Netherlands), SP-382, 547
- McNamara, B. J., Harmon, B. A., & Harrison, T. E. 1995, AAS, 111, 587
- McNamara, B. J. et al. 1998, ApJS, 116, 287



- Meegan, C. A. et al. 1992, *Nat*, 355, 143
- Much, R. et al. 1996, *A&AS*, 120C, 703
- Paciesas, W. S., Wilson, R. B., Fishman, G. J., & Meegan, C. A. 1985, in *Proc. 19th ICRC*, LaJolla, 351
- Paciesas, W. S. et al. 1992 *IAUC* 5580
- Paciesas, W. S. et al. 1995, in *Imaging in High Energy Astronomy*, (Kluwer: Amsterdam), 247
- Paciesas, W. S. et al. 1998, in *Gamma Ray Bursts: Fourth Huntsville Symposium*, AIP Conf. Proc. 428, eds. C. A. Meegan, R. D. Preece, & T. M. Koshut (New York: AIP), 466
- Pendleton, G. N. et al. 1994, *Proc. of the 2nd Compton Gamma-Ray Observatory Symposium*, AIP Conf. Proc. 304, eds. C. Fichtel, N. Gehrels, J. Norris, (AIP: New York), 749
- Pendleton, G. N. et al. 1995a, *NIM*, A364, 567
- Pendleton, G. N. et al. 1995b, *ApJ*, 439, 963
- Pendleton, G. N. et al. 1999, *ApJ*, 512, 362
- Preece, R. et al. 1994, *Proc. of the 2nd Gamma Ray Burst Workshop*, AIP Conf. Proc. 307, eds. G. J. Fishman, J. J. Brainerd, & K. Hurley, (AIP: New York), 266
- Press, W. H., Teukolsky, S. A., Vetterling, W. T., & Flannery, B. P., 1992, *Numerical recipes in Fortran, The Art of Scientific Computing*, 2nd Ed., (Cambridge University: New York), 678
- Robinson, C. R. et al. 1997, in *Proc. of Second INTEGRAL Workshop*, SP-382, eds. C. Winkler, T. J.-L. Courvoisier, & Ph. Durouchoux, (ESA: Noordwijk), 249
- Rubin, B. C. et al. 1996a, *ApJ*, 459, 259
- Rubin, B. C. et al. 1996b, *A&AS*, 120C, 687
- Rubin, B. C. et al. 1998, *ApJ*, 492, L67
- Shaw, S., et al. , 2000, *Proc. of the 4th INTEGRAL Workshop*, Alicante, Spain, astro-ph/0101035
- Skelton, R. T., Ling, J. C., Radocinski, R., & Wheaton, W. A., 1994, *Proc. of the 2nd Compton Gamma-Ray Observatory Symposium*, AIP Conf. Proc. 304, eds. C. Fichtel, N. Gehrels, J. Norris, (AIP: New York), 758
- Standish, E. M., Newhall, X. X., Williams, J. G., & Yeomans, D. K. 1992, *Orbital Ephemerides of the Sun, Moon, & Planets*, in *Explanatory Supplement to the Astronomical Almanac*, ed. P. K. Seidelmann (Mill Valley:University Science Books), 297
- Staubert, R. et al. 1975, *ApJ*, 201, L15
- Storm, E. & Israel, H. I. 1970, *ND Tab.*, A, 7, 565
- Strickman, M. S., Johnson, W. N., & Kurfess, J. D. 1979, *ApJ*, 230, L15
- Sunyaev, R. A. & Titarchuk, L. G. 1980, *A&A*, 86, 121

- Tsunemi, H., Kitamoto, S., Manabe, M., Miyamoto, S., Yamashita, K., & Nakagawa, M. 1989, PASJ, 41, 391
- U.S. Committee on Extension to the Standard Atmosphere 1962, U.S. ICAO Standard Atmosphere to 20 Kilometers, (Washington, U.S. Gov. Printing Office), 278 pp
- Valinia, A. & Marshall, F. E. 1998, ApJ, 505, 134
- Wheaton, W. A. et al. 1982, in “Gamma Ray Transients and Related Astrophysical Phenomena”, AIP Conf. Proc. 77, eds. R. E. Lingensfelter, H. S. Hudson, & D. M. Worrall, (AIP: New York), 77
- Wheaton, W. A. et al. 1995, ApJ, 438, 322
- Wilson, R. B., Harmon, B. A., Finger, M. H., Fishman, G. J., Meegan, C. A., & Paciesas, W. S. 1992, NASA CP-3137, in The Compton Observatory Science Workshop, ed. C. R. Shrader, N. Gehrels, & B. Dennis, 35
- Woods, P. et al. 1999, ApJ, 527, L47
- Zhang, S. N., Fishman, G. J., Harmon, B. A. & Paciesas, W. S. 1993, Nat 366, 245
- Zhang, S. N. et al. 1993, IAUC 5864
- Zhang, S. N. et al. 1994a, ITNS, 41, 1313
- Zhang, S. N. et al. 1994b, IAUC 6046
- Zhang, S. N. et al. 1995, Exp. Astron. 6, 57
- Zhang, S. N. et al. 1997, ApJ, 477, L95

### FIGURE CAPTIONS

Fig. 1.— (a) The Compton Gamma Ray Observatory showing placement of the Burst and Transient Source Experiment detector modules. (b) Major components of the BATSE detector modules (one of eight).

Fig. 2.— DISCLA data (1.024 s resolution) in low and high energy bands at times in which the viewing directions toward the Crab Nebula and the binary system A 0535+26 were close to face-on in a large area detector. To make the occultation steps more clearly seen, zero suppression has been applied to the vertical axes. (a) Approximately 7000 seconds of data in the 20-50 keV band, where the background is dominated by diffuse sky flux and earth shadowing. Crab occultation steps can be seen at  $\sim 550$ s (rise), 6050s (rise), and 4000s (set). (b) the same detector in the 100-300 keV band, where the background is dominated by variations in the flux of secondary cosmic ray flux modulated by the local magnetic field of the Earth, and (c) 20-50 keV band data containing a rise and a set from occultation of the Be star/X-ray pulsar system A 0535+26. Data are from a giant outburst in 1994 Jan-Mar. Individual pulses (period 110 s) can clearly be seen between the rising and setting features. Gaps in the data coverage result from either filtering or temporary loss of telemetry from CGRO to TDRSS (NASA Tracking and Data Relay Satellite System).

Fig. 3.— Earth occultation step features for sources shown with a fit to a quadratic model plus source terms modeled using attenuation by the atmosphere, where the fit assumes the background is continuous before and after the step, and a linear fit, with independent slopes on either side of the step. All fits are in CONT channel 4 (50-70 keV), (a) and (b) show Crab steps and (c) and (d) show steps from the transient black hole candidate GRO J0422+32 with Crab steps within the four minute fitting window. The linear model gives similar results for the size of the step to the quadratic model except in the case of (c) where the presence of the Crab step induces a systematic error in the measurement of the GRO J0422+32 step. Vertical dotted lines represent the computed occultation time for 100 keV photons at 50% transmission using the method described in Appendix B.

Fig. 4.— Examples of count spectra and model fit residuals obtained from CONT data for the sources (a) Crab Nebula supernova remnant for TJDs 9783-9797 (b) the black hole candidate Cygnus X-1 for TJDs 10427-10434 in its low (hard) state (c) the transient black hole candidate GRO J1655-40 for TJDs 10322-10332 in its high or very high state and (d) and the neutron star high mass binary Vela X-1 for TJDs 10413-10420. The dashed histograms represent the best fitting photon model folded through the detector response. Each observation includes two or more LADs with angles between the source and the detector normal vector of less than  $60^\circ$ . Residuals (measured counts - model counts) in sigmas are shown in the lower frame. The models and best fit parameters are given in the caption of Fig. 5.

Fig. 5.— Examples of spectra in photon space derived from the count spectra of Fig. 4 for the (a) Crab Nebula supernova remnant for TJDs 9783-9797 (b) the black hole candidate Cygnus X-1 for

TJDs 10427-10434 in its low (hard) state (c) the transient black hole candidate GRO J1655-40 for TJDs 10322-10332 in its high or very high state and (d) and the neutron star high mass binary Vela X-1 for TJDs 10413-10420. All data and model results are in units of photons  $\text{cm}^{-2}\text{s}^{-1}\text{keV}^{-1}$ . For (a) a broken power law was used with a goodness of fit 49.85 for 38 d.o.f. and parameters: norm =  $(3.46 \pm 0.023) \times 10^{-3}$ @45 keV,  $\alpha_1 = -2.08 \pm 0.015$ , break energy =  $136 \pm 15$ ,  $\alpha_2 = -2.43 \pm 0.056$ . For (b) the Sunyaev-Titarchuk Comptonization model was used (Sunyaev & Titarchuk 1980) with a goodness of fit 90.55 for 39 d.o.f. and parameters: norm =  $(2.33 \pm 0.16) \times 10^{-4}$ , kT =  $49.4 \pm 1.2$  keV and the optical depth  $\tau = 2.65 \pm 0.067$  for a spherical plasma. For (c) a single power law was used with a goodness of fit of 59.53 per 54 d.o.f. and parameters norm =  $(2.09 \pm 0.053) \times 10^{-4}$ @100 keV,  $\alpha = -2.70 \pm 0.036$ . For (d) an optically thin thermal bremsstrahlung model was used with a goodness of fit of 11.6 per 16 d.o.f. and parameters norm =  $(5.31 \pm 2.2) \times 10^{-6}$ @100 keV, kT =  $14.6 \pm 1.4$ .

Fig. 6.— (a) Examples of multi-year intensity histories (1991 April- 1998 July) for four persistent sources (from top to bottom) the Crab supernova remnant (40-150 keV), the high mass binary pulsar Vela X-1 (20-50 keV), the black hole candidate GX 339-4 (20-100 keV), and the radio galaxy Centaurus A (20-200 keV) obtained with the Earth occultation technique. Each data point represents an average of occultation steps obtained for that day or several days. (b) intensity histories for four transient sources (from top to bottom) GRO J0422+32 (X-Ray Nova Persei 1992) (40-150 keV), the high mass binary 2S 1417-624 (20-50 keV), GRO J1655-40 (X-Ray Nova Scorpii 1994) (20-200 keV) and GRO J1719-24 = GRS 1716-249 (X-Ray Nova Ophiuchi 1993) (20-100 keV).

Fig. 7.— Sensitivity ( $3\text{-}\sigma$ ) for a two-week observation of a source averaging 16 occultations a day with contributions from two LADs, as a function of energy. Energy bins correspond to CONT channel boundaries. The Crab Nebula total emission spectrum measured with HEAO-A4 (Eq. (8)) (Jung 1989) is shown for comparison.

Fig. 8.— Sensitivity curves ( $3\text{-}\sigma$ ) for a two-week observation with the LADs as a function of angle from the normal vector of the LAD entrance window for combinations of one (continuous curves), two (lower rows of diamonds), three and four LADs (higher rows of diamonds). Three different energy channels are shown.

Fig. 9.— Sky regions near the (a) Crab Nebula and (b) the black hole candidate Cyg X-1. Superimposed are shaded regions which represent the portion of the sky subject to Earth occultation when the Earth’s limb crosses the Crab or Cyg X-1. Other sources which are routinely monitored with BATSE are also shown. See text for a more detailed explanation.

Fig. 10.— (a) Angle between the closest approach points of a given source location, here GRO J0422+32, with the rising (top frame) and setting (middle frame) limbs of the Crab Nebula as a function of time for the period TJD 9800-10000. The corresponding light curve of GRO J0422+32 for the same period is also shown (bottom frame). Note that the closest approach of the setting limb of the Crab to GRO J0422+32 is about  $3^\circ$ . (b) Same type of plot for the source 4U 0614+091. Note

that setting limb of the Crab periodically crosses the location of 4U 0614+091, when occultations occur at the same time for both sources.

Fig. 11.— Sky grid, consisting of 162 points, used for determination of location-dependent systematic error.

Fig. 12.— Centroids in photons  $\text{cm}^{-2}\text{s}^{-1}$  and width (in  $\sigma$ s) of the light curves for the grid locations shown in Fig. 10 as a function of galactic longitude.

Fig. 13.— Crab Nebula count rates in CONT channel 3 (40-50 keV) for LADs 0, 1, 2, and 3 as a function of the angle from the detector normal. Data are binned in 10-degree steps and weighted by the measured errors. In the four top frames, the dotted curves represent the original detector response function folded with the known Crab spectrum (eq. (8)) before the correction given in eq. (9) was applied and, in the bottom four frames, the dotted curves represent the response after the correction was applied. The solid curve (same in the top and bottom frames) is an empirical fit to the Crab count data which reflects both the triangular response of the entrance window and the cosine-like response due to the reduction in geometric area toward the radiation source.

Fig. 14.— Histograms of the Crab Nebula daily average fluxes in photons  $\text{cm}^{-2}\text{s}^{-1}$  for the 20-100 keV band before (upper frame) and after (lower frame) the response corrections in eq. (9) were applied. The histograms show the difference in the centroid and width of the distribution of flux measurements.

Fig. 15.— Illustration of the geometry of a lunar occultation of the Crab.

Fig. 16.— Example of fits to BATSE CONT 40-50 keV data for LAD 7 for lunar occultations of the Crab using an extended source model for the Crab.

Fig. 17.— Ratio of Crab lunar occultations to Crab Earth occultations integrated over the 20-320 keV energy band. Each point represents the ratio of the average integrated intensity from lunar occultations to that of Earth occultations for each detector and each day.

Fig. 18.— Comparison of various instrument data for high energy observations of the Crab Nebula. The shaded region represents a variation in the parameters of the broken power law fit, and data from various instruments used by permission (see text).

Fig. 19.— Results of the occultation step search. The horizontal axis represents the time elapsed from the start of the CGRO orbit and the vertical axis is the significance of the detection (size of the step in counts divided by the uncertainty). The number on the plot represents the number of the LAD in which the most significant step of a detector combination was found. Times of bright source occultations are indicated on the plot, which correlate with the larger number of aligned

bright steps detected by the algorithm.

Fig. 20.— A simulated image and associated occultation data in the time domain (after filtering) for two closely-spaced point sources. Background data are taken from one orbit on TJD 9573 and one orbit on TJD 9575 (two rises and two sets) and combined with a simulated source signal. This illustrates how a change in limb geometry can be used to distinguish sources within a few degrees of each other.

Fig. 21.— Examples of Earth occultation transform imaging for various regions along the galactic plane.

Fig. 22.— Geometry of occulting source relative to the spacecraft orbit.

Fig. 23.— Geometry of the line of sight from the spacecraft to the source.

Fig. 24.— The rising and setting limbs for a source at  $\phi = 0^\circ$  and  $\beta = 50^\circ$ .

Table 1. Comparison of BATSE Earth Occultation Measurement Techniques

Occultation Technique	Source Location Assumption	Datatype	Typical Energy & Channel Ranges <sup>a</sup>	Sensitivity (3 $\sigma$ -1 day) (30-250 keV) $10^{-9}$ erg cm <sup>-2</sup> s <sup>-1</sup>	Source Localization Error(1 $\sigma$ ) <sup>b</sup>
Step Fit w/ atmos. model	known ...	CONT chans 1-14	20-1800 keV ...	1.1 ...	$\gtrsim 0.2^\circ$
Step Search ...	unknown <sup>c</sup> ...	CONT chans 2-8	30-250 keV ...	4.6 ...	$\gtrsim 1^\circ$
Transform Imaging ...	unknown <sup>c</sup> ...	DISCLA chans 1-3	20-300 keV ...	1.1 ...	$\gtrsim 0.3^\circ$

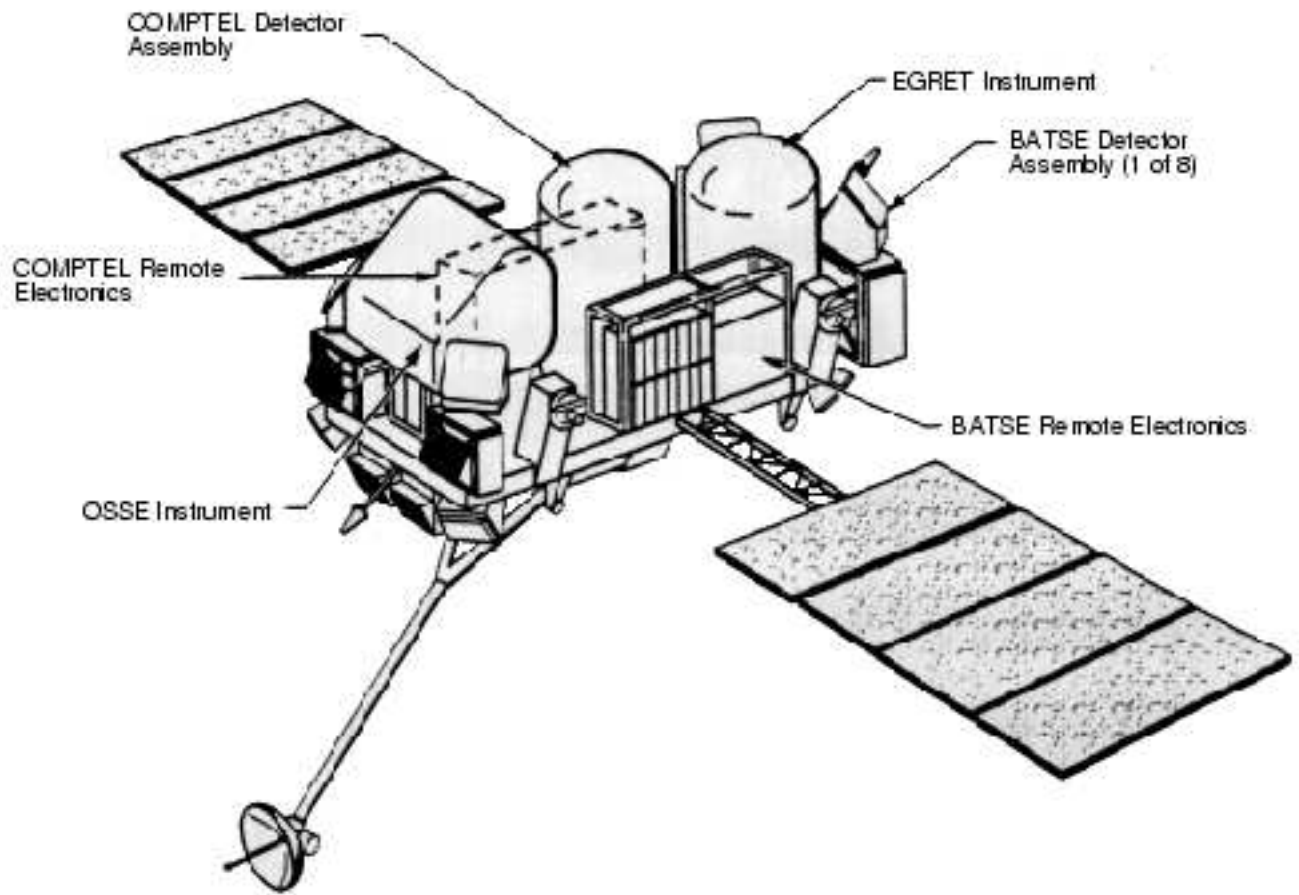
<sup>a</sup>Channel range is selectable.

<sup>b</sup>Quoted error assumes optimal limb geometry for rise and set, which should be regarded as a lower limit.

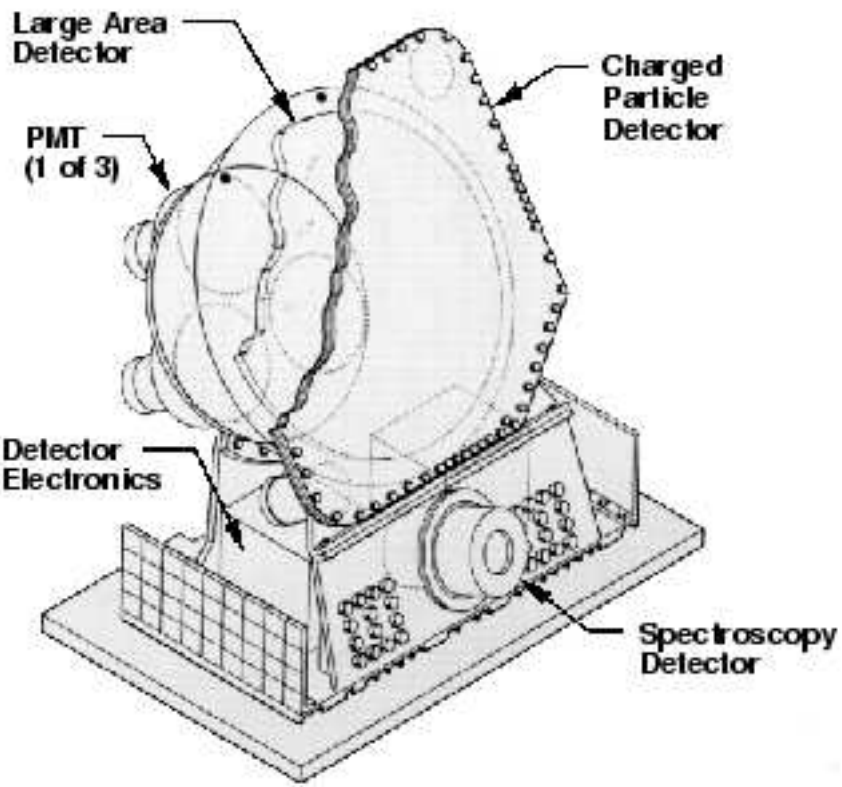
<sup>c</sup>Detection of unknown weak sources may be improved by prior subtraction of known step-fit sources.

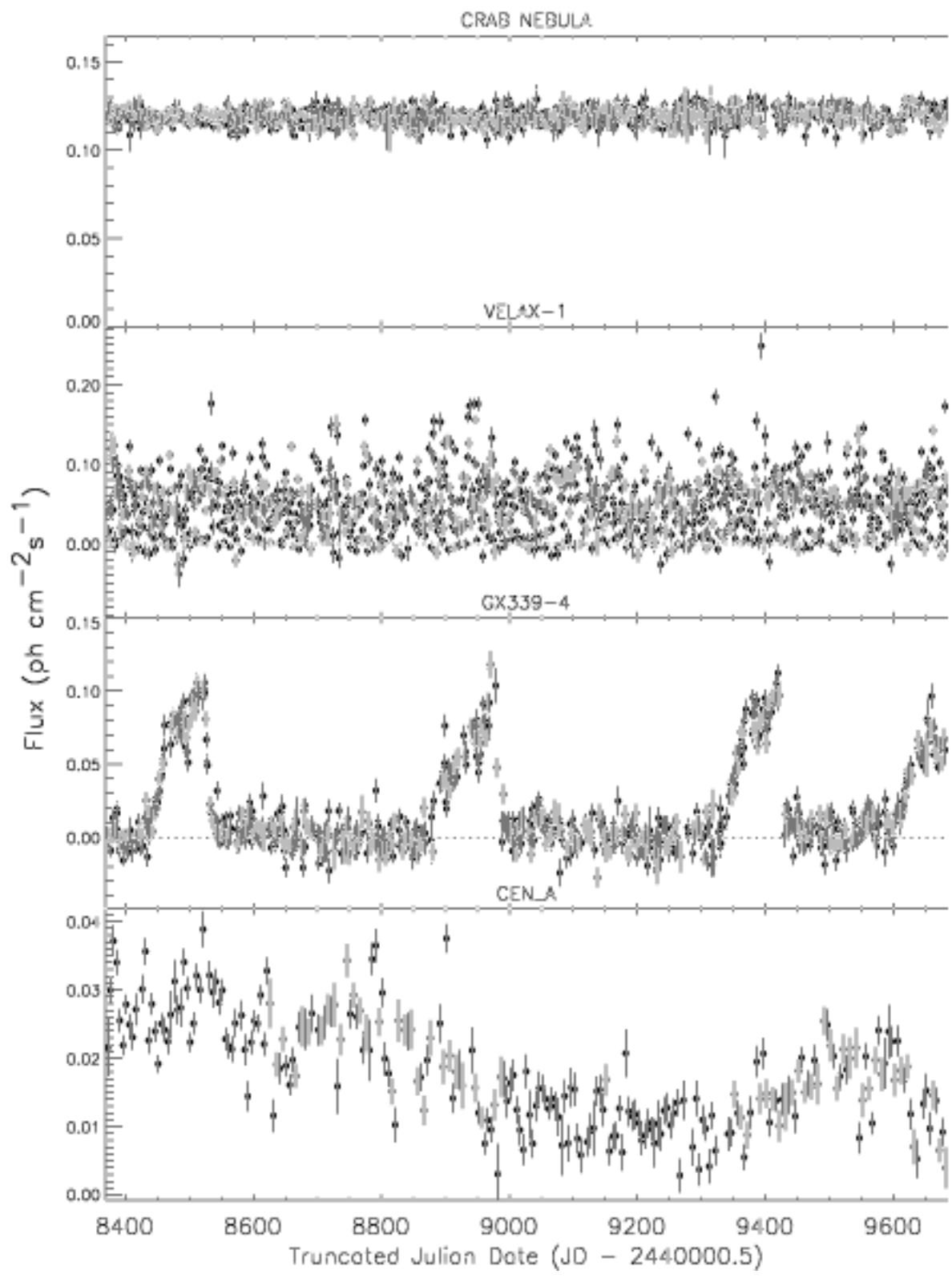
Table 2. Times of lunar occultations of the Crab Nebula in BATSE CONT data.

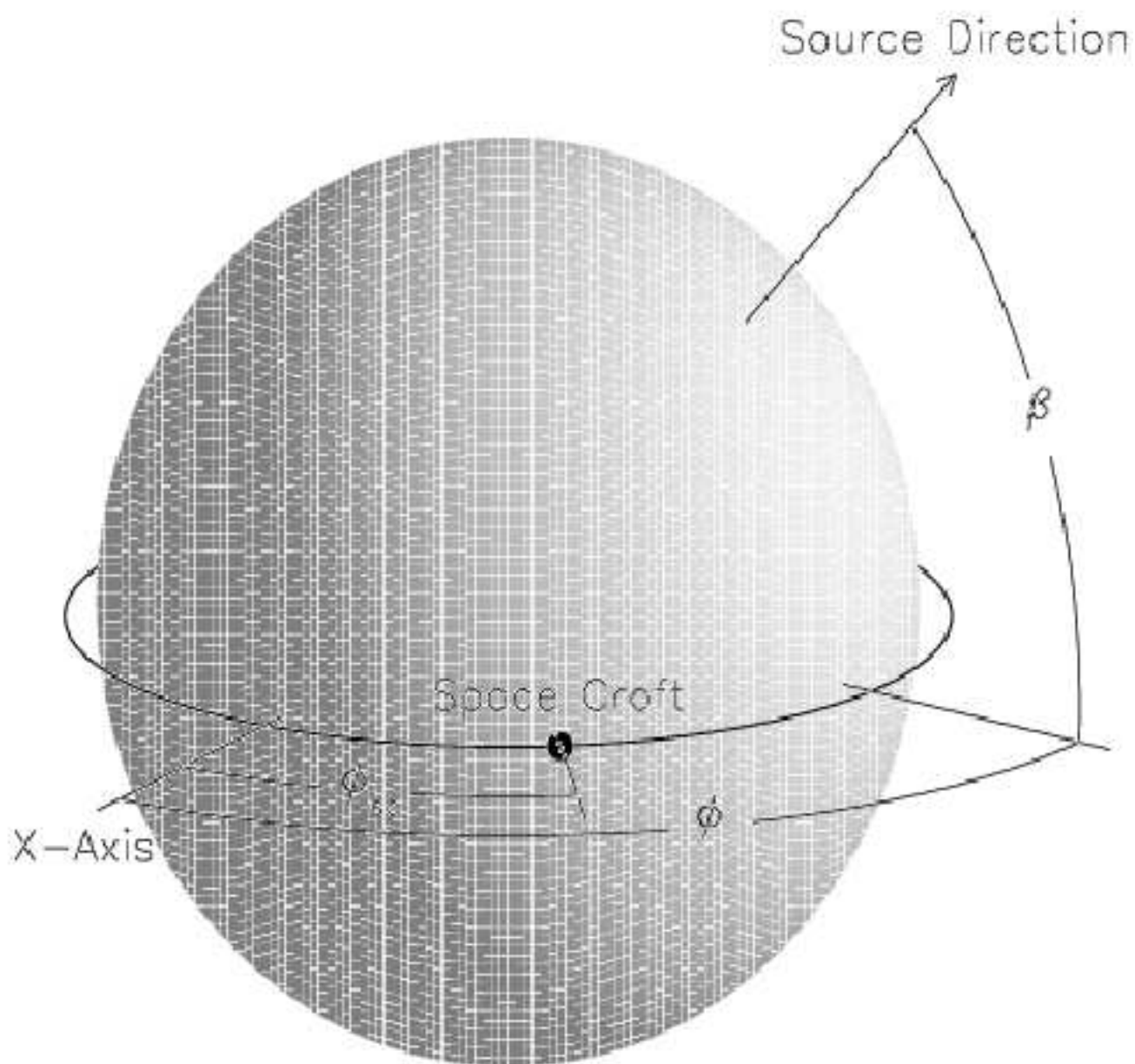
Day (TJD)	Set Time (secs)	Rise Time (secs)	LADs Viewing the Crab
9103	10645	11150	0, 1
9212	39061	39487	1, 3, 5, 7
9239	74328	74543	1, 3, 5, 7
9376	20809	21036	5, 7
9376	27098	27633	5, 7

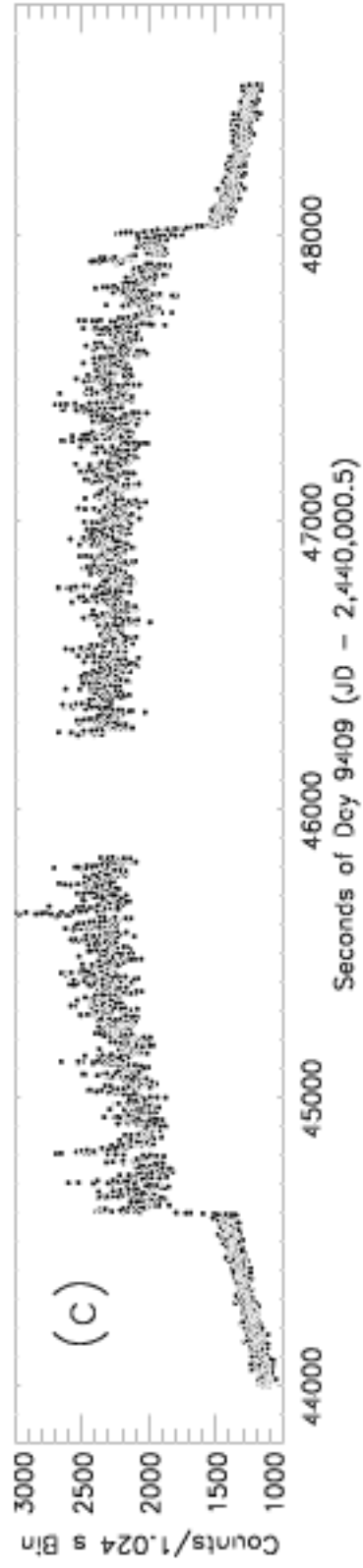
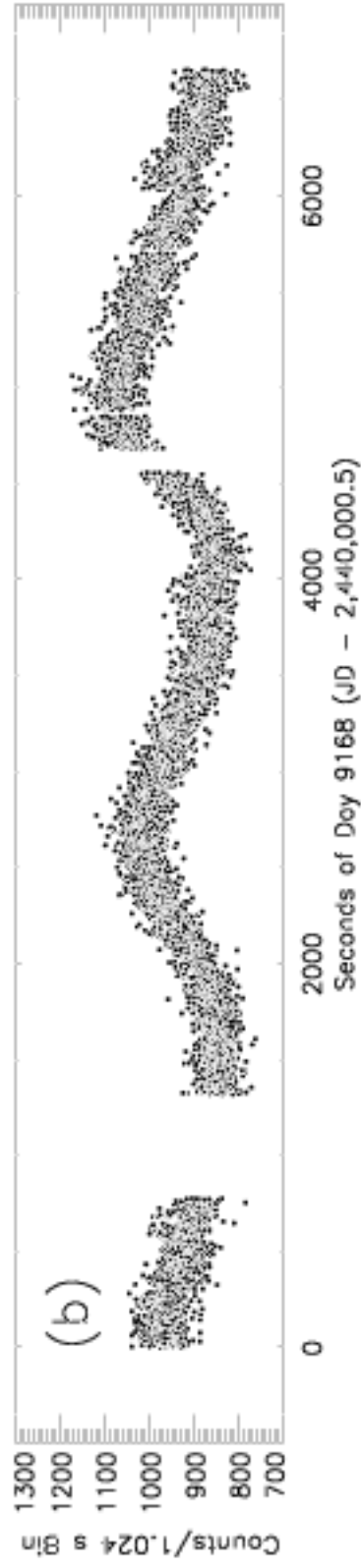
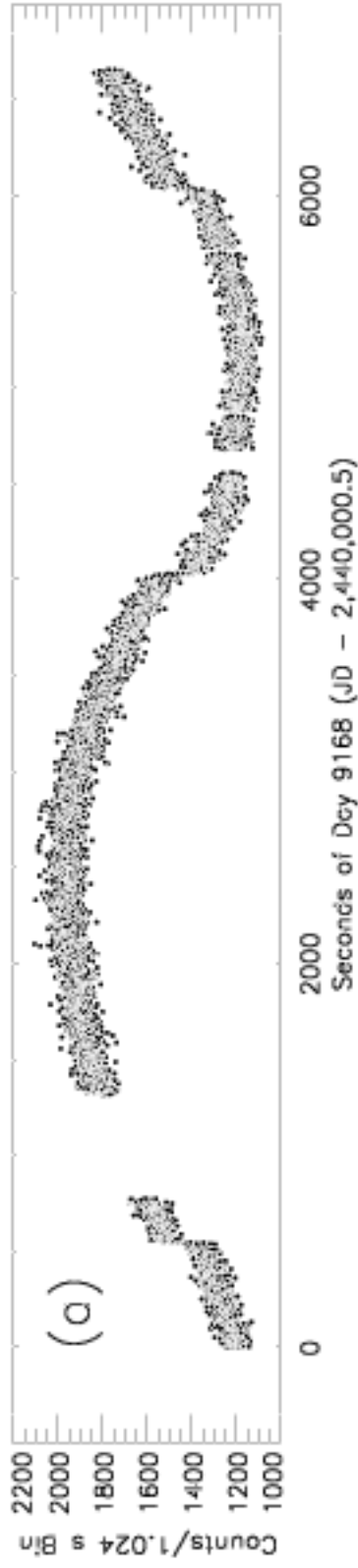


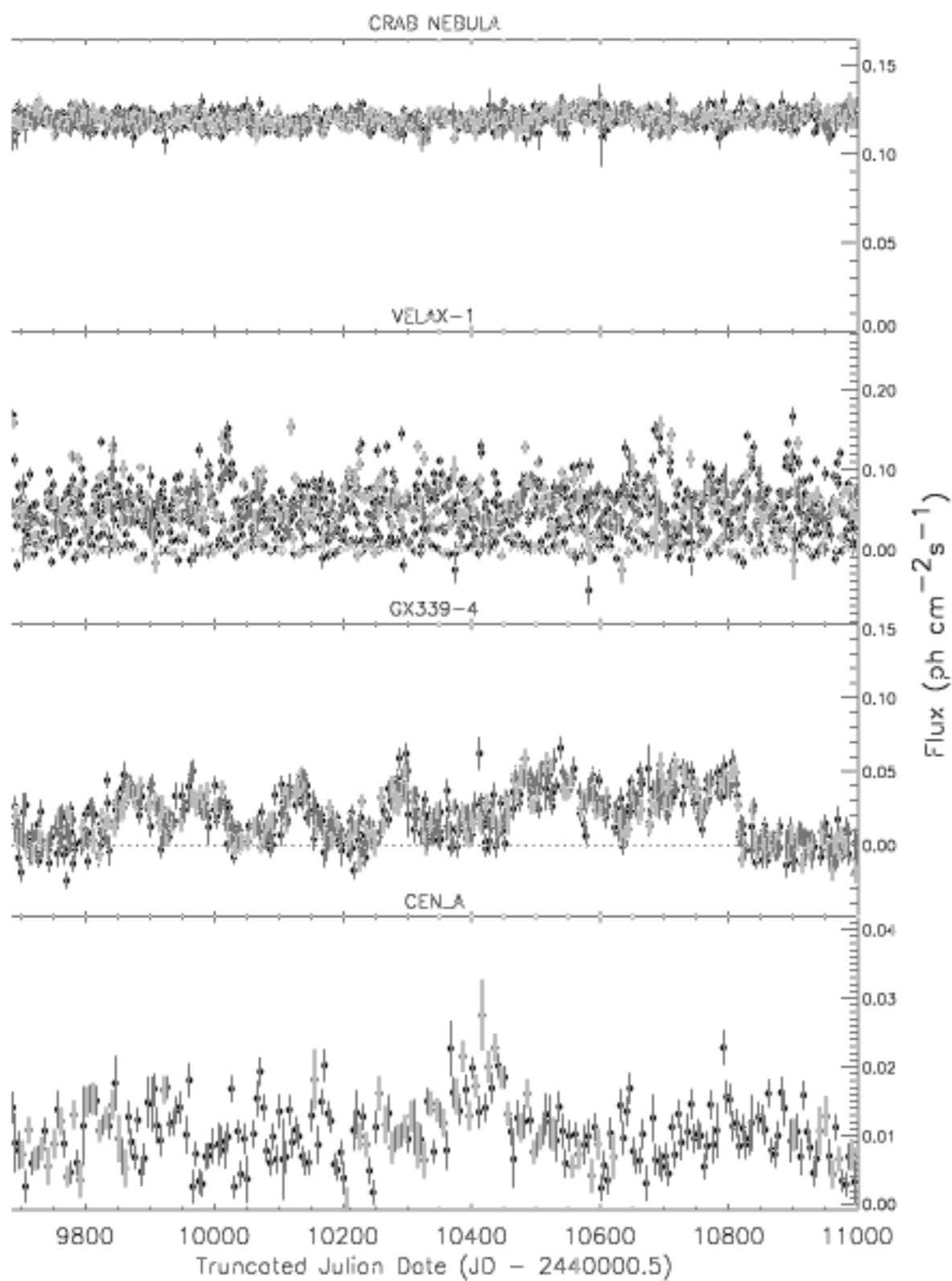


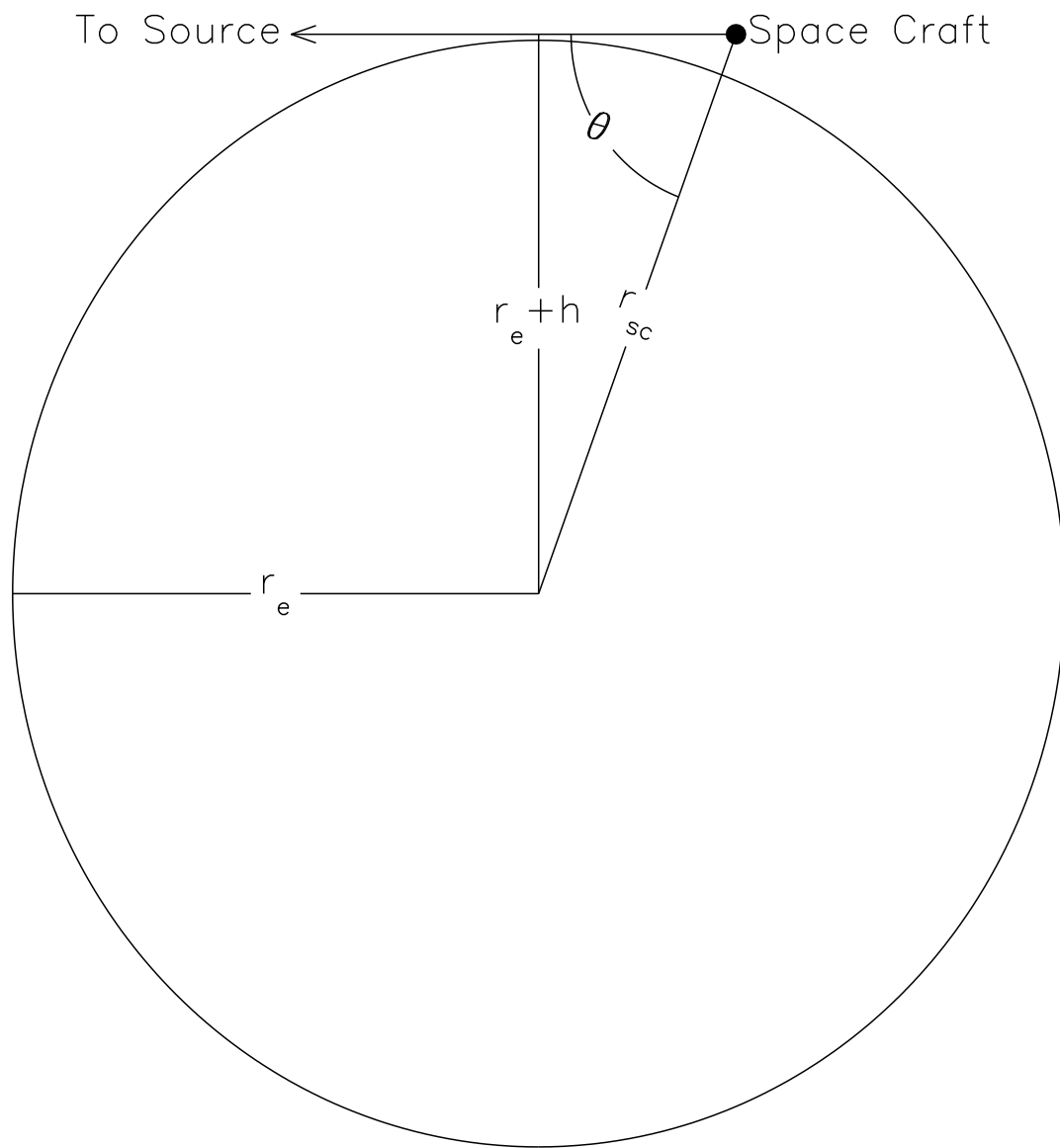


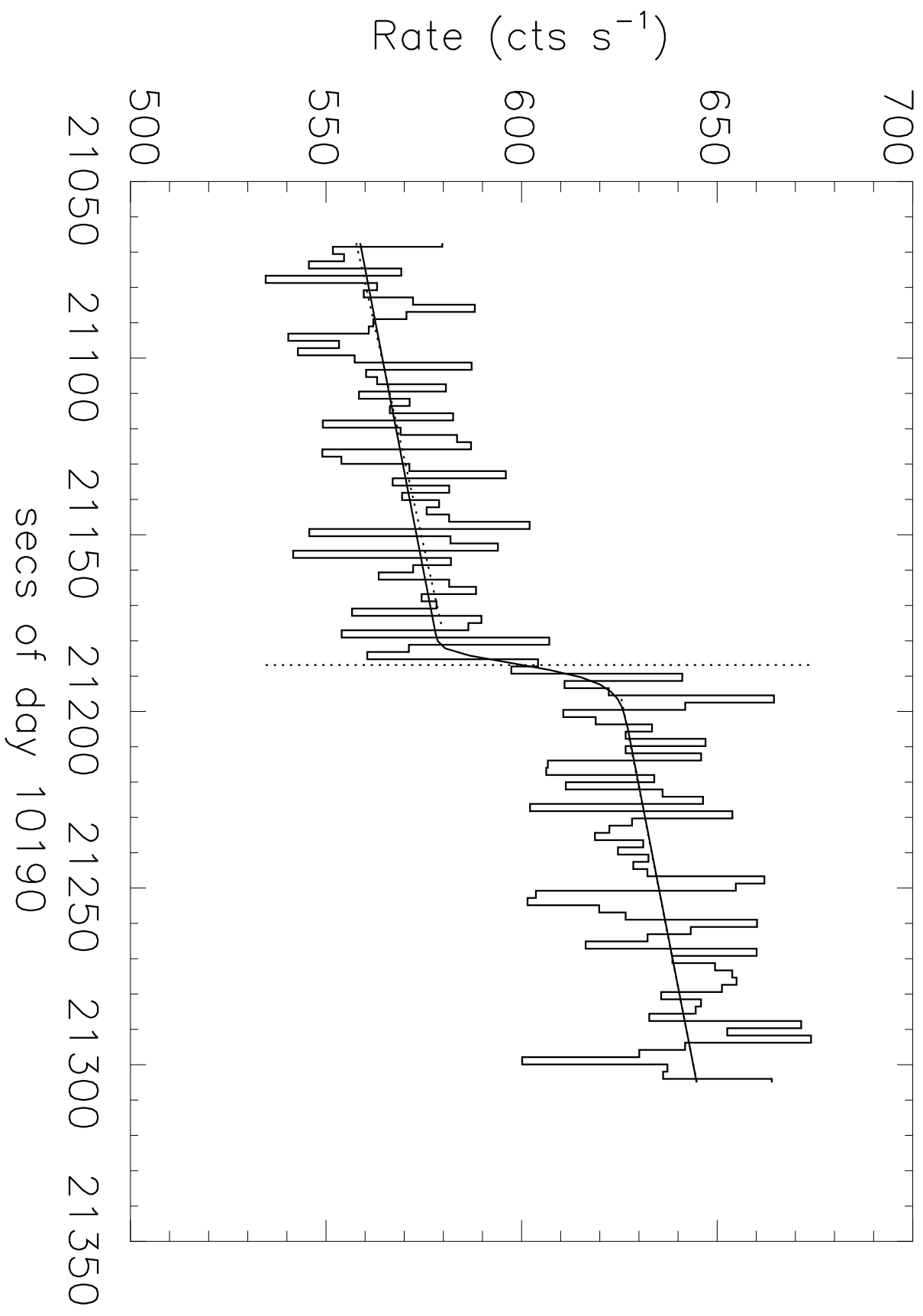


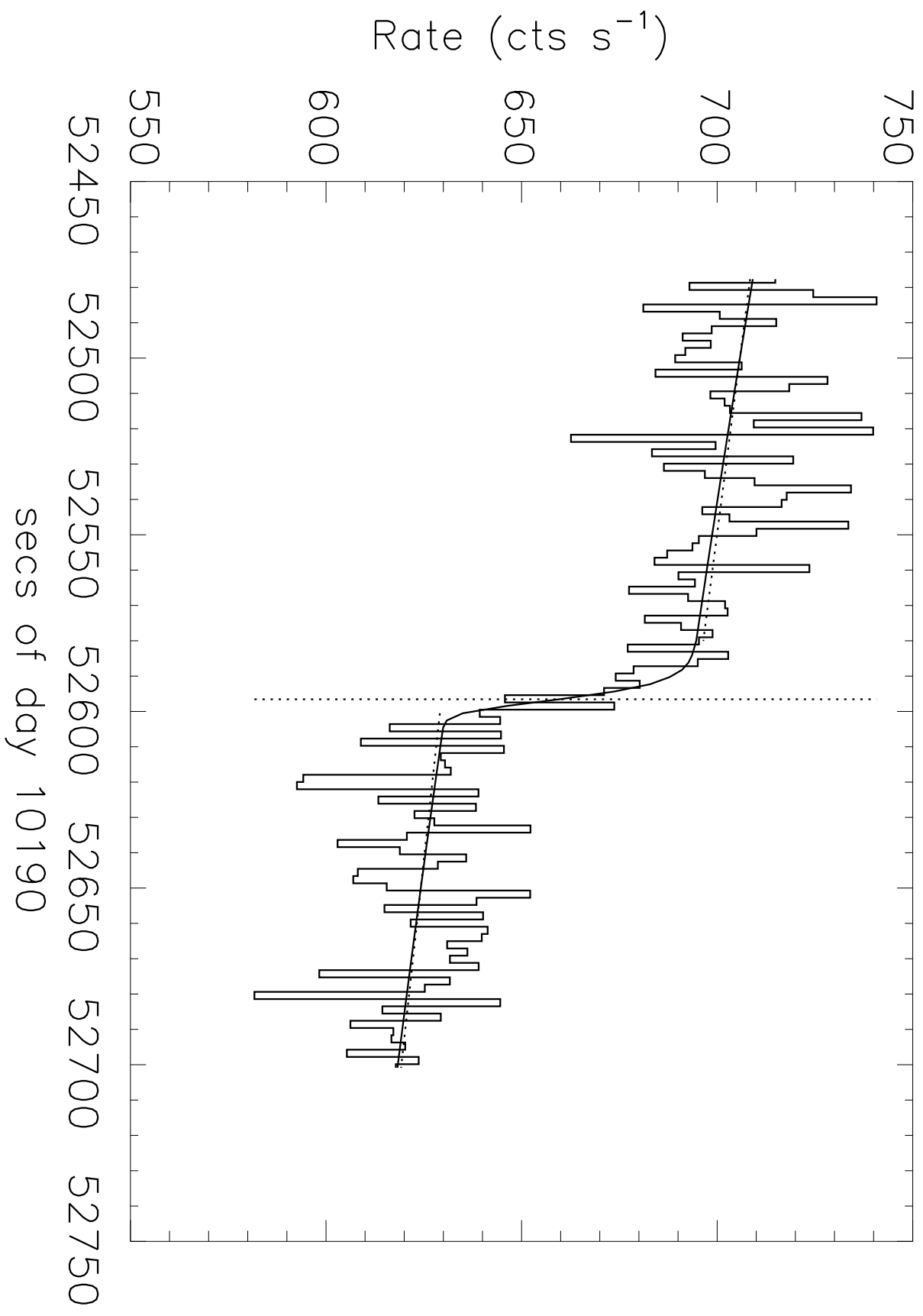




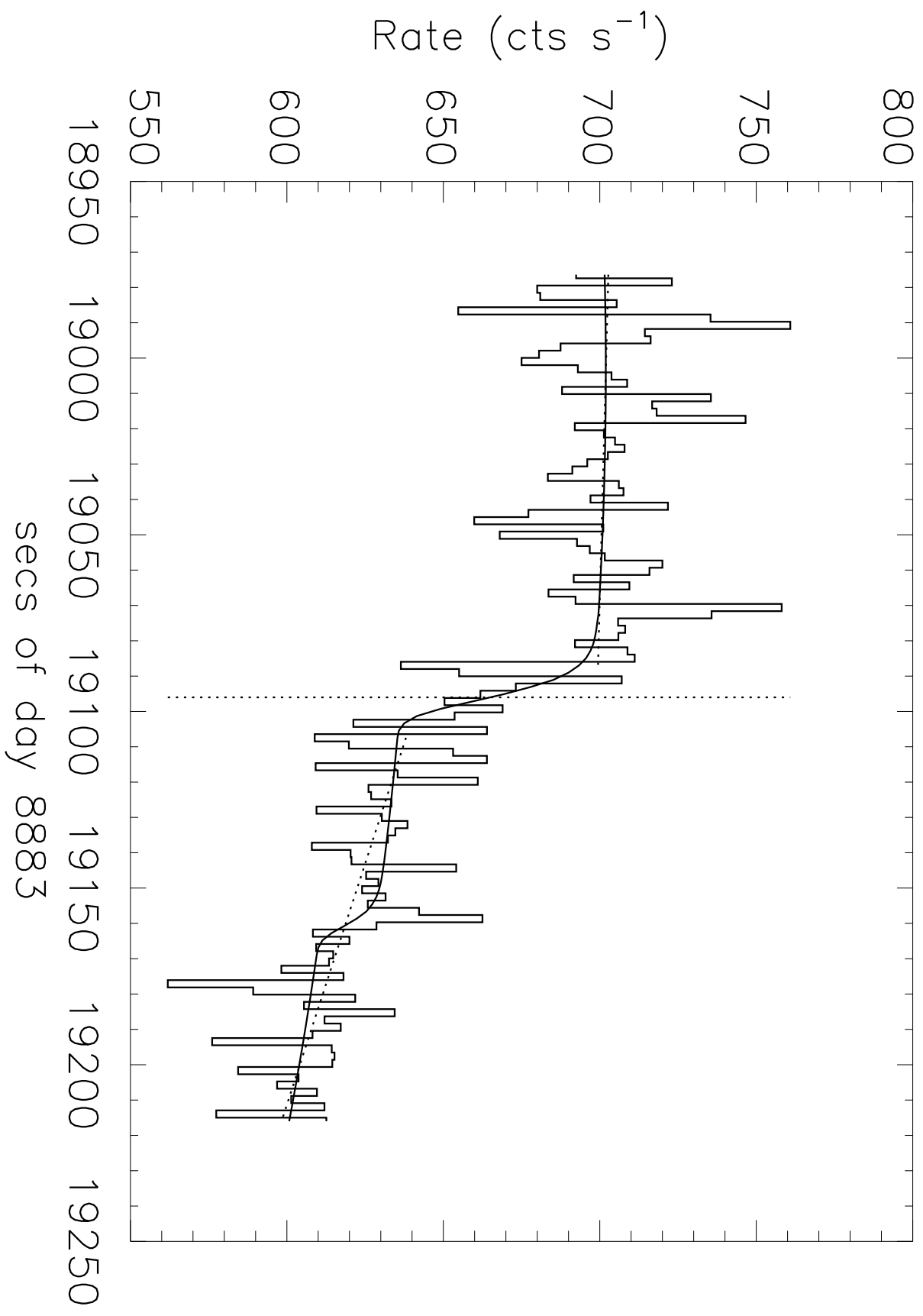


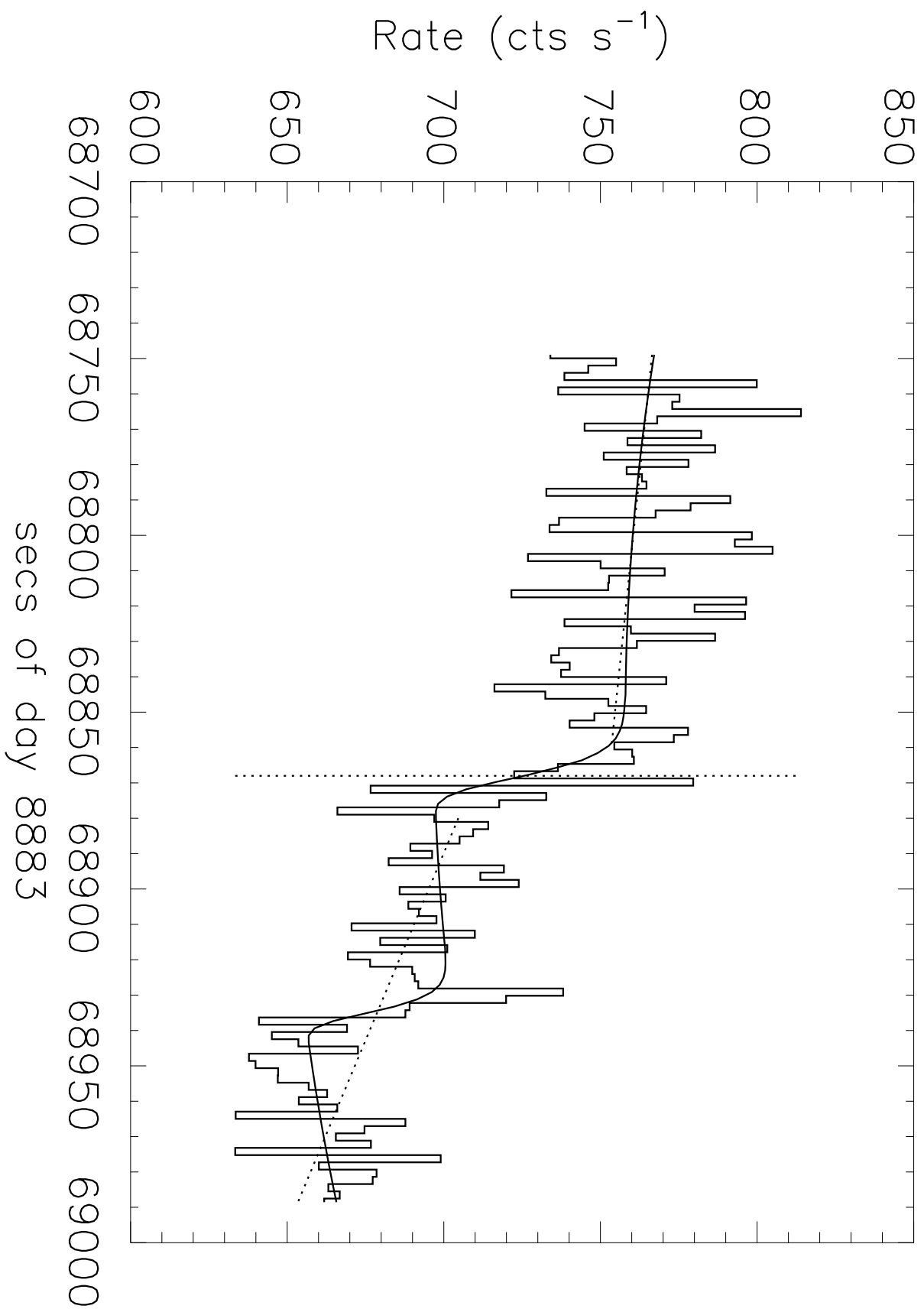


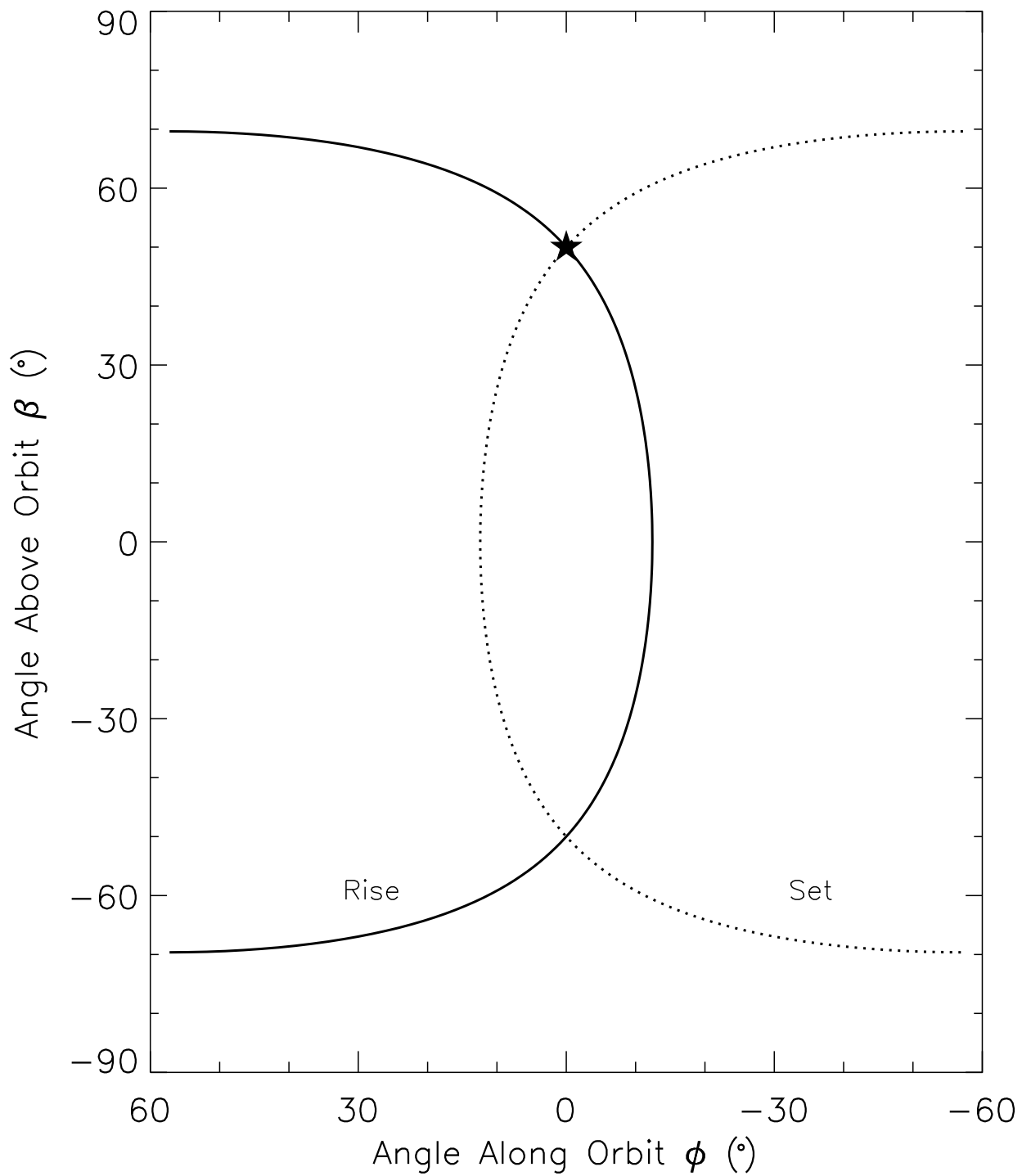


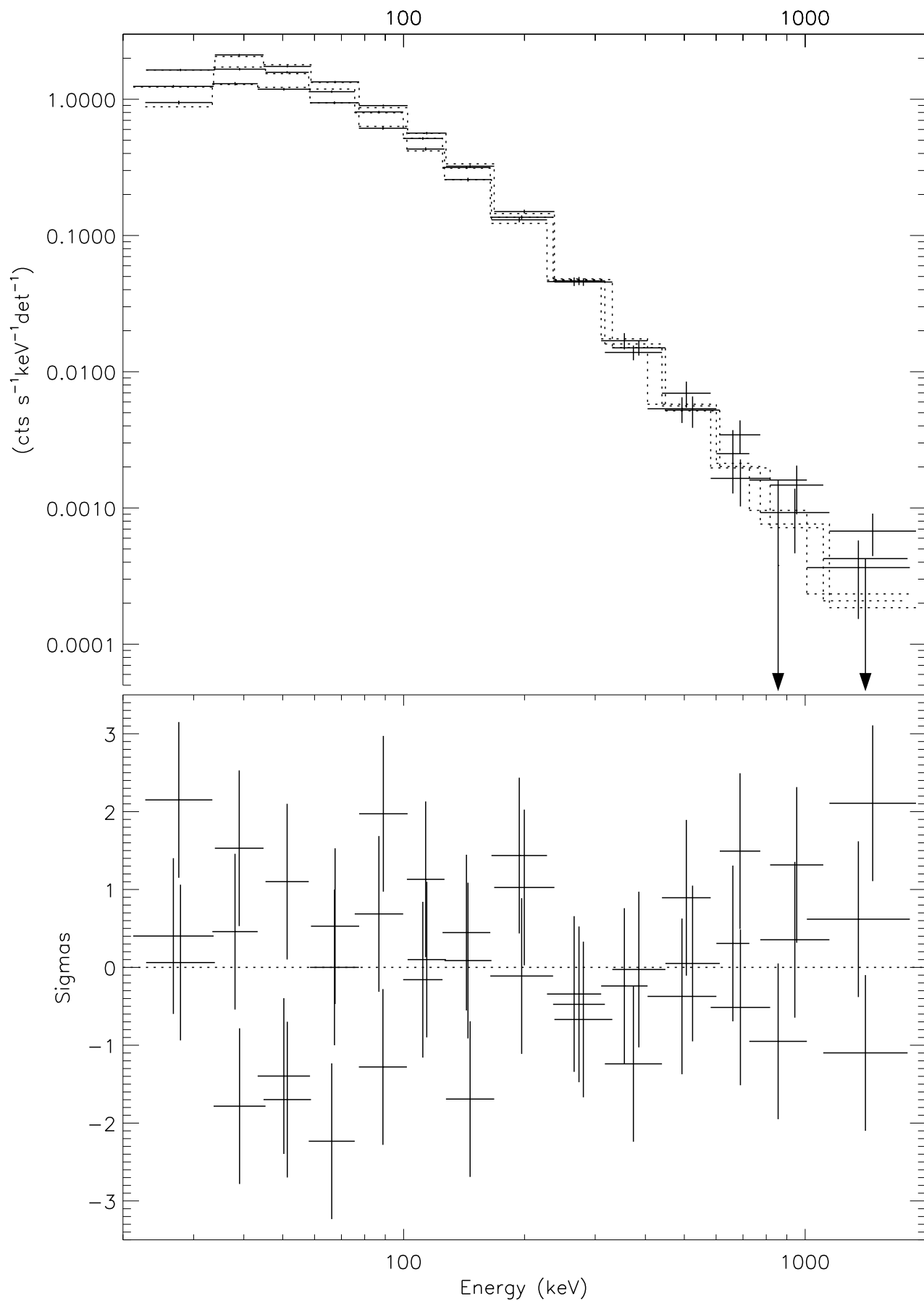


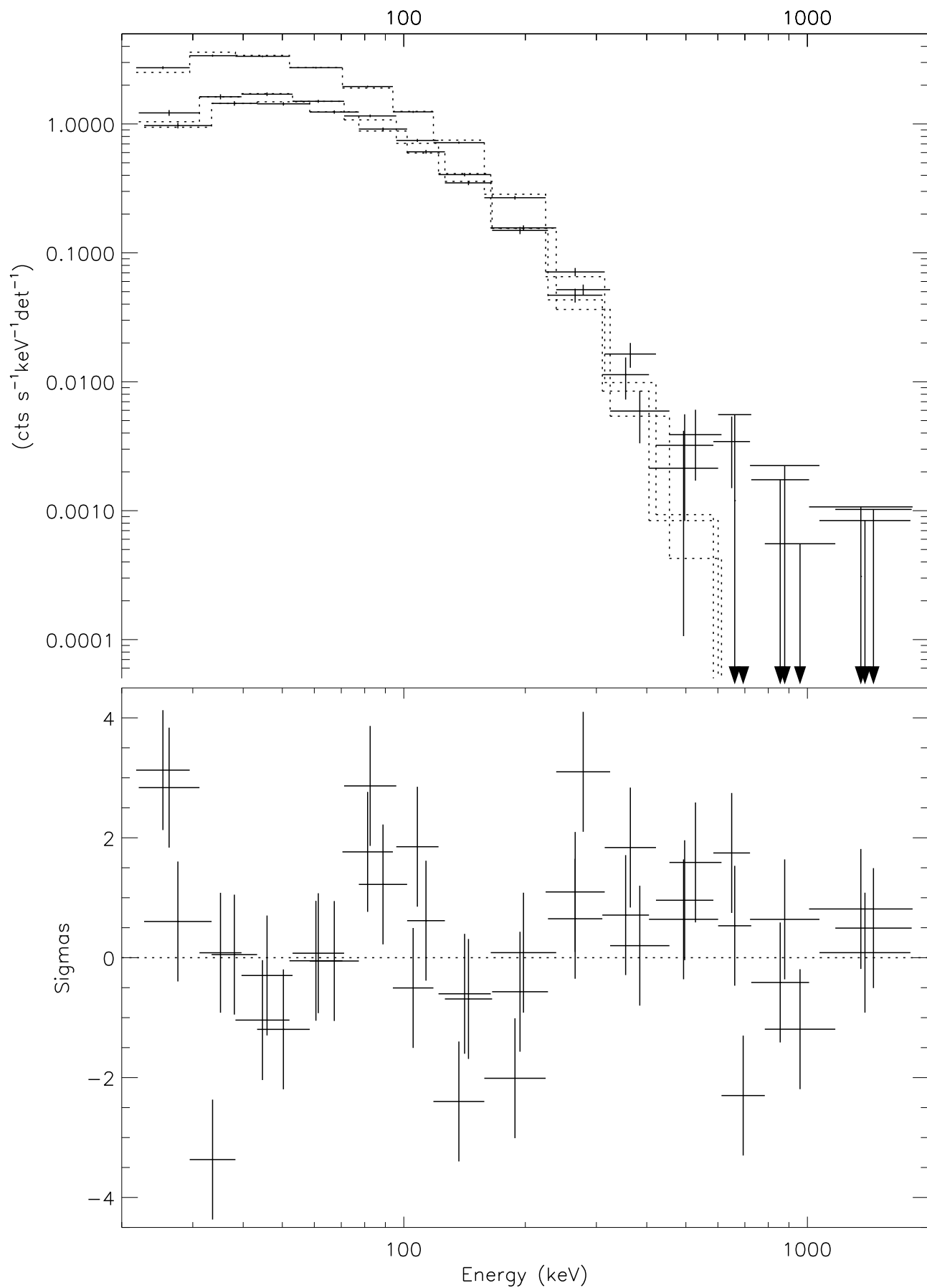


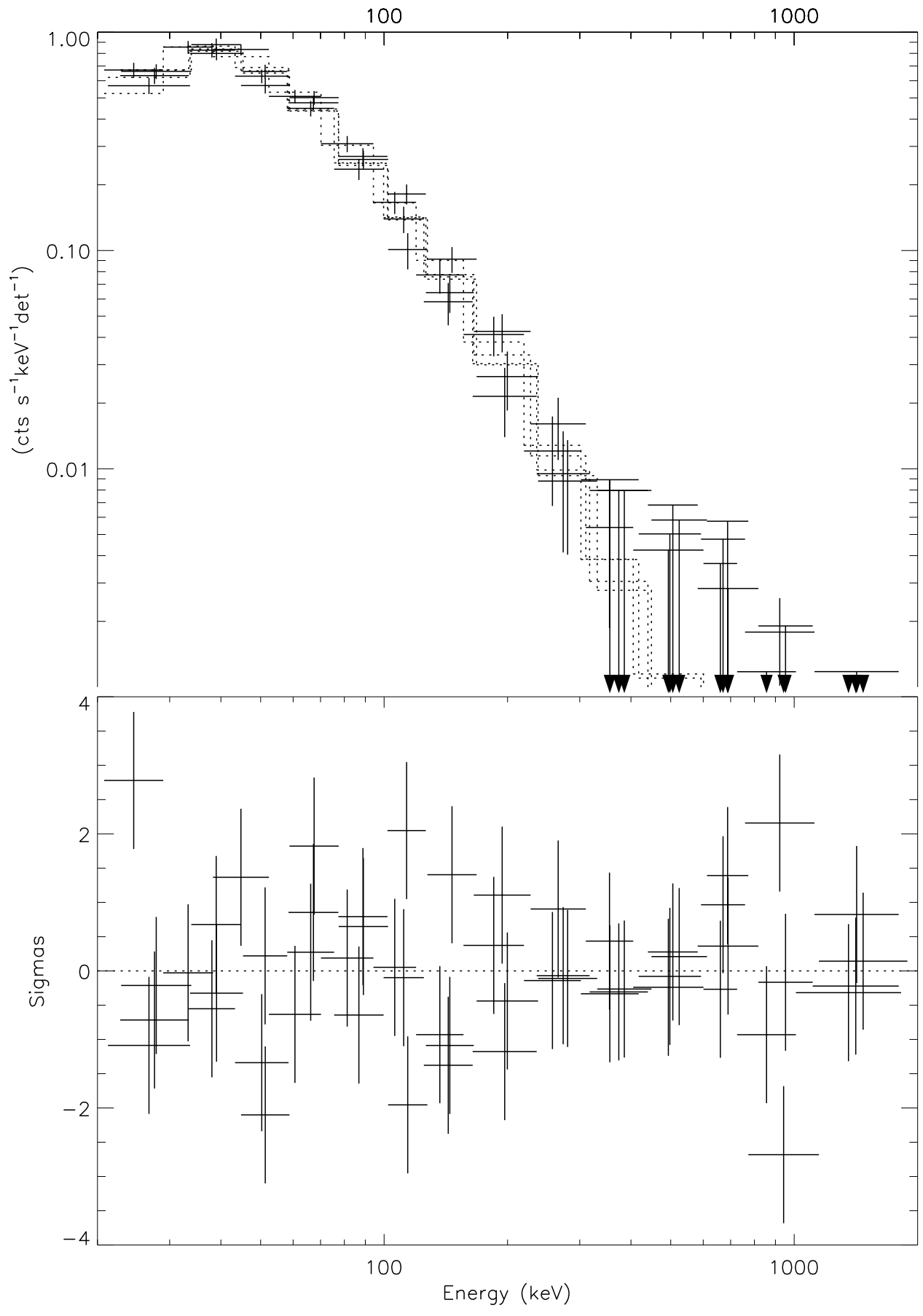


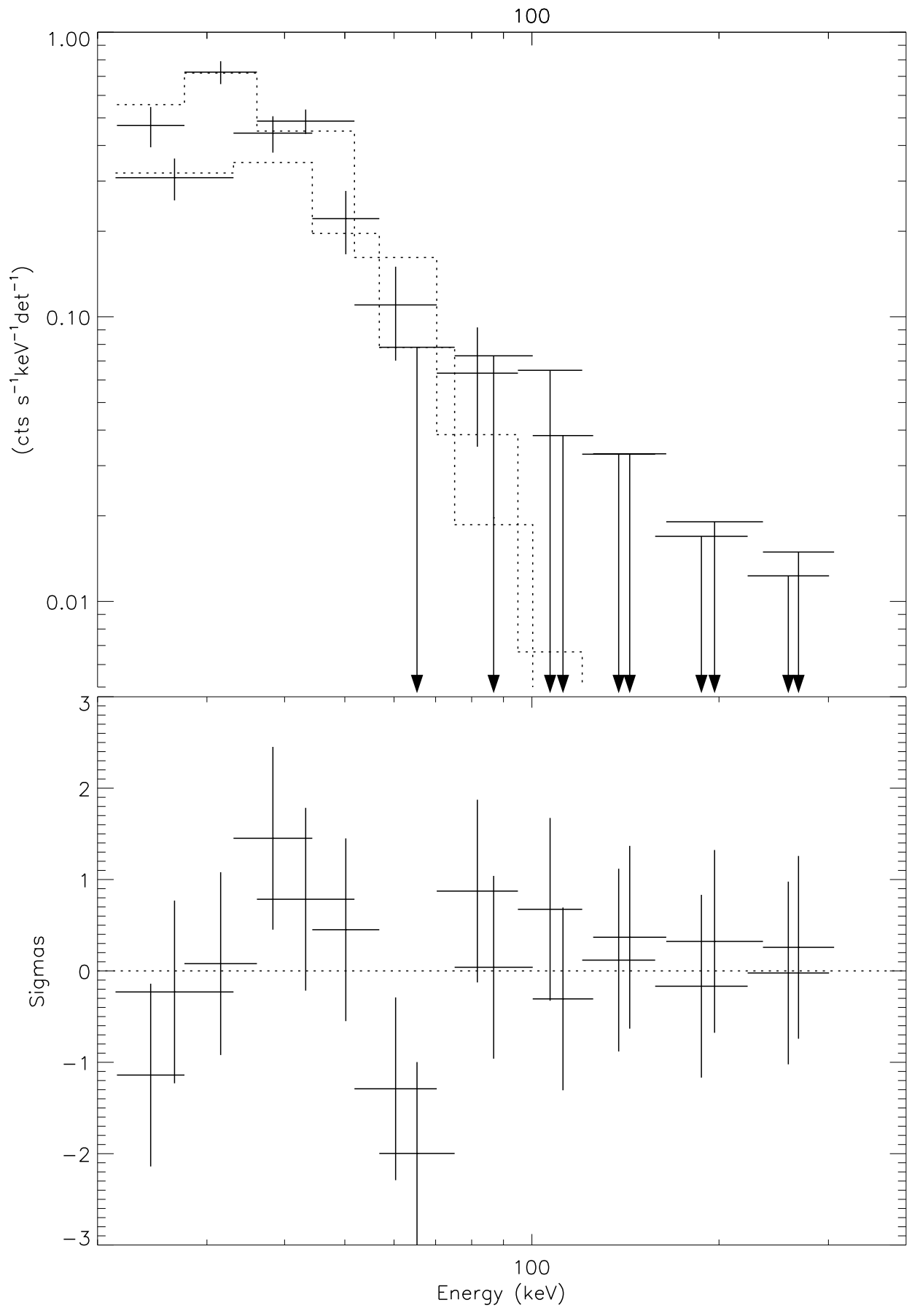




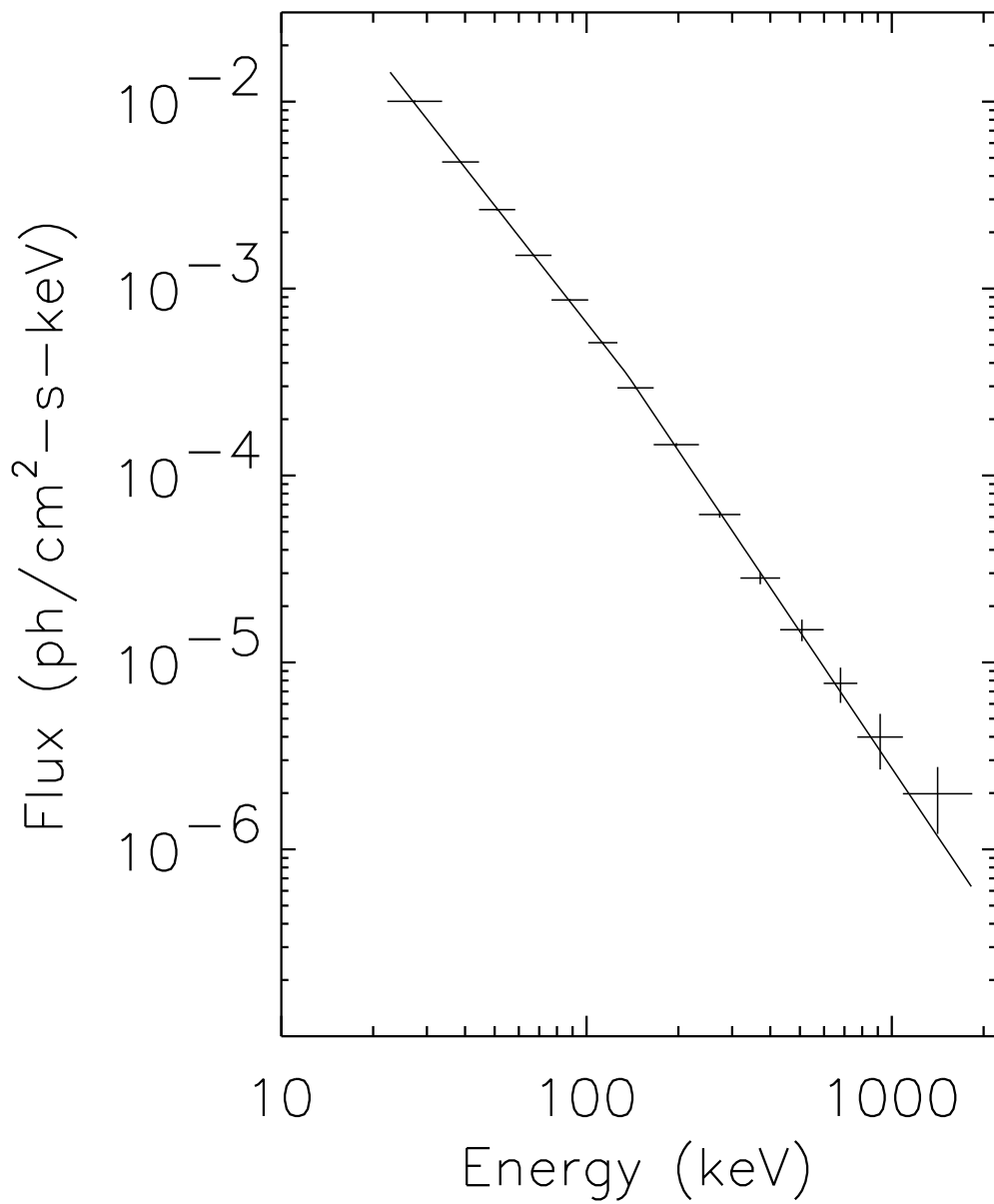






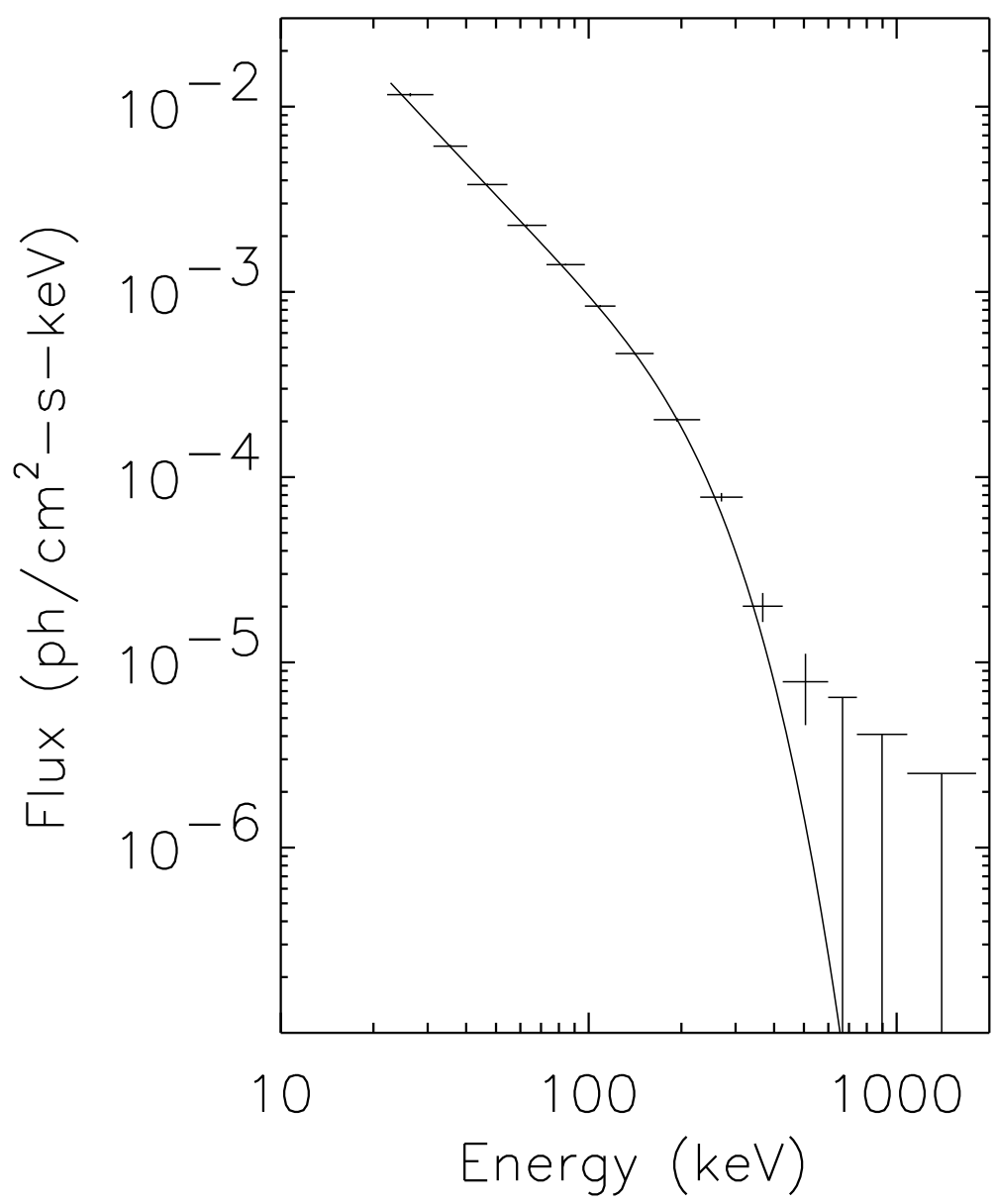


# CRAB NEBULA

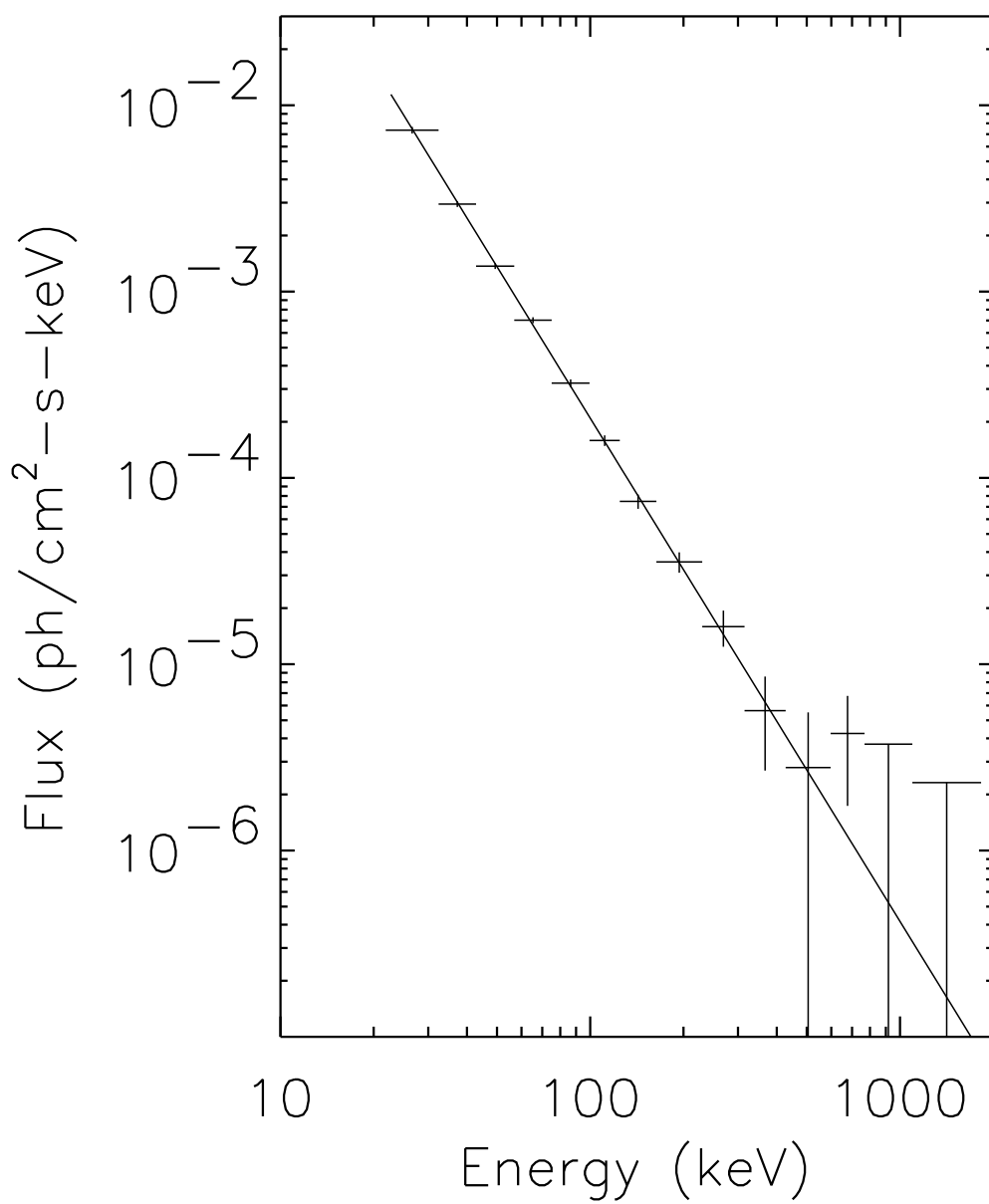




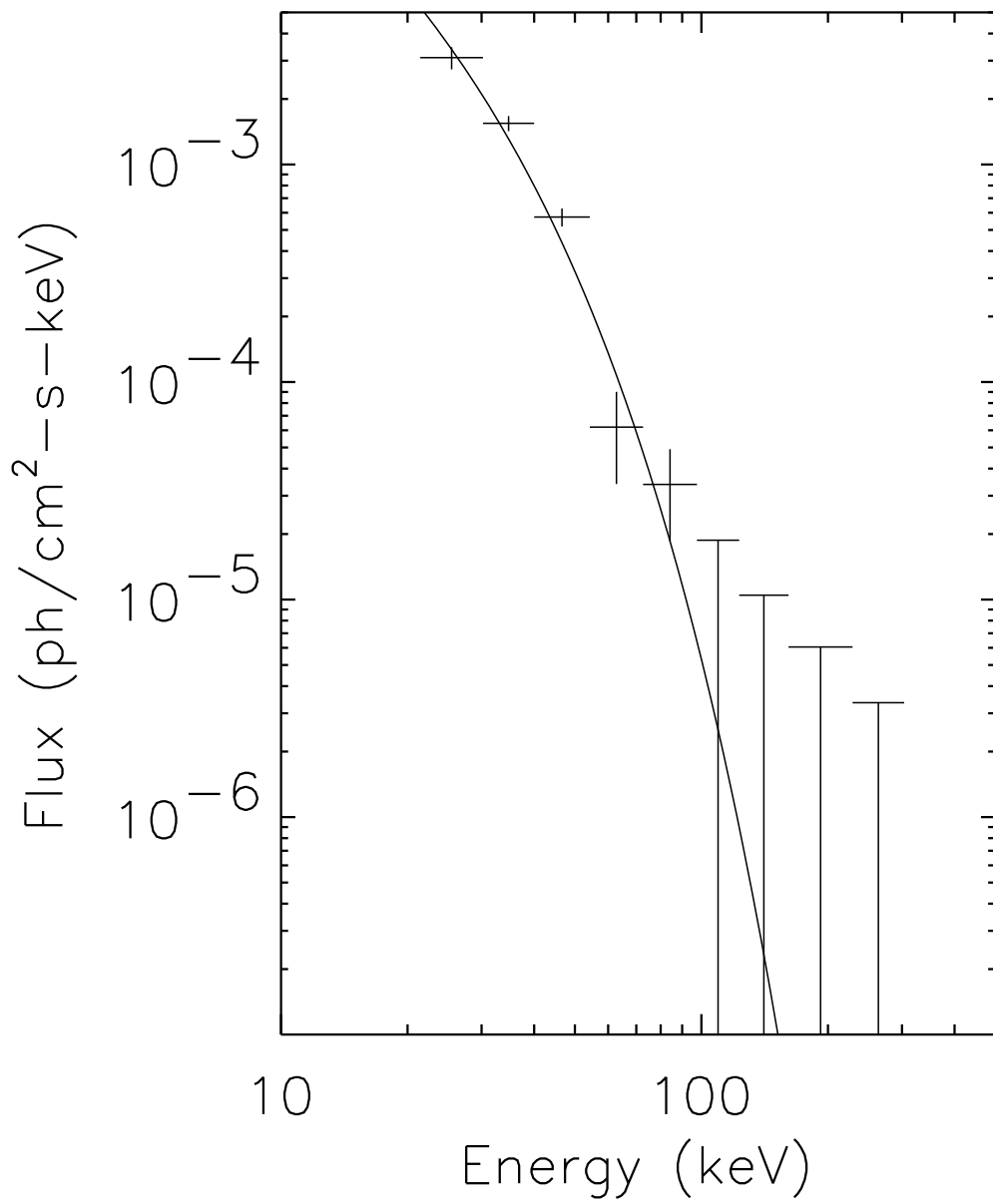
# CYGNUS X-1

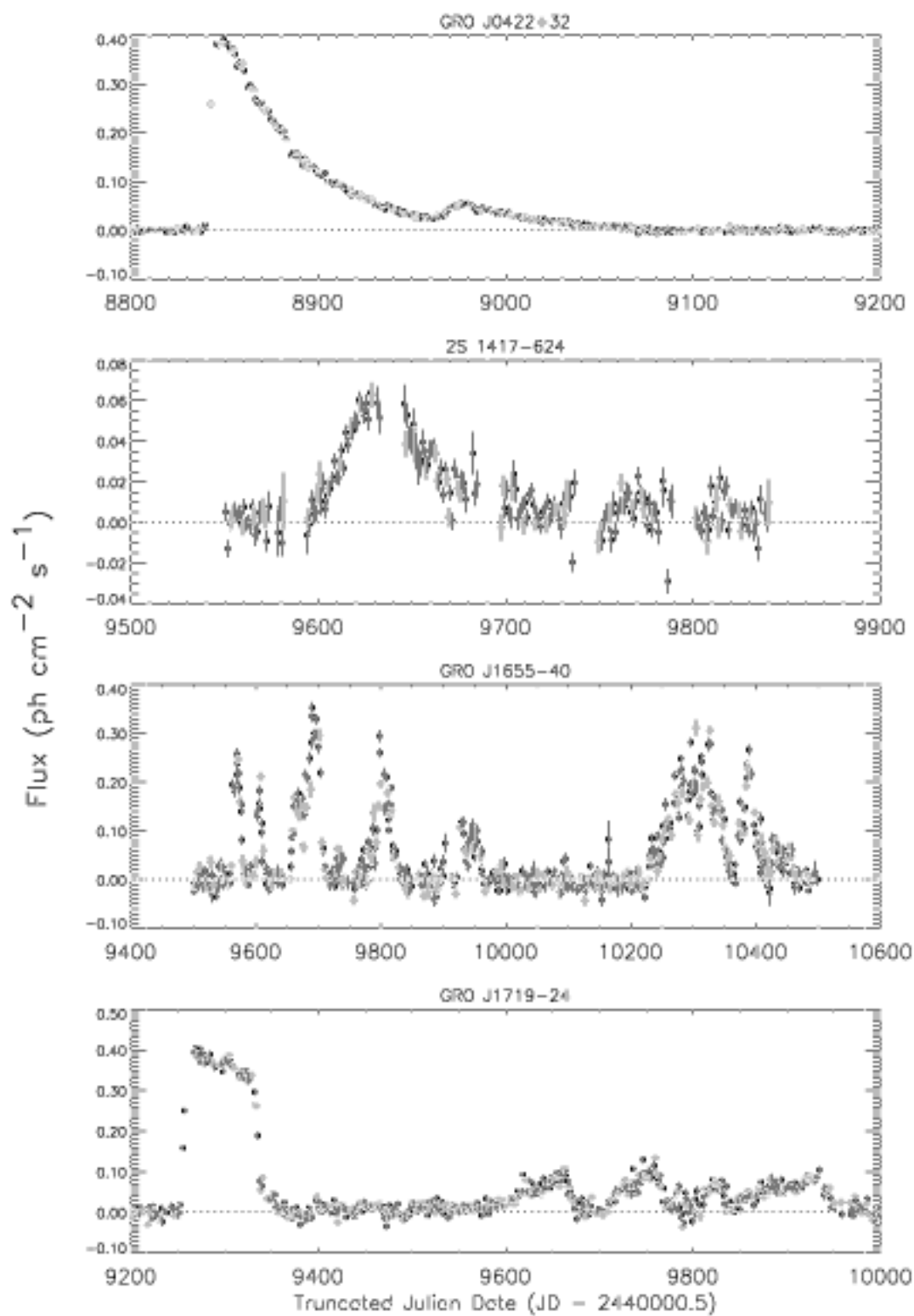


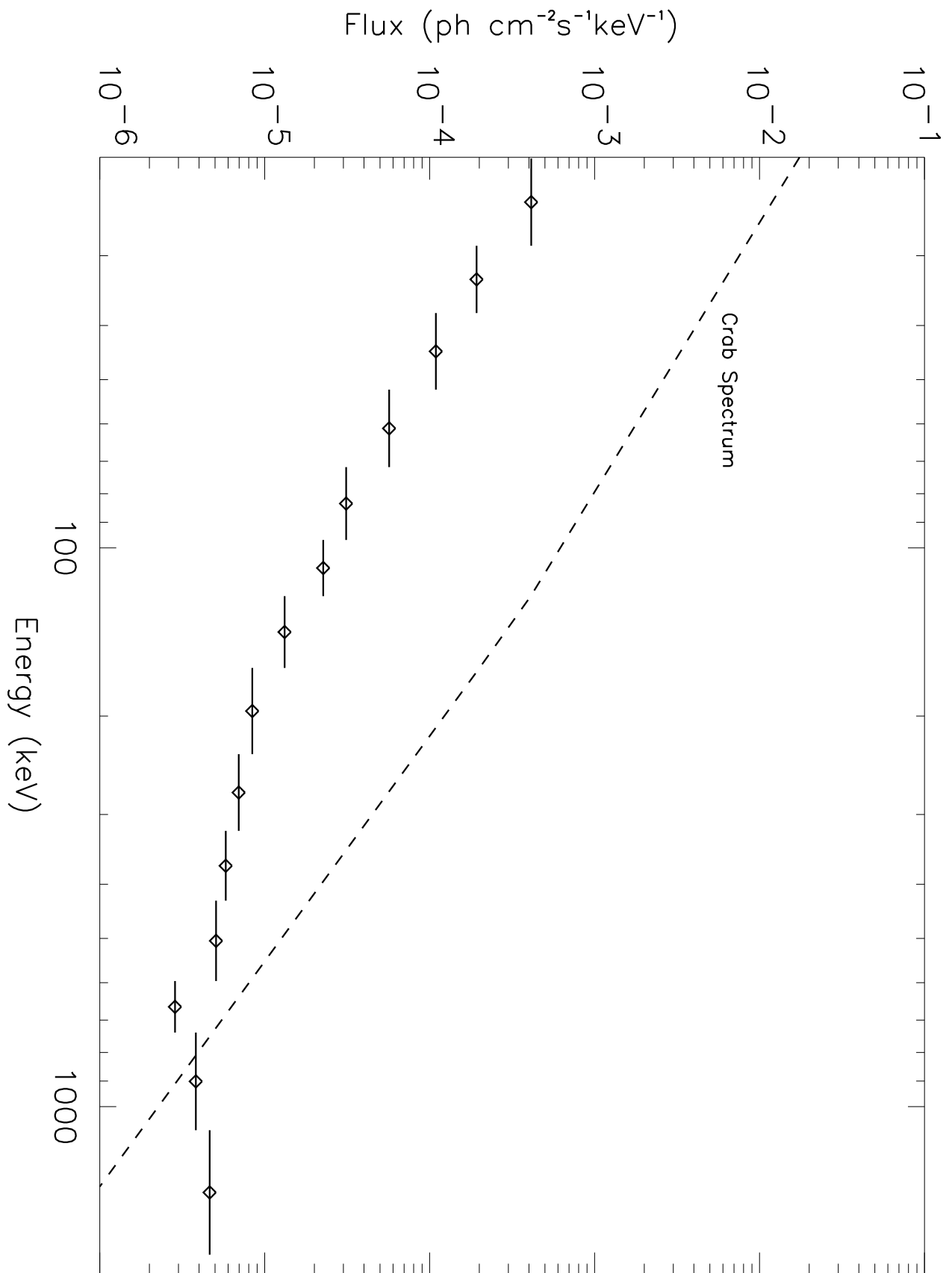
# GRO J1655-40



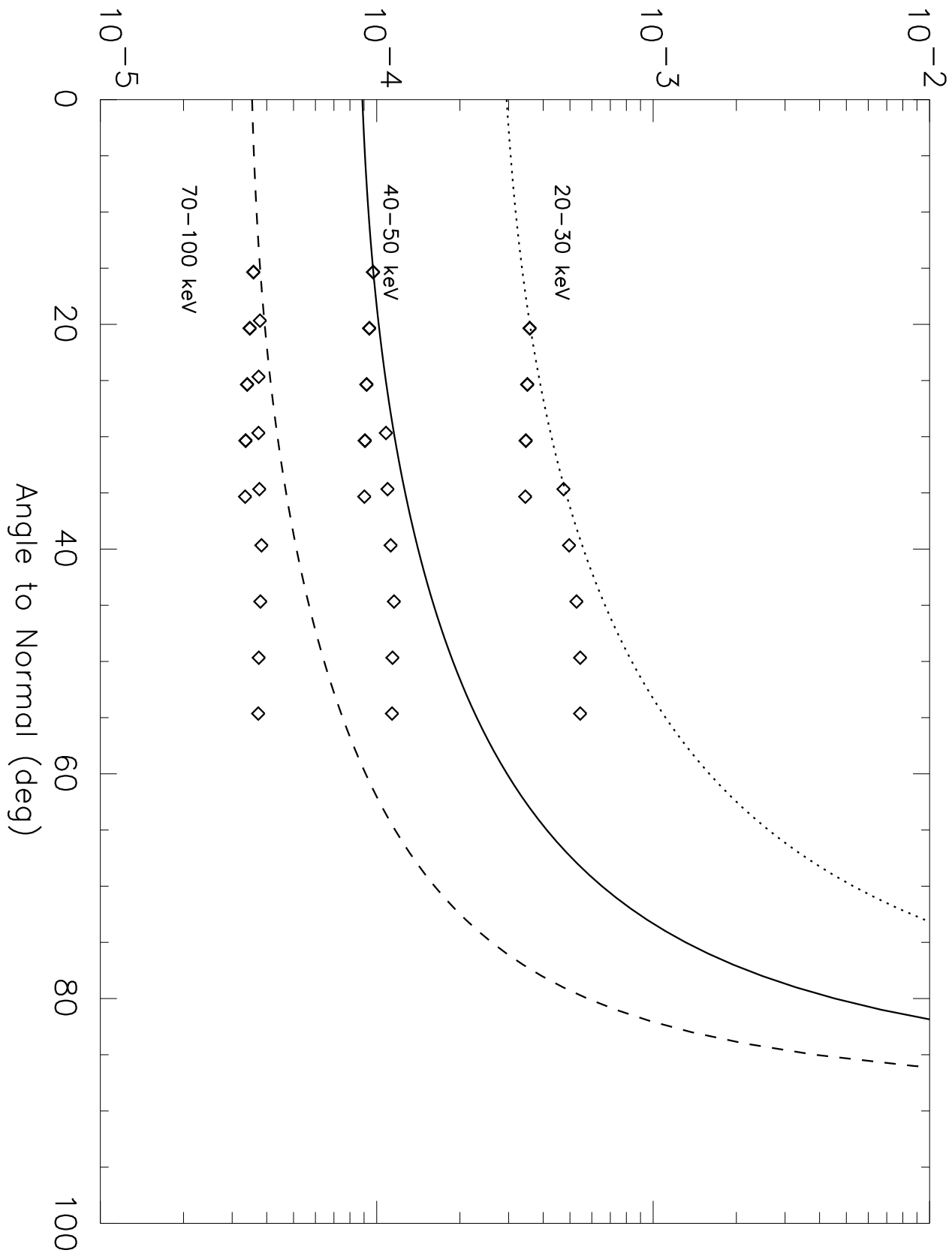
# VELA X-1

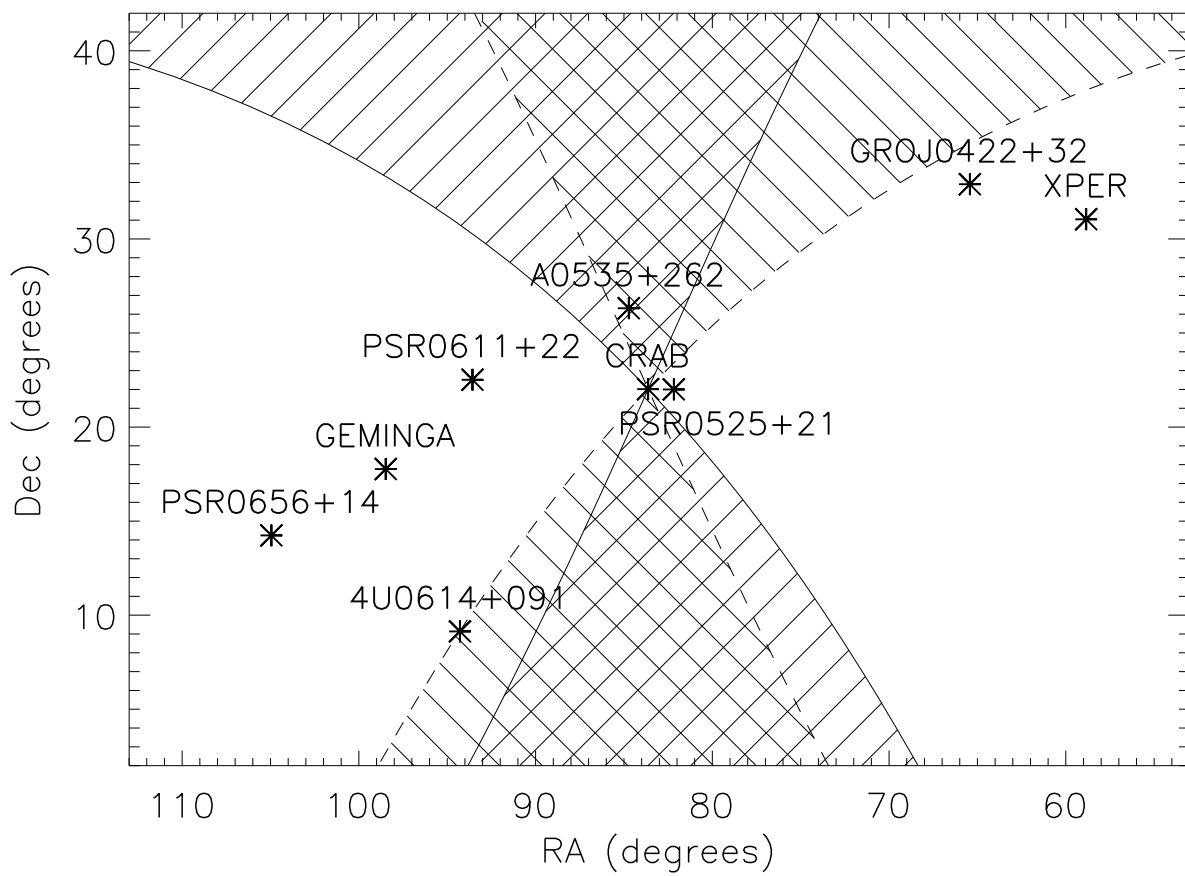


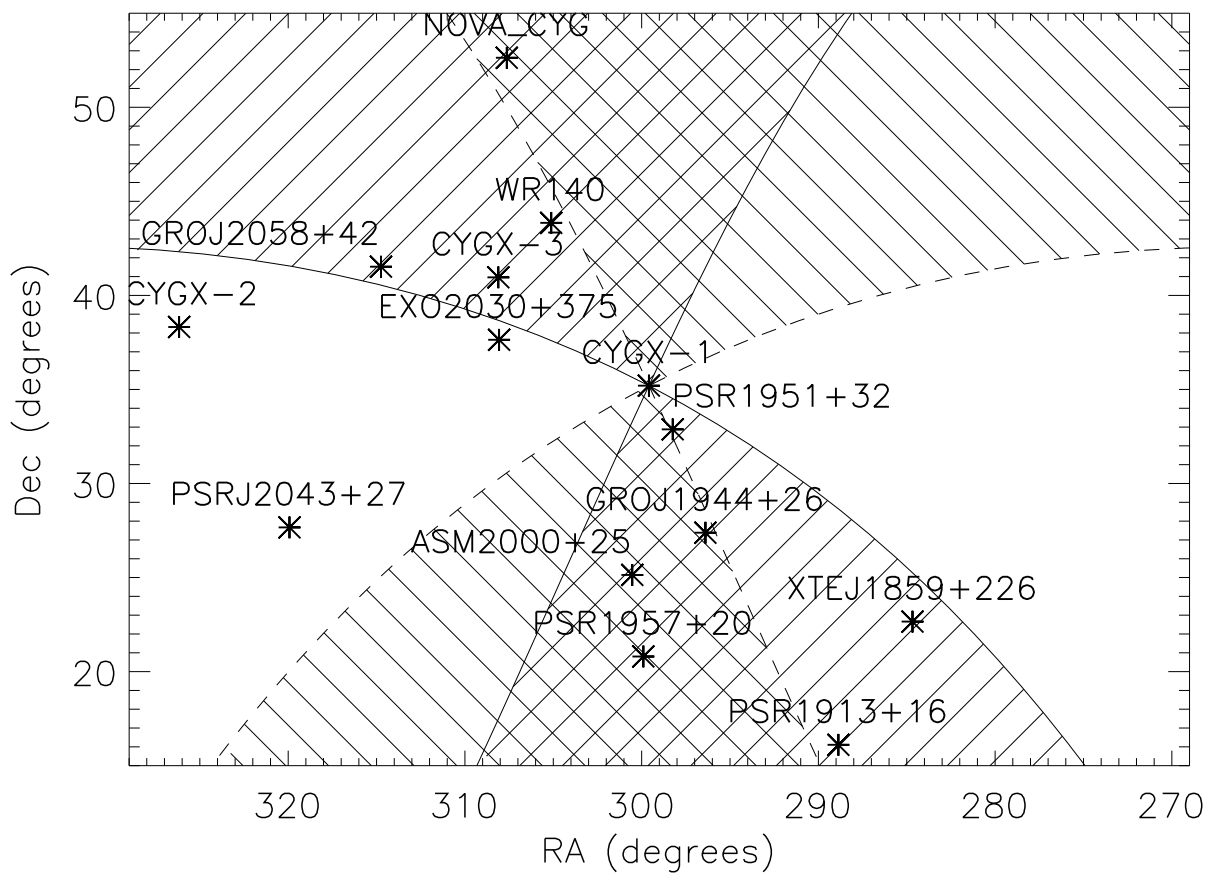




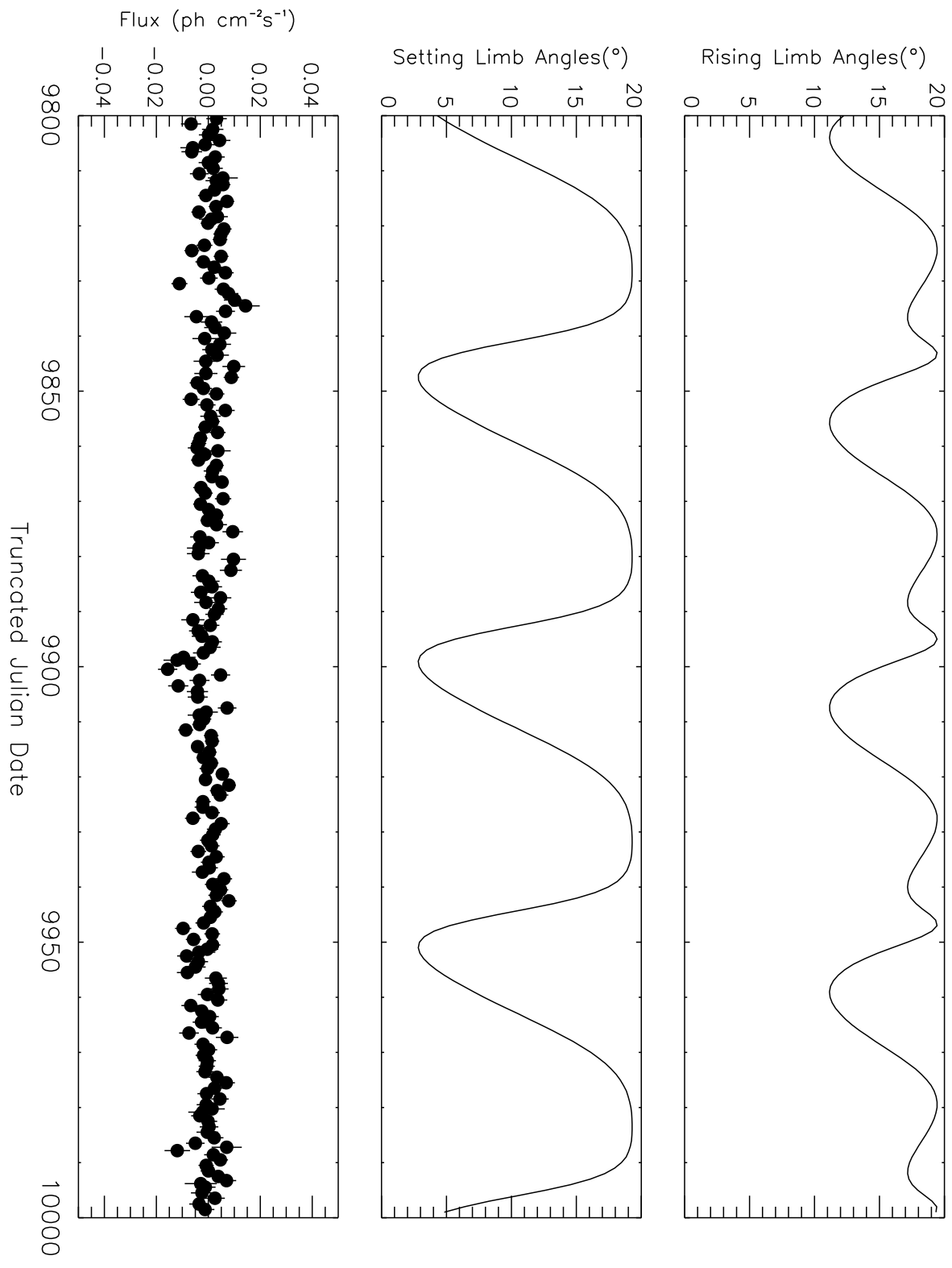
3-Sig Sensitivity ( $\text{ph cm}^{-2}\text{s}^{-1}\text{keV}^{-1}$ )

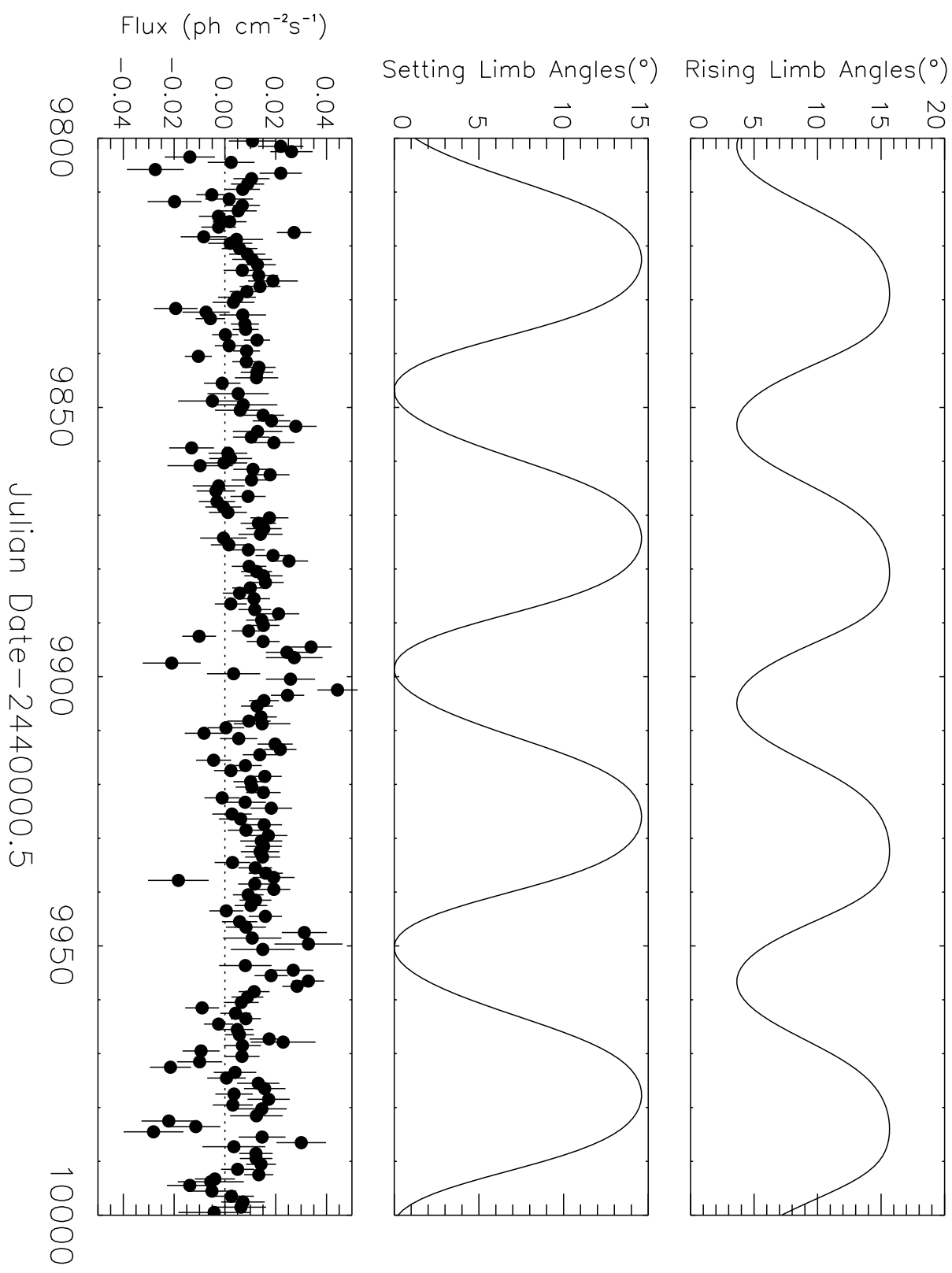


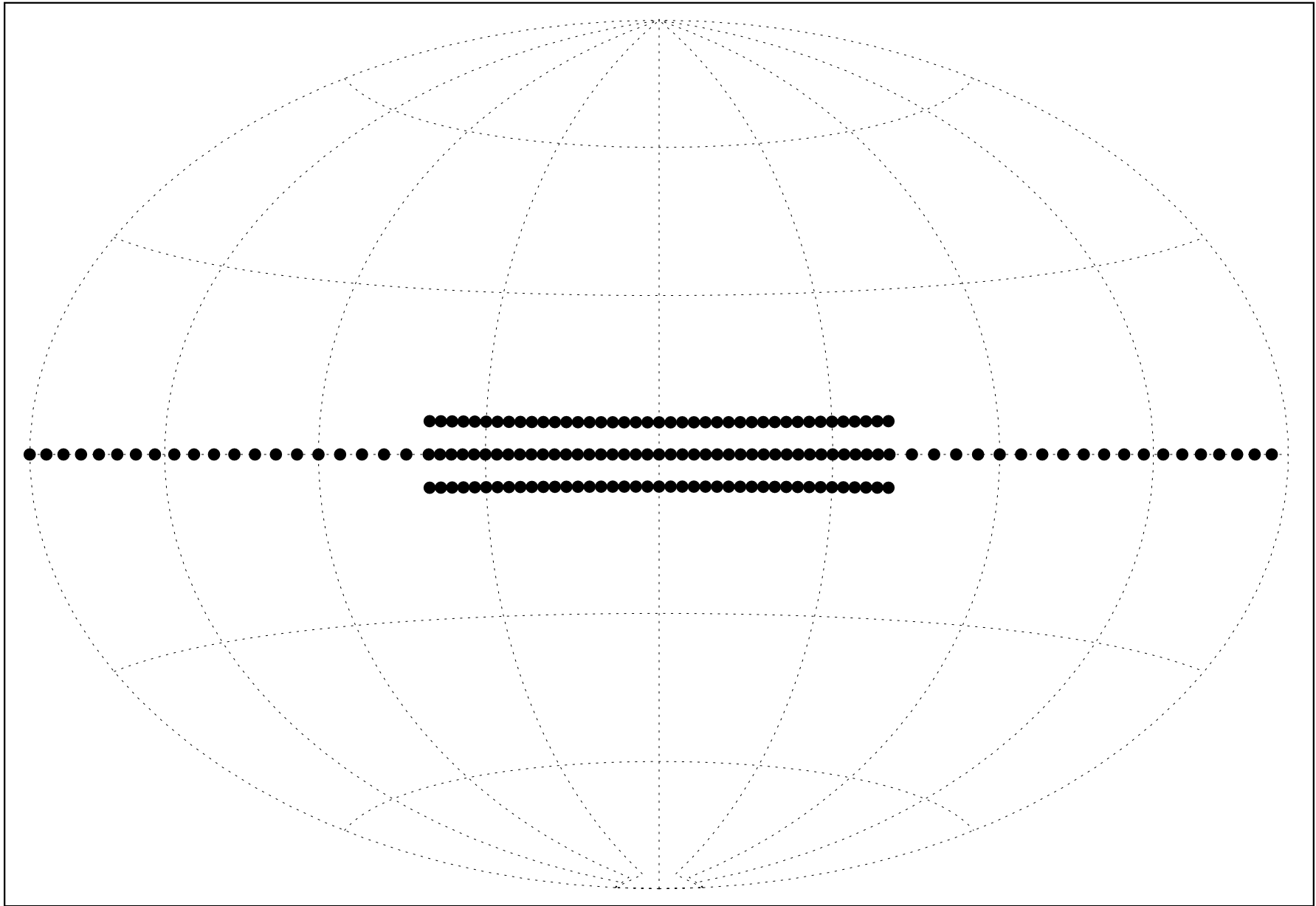


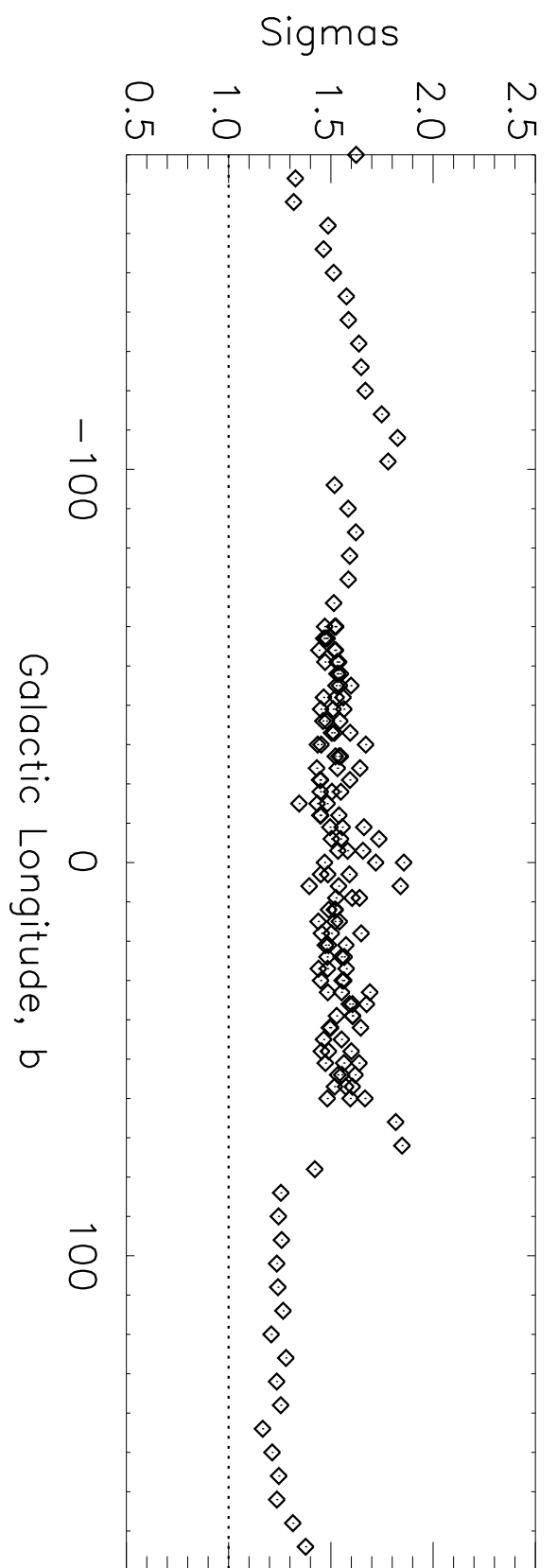
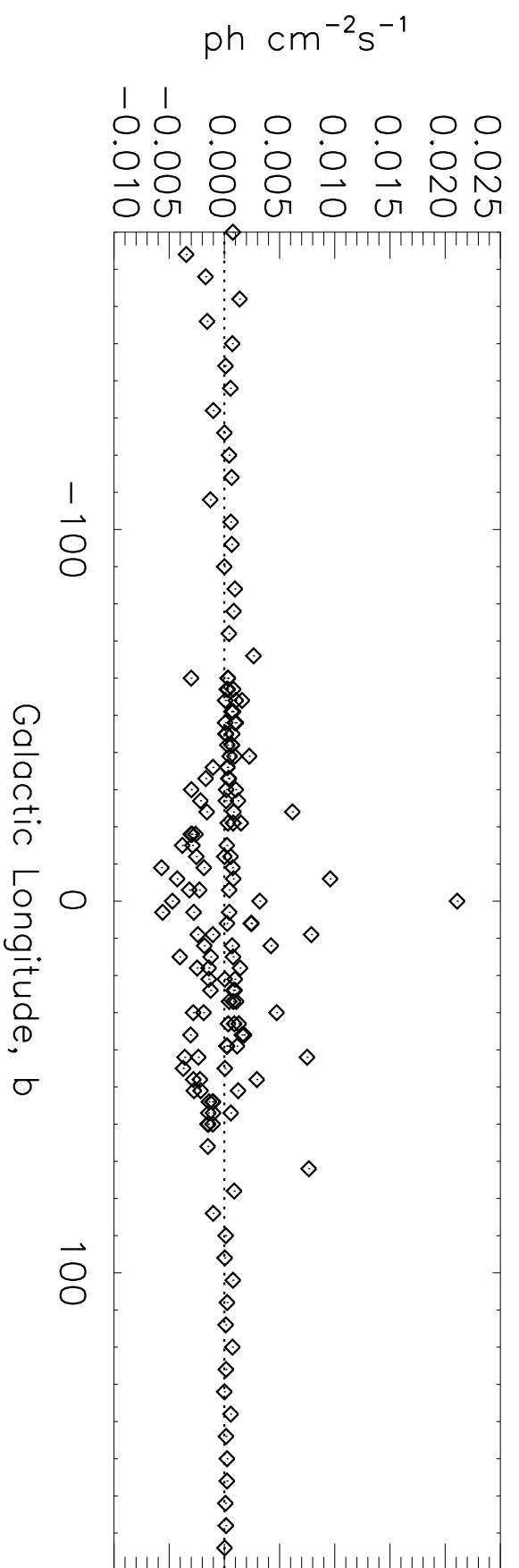


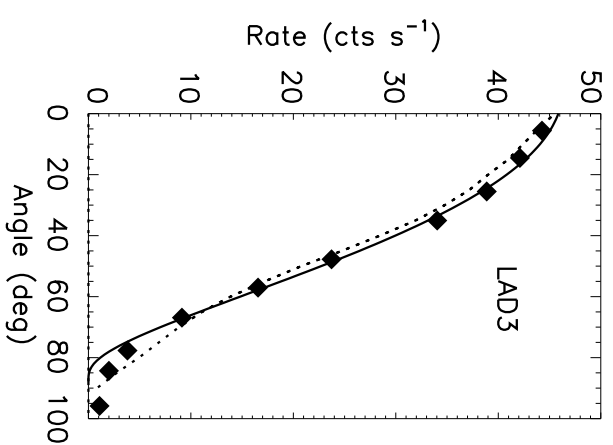
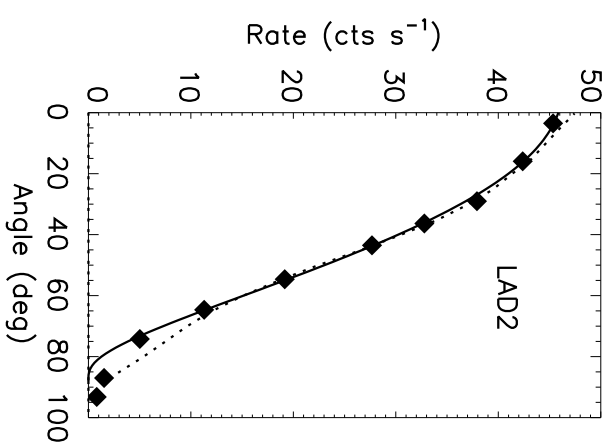
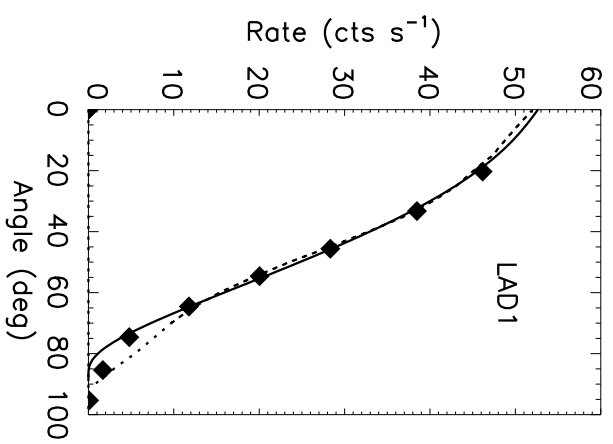
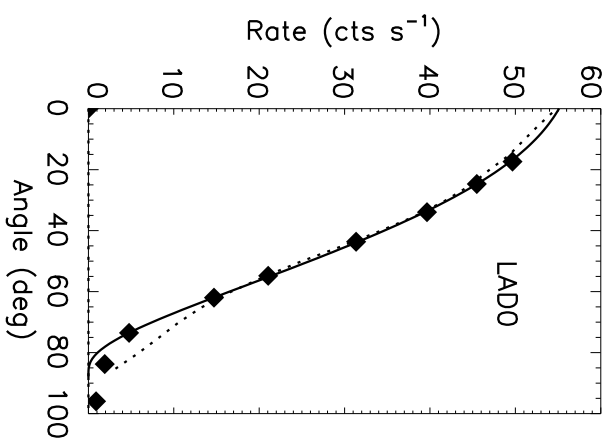
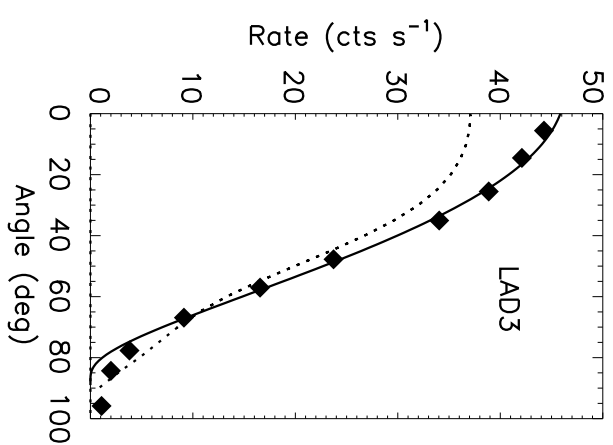
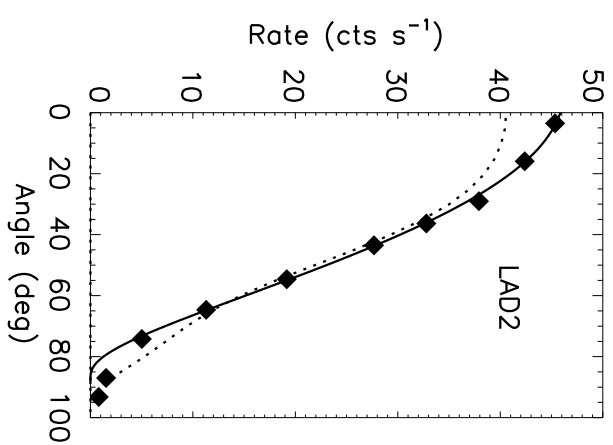
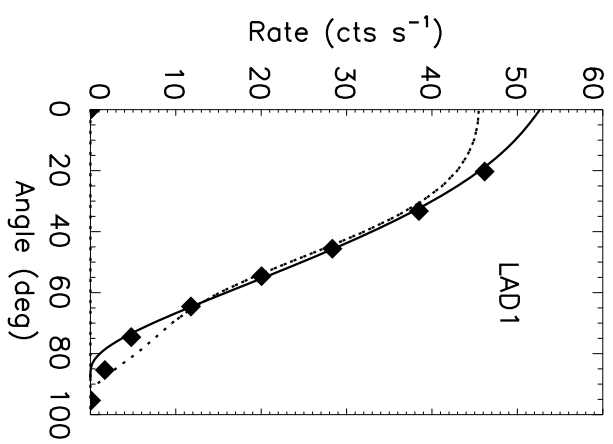
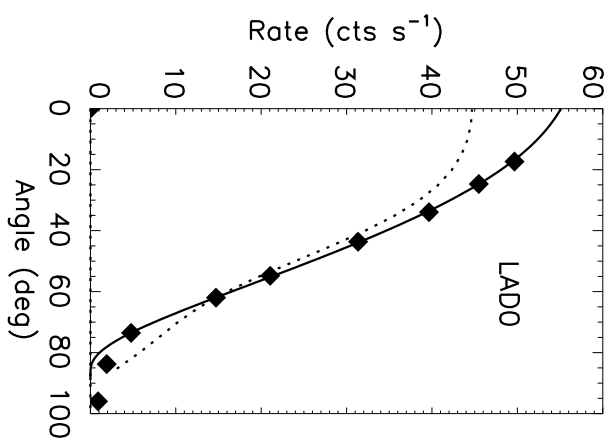


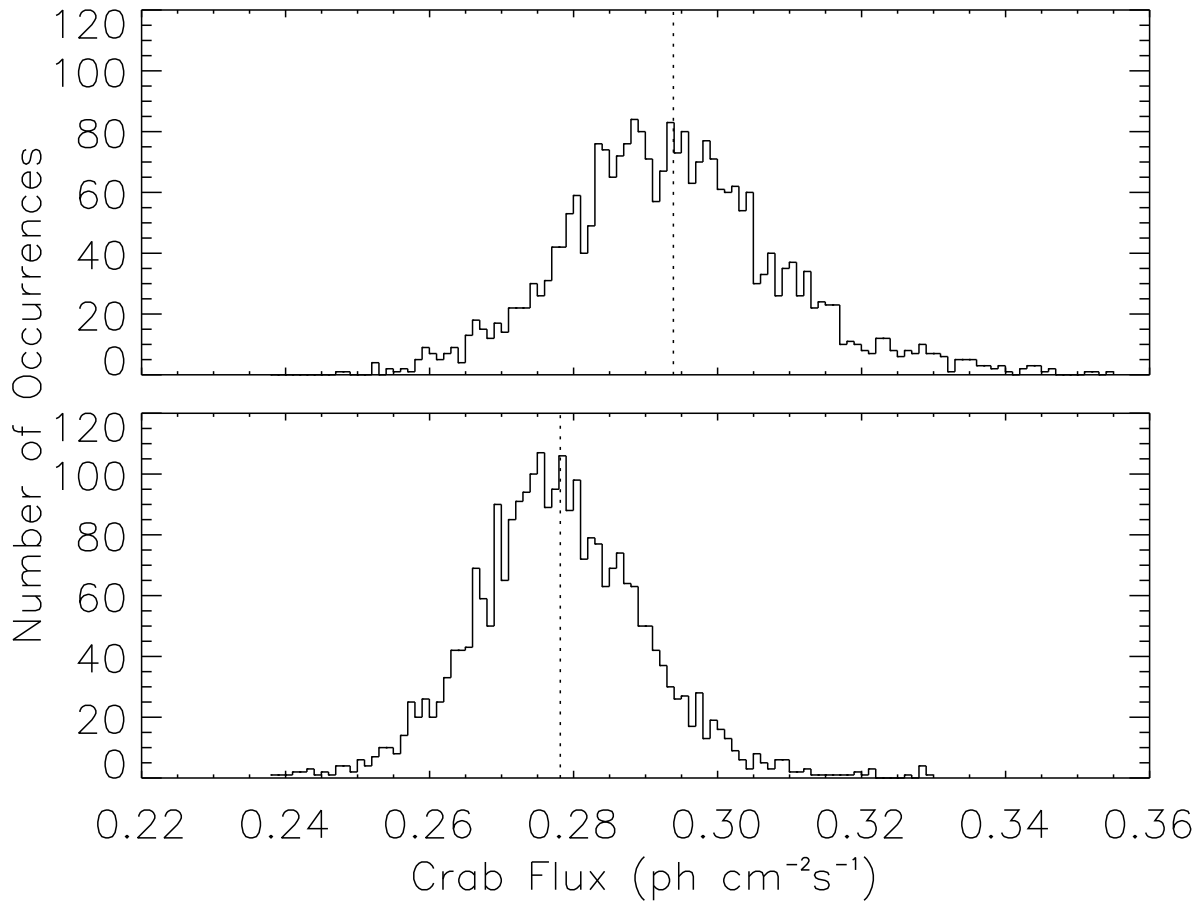


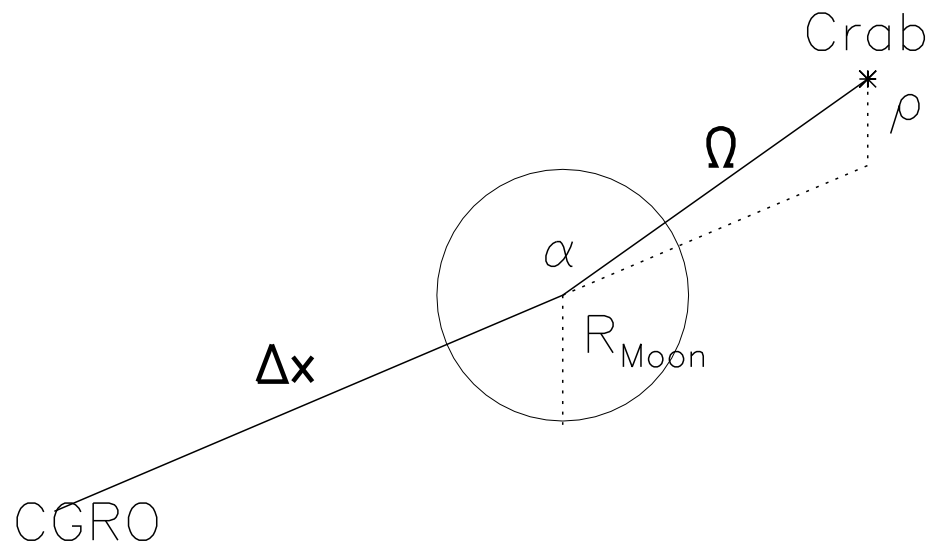


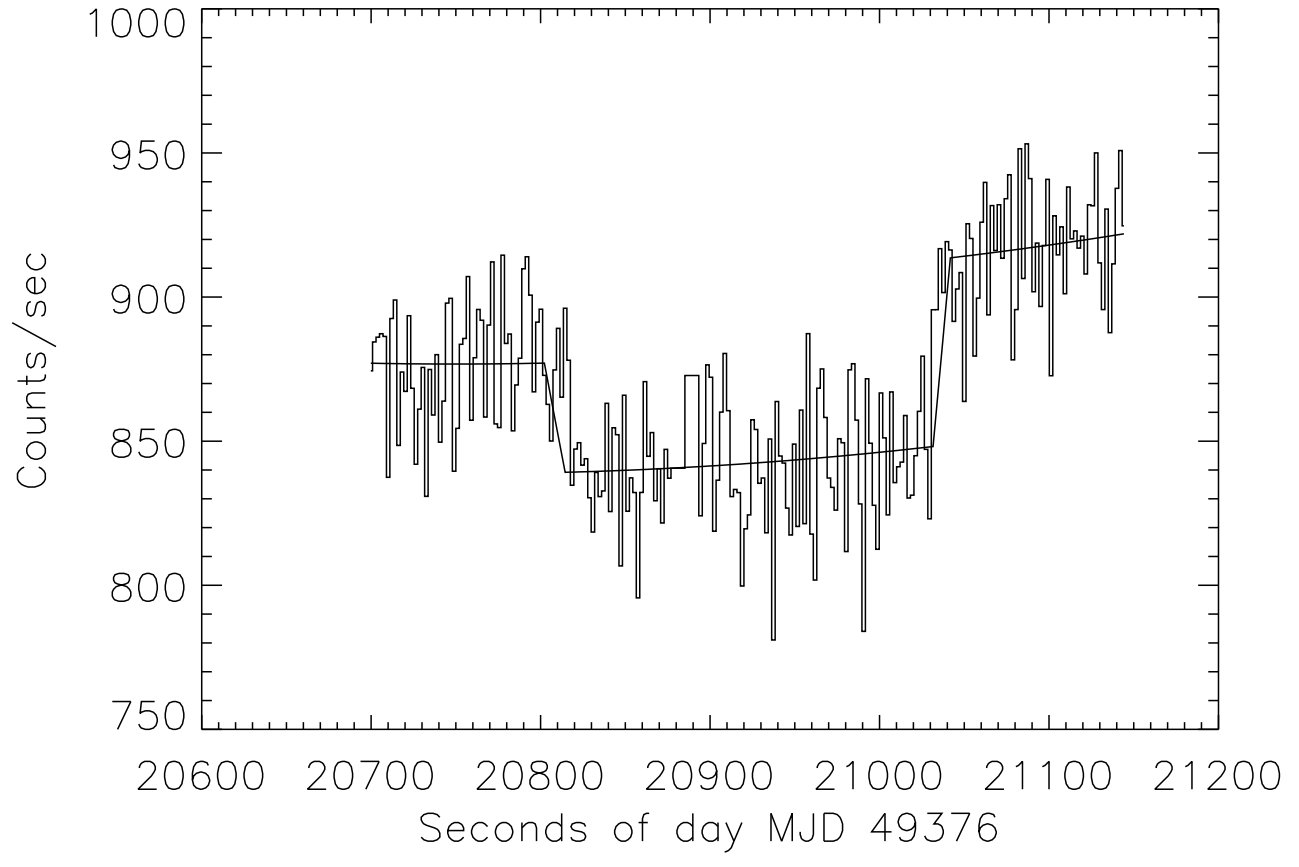




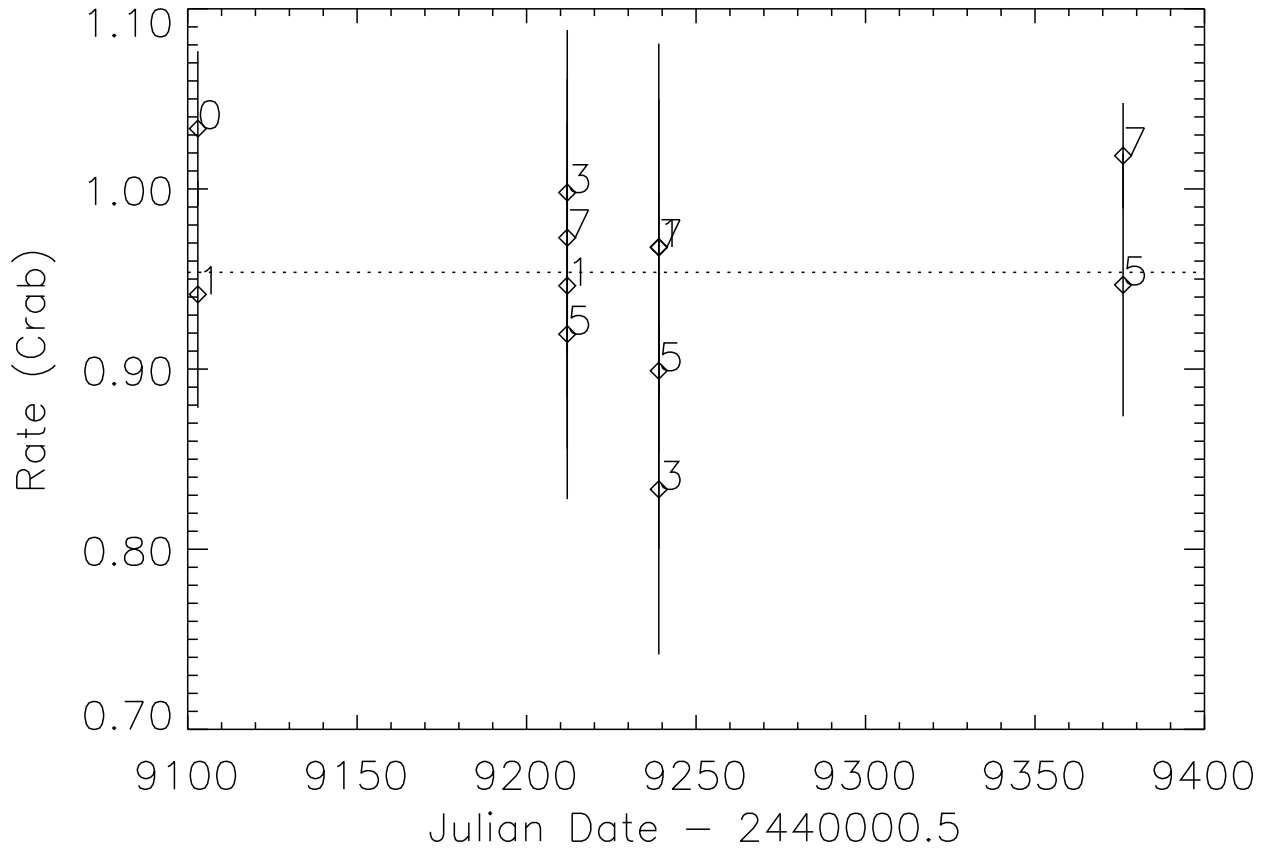


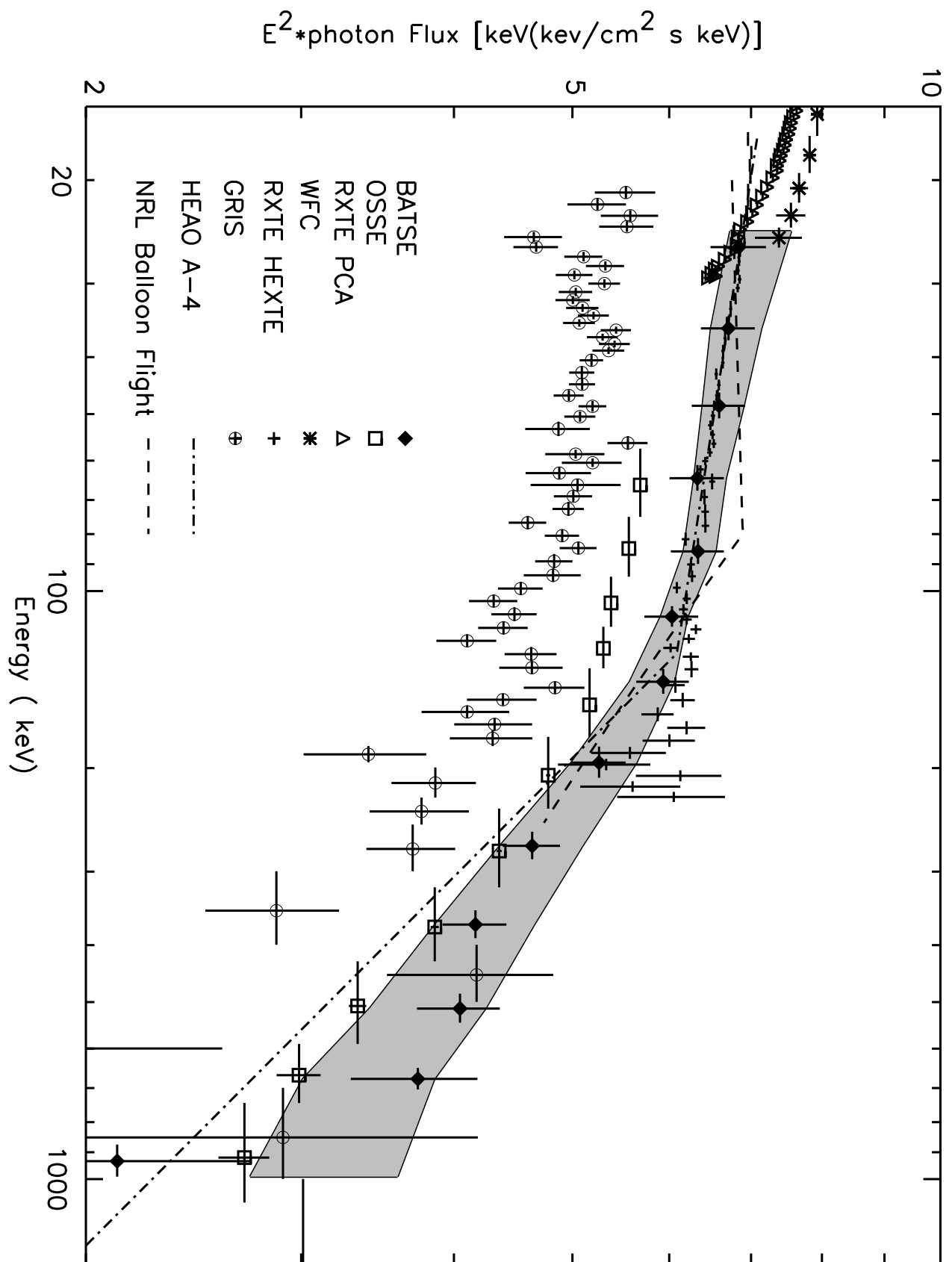


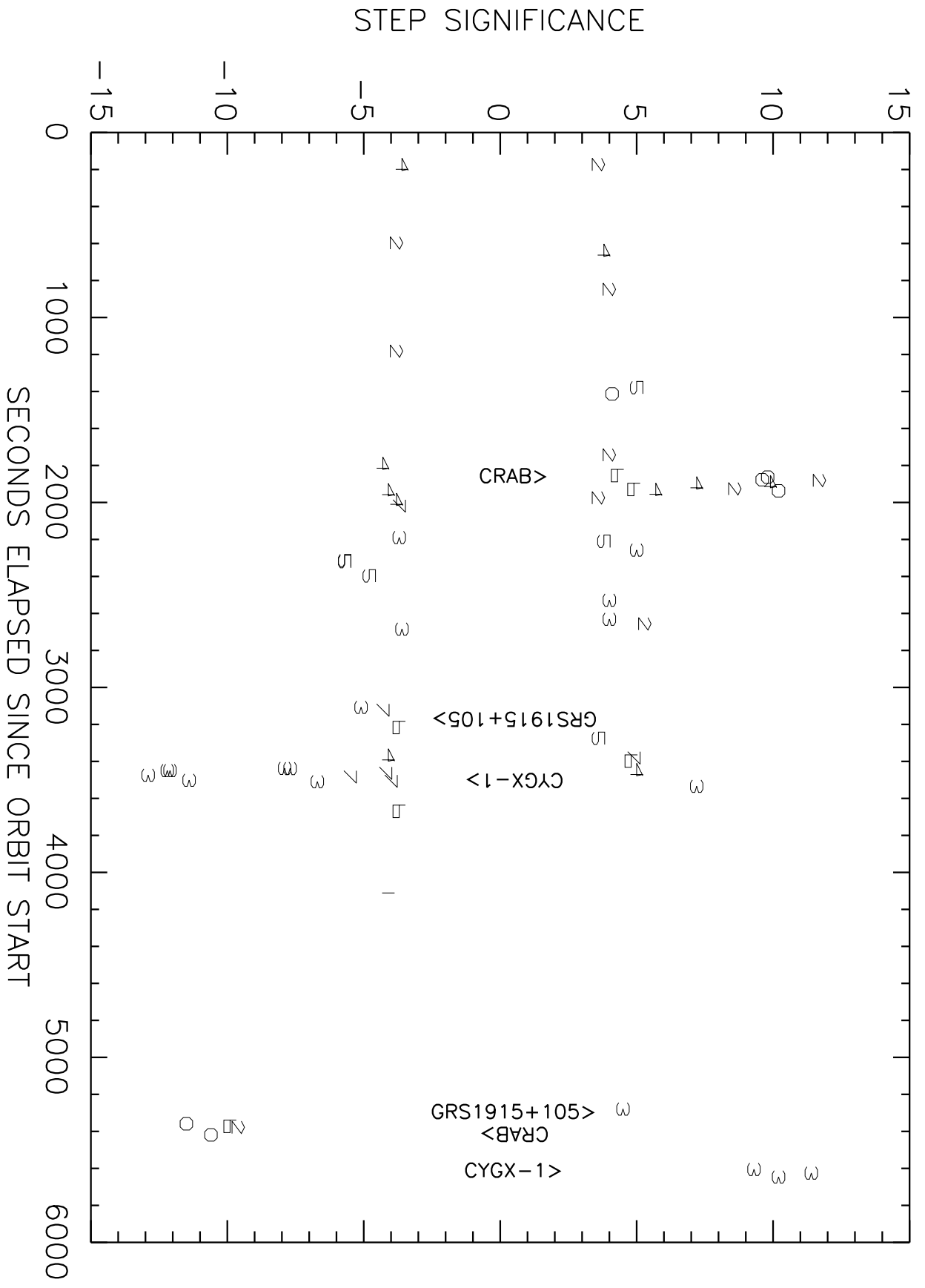


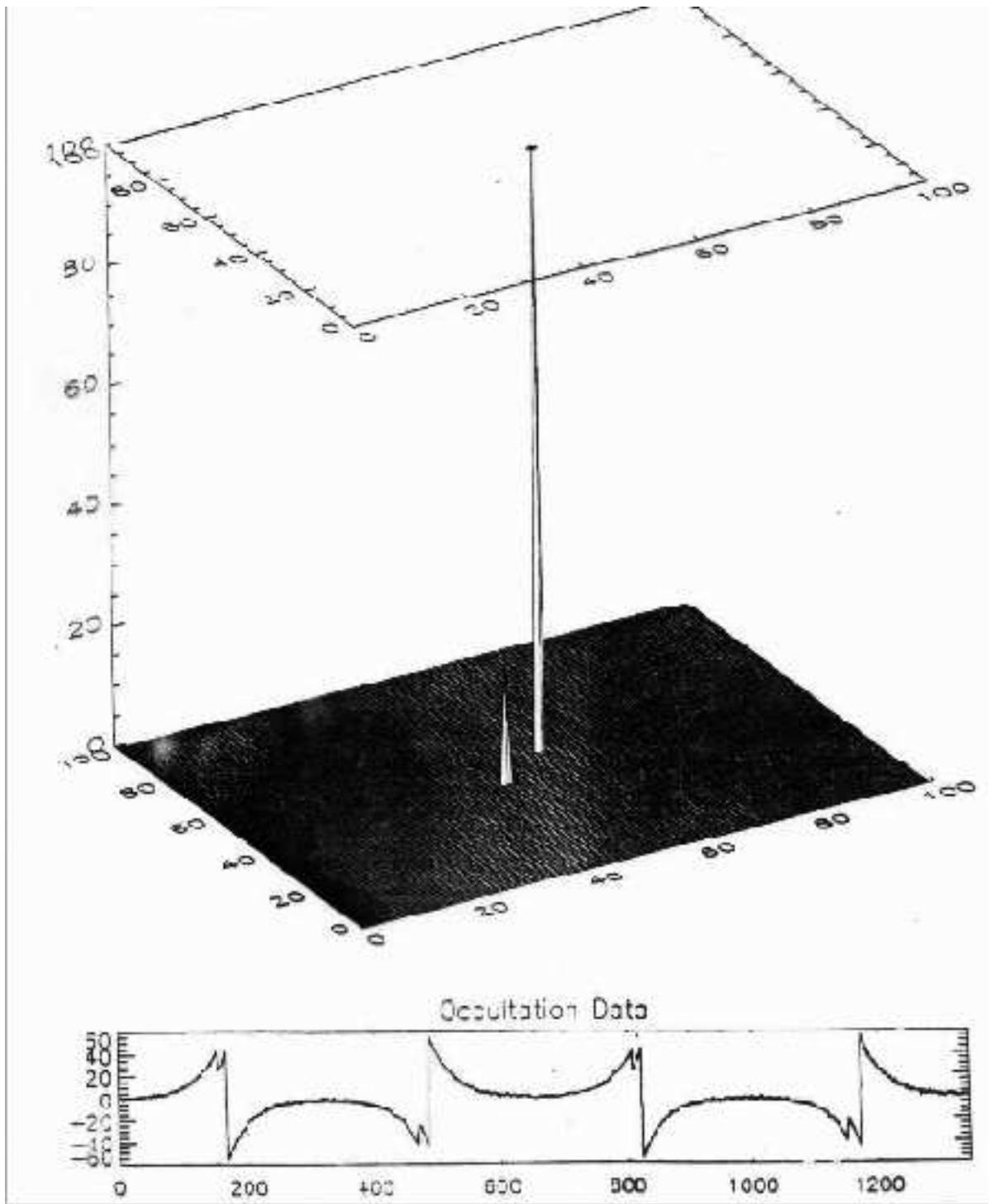




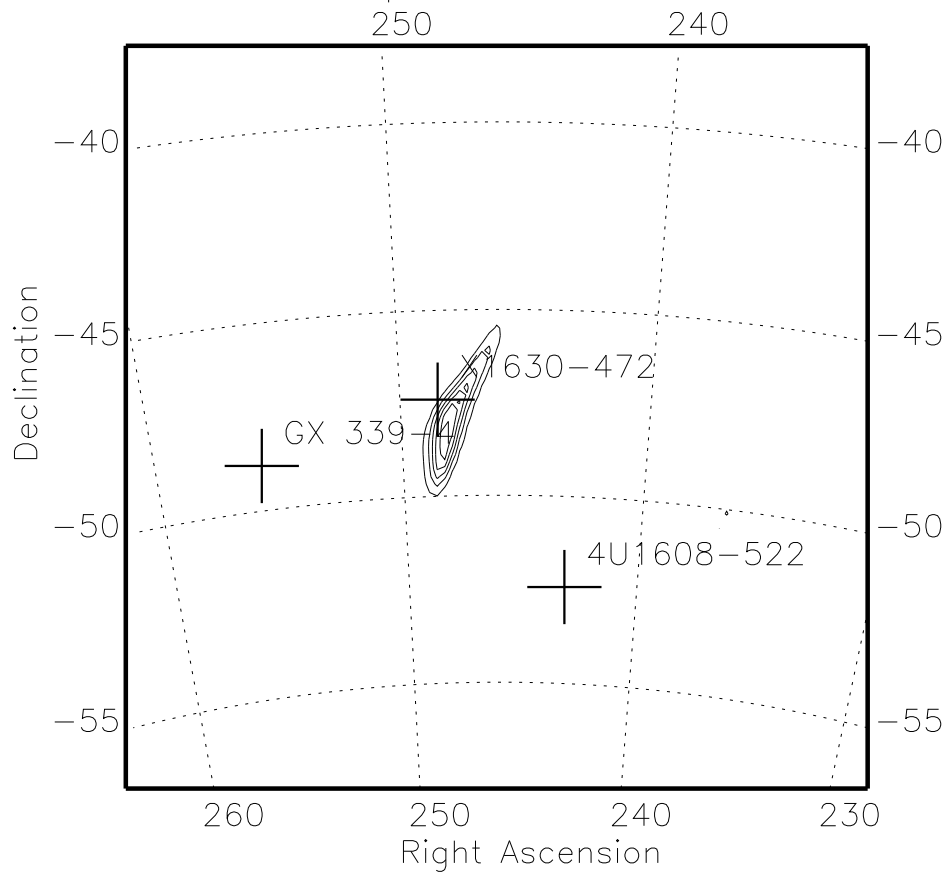




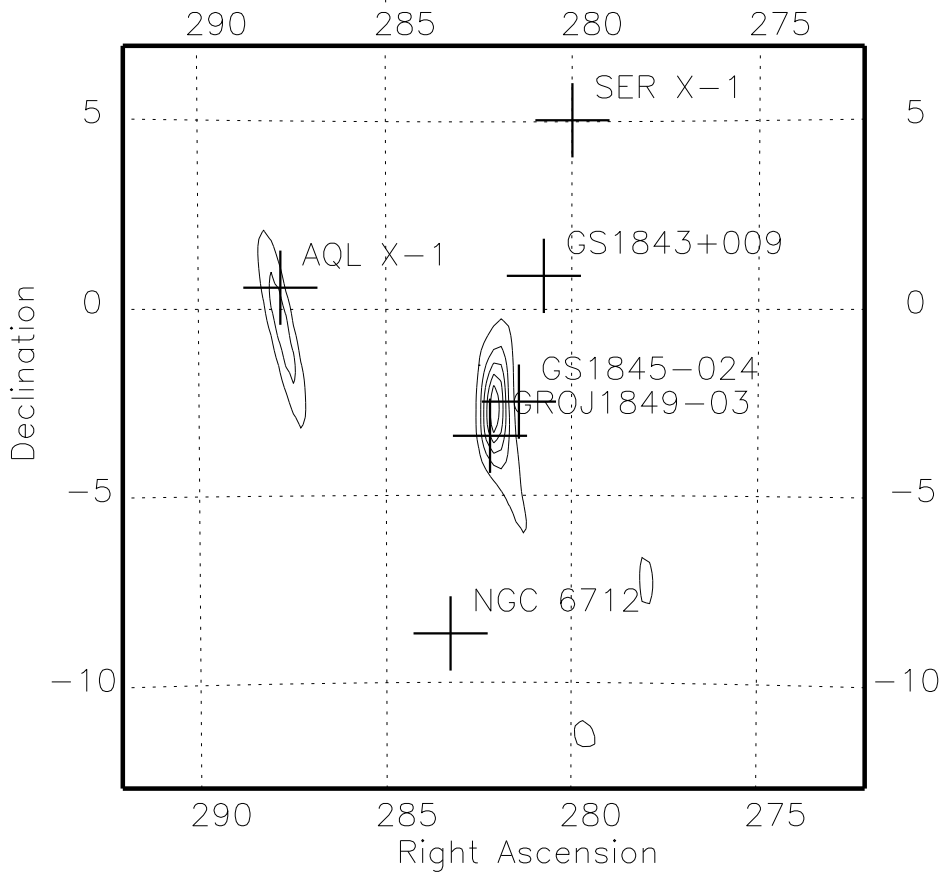




8389-8398 Map No. 1 Ch 1



8408-8417 Map No. 1 Ch 1

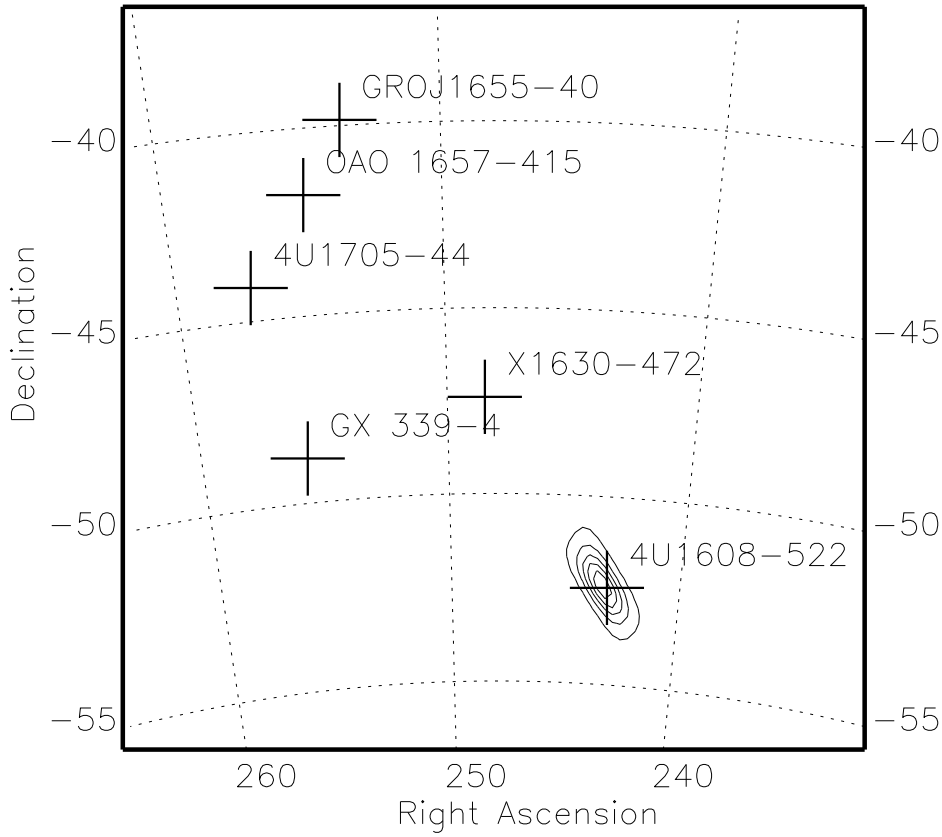


8580–8589 Map No. 8 Ch 1

260

250

240



8590–8599 Map No. 8 Ch 1

